TWO-PHASE 3D CFD MODELLING OF AN AIRLIFT PUMP

by

Geoffrey Gray

A Thesis
submitted to the Faculty of Graduate Studies of
the University of Manitoba
in partial fulfilment of the
requirements for the degree of

Master of Science
in
Mechanical Engineering

Winnipeg, Manitoba, Canada

Abstract

An airlift pump is a vertical tube that utilizes the buoyant effects of a gas to lift a liquid. Unlike a standard mechanical pump, the liquid flow rate through the airlift pump is not directly controlled; rather, it depends on the supplied gas flow rate, the tube length and diameter, and the relative height of the liquid supply free surface (submergence ratio). The present study uses the commercial CFD code ANSYS CFX to model the isothermal, 3-D, transient flow in an airlift pump using water and air.

The model applies pressure boundary conditions at both ends of the tube and specifies the mass flow rate of air through multiple openings in the side of the tube. The bottom of the tube is an inlet of water only and the outlet is a two-phase flow opening. A time-dependent, homogeneous, VOF two-phase RANS CFD modelling approach is used with the air treated as an ideal gas. Both the k-epsilon and SST turbulence models were each used in portions of this study.

This work found that a complete 3-D domain was necessary for consistent prediction of the airlift performance and physically realistic two-phase flow structures. Three airlift pump configurations (combinations from two tube lengths and submergence ratios) matching cases from experiments in the open literature were simulated. The CFD simulations predicted the overall trends in airlift performance. The agreement between the simulation and experimental results was better at low gas flow rates than at high gas flow rates. The two-phase flow structures of the simulations were studied using stochastic methods. Churn flow was the predominant flow regime observed in the simulation. Airlift pump instabilities characterized by low frequency large amplitude oscillations in the water flow were observed for one case of low gas flow rate. The more the liquid flow rate entering the airlift pump varied with time, the more the two-phase flow in the airlift pump deviated from conventional two-phase flow regime maps. The present study demonstrated that a 3-D CFD model is a valuable approach to the study of the two-phase flow in an airlift pump.

Acknowledgements

I would like to sincerely thank my advisors, Dr. Scott Ormiston and Dr. Hassan Soliman for their support and guidance throughout my masters program. Special thanks to the instructors of my graduate courses, Dr. Mark Tachie and Dr. Bing-Chen Wang; not only were your courses informative and enjoyable, they benefited my research work. I would like to thank the University of Manitoba and the Compute Canada support staff for quickly resolving technical problems, allowing me to complete my computing tasks.

The financial support of the Natural Sciences and Engineering Research Council of Canada (NSERC) and University of Manitoba Engineering Department is gratefully acknowledged.

Contents

List of Tables

List of Figures

Nomenclature

A	area, m^2
C_0	distribution parameter
d	diameter, m
E	airlift effectiveness
f	friction factor
g	gravity, $\mathrm{m\,s^{-2}}$
H_L	static lift, m
H_S	submerged depth, m
J	superficial velocity, $\mathrm{m\,s^{-1}}$
k	turbulent kinetic energy, $\mathrm{m^2\,s^{-2}}$
L	length, m
$\dot{m}$	mass flow rate, $\mathrm{kg\,h^{-1}}$
N	number of nodes
P	pressure, $\mathrm{N\,m^{-2}}$
$\tilde{P}$	modified pressure used in CFX, $\mathrm{N\,m^{-2}}$
$\dot{Q}$	volumetric flow rate, $\mathrm{m^3\,s^{-1}}$
$\boldsymbol{r}$	position vector, m
s	slip ratio
S_r	submergence ratio
t	time, s
$\boldsymbol{T}$	stress tensor
U	bulk velocity, $\mathrm{m\,s^{-1}}$
$\boldsymbol{U}$	velocity vector, $\mathrm{m\,s^{-1}}$
v_d	drift velocity, $\mathrm{m\,s^{-1}}$
X	Lockhart-Martinelli parameter

Greek Letters

α	void fraction
β	volume fraction
$\boldsymbol{\gamma}$	strain rate tensor, $\mathrm{m\,s^{-1}}$
σ	surface tension coefficient, $\mathrm{N\,m^{-1}}$
ε	turbulent dissipation rate, $\mathrm{m^2\,s^{-3}}$
μ	dynamic viscosity, $\mathrm{kg\,m^{-1}\,s^{-1}}$
η	airlift efficiency
ρ	density, $\mathrm{kg\,m^{-3}}$
τ_w	wall shear stress, $\mathrm{N\,m^{-2}}$
ϕ_ℓ^2	Lockhart-Martinelli two-phase multiplier
χ	quality
ω	turbulent frequency, $\mathrm{s^{-1}}$

Subscripts

atm	atmospheric
ent	entrance
G	gas phase
in	inlet boundary
inj	injection
L	liquid phase
out	outlet boundary
q	generalized q^{th} phase
ref	reference location or value
ris	riser
tot	total mixture

Superscripts

n	value at the current time step
rms	root mean square of a given time signal
T	transpose of vector
$'$	fluctuating component

Averaging

$\langle\phi\rangle_{\mathrm{p}}$	perimeter average
$\langle\phi\rangle_{\mathrm{A}}$	area average

$\langle \phi \rangle_V$	volume average
$\overline{\phi}$	time average
$\langle \overline{\phi} \rangle_\mathrm{p}$	time and perimeter average
$\langle \overline{\phi} \rangle_\mathrm{A}$	time and area average
$\langle \overline{\phi} \rangle_V$	time and volume average
$\overline{\widetilde{\phi}}$	moving mean smoothing
$\widehat{R}_\phi$	instantaneous value normalized by time average

Abbreviations

CSF	Continuum Surface Force
DNS	Direct Numerical Simulation
LES	Large-Eddy Simulation
PD	Probability Density
PDF	Probability Density Function
RANS	Reynolds-Averaged Navier-Stokes
SST	Shear Stress Transport
WMS	Wire Mesh Sensor
VOF	Volume Of Fluid

Chapter 1

Introduction

The airlift pump was first introduced by German engineer Carl Löscher in 1797 [1]. Since it's conception, airlift pumps have been used in a variety of applications and industries including but not limited to: petroleum and chemical processing, pumping of hazardous or corrosive liquids, deep sea mining, and artificial ocean upwelling. In recent years, airlift pumps have become popular in the growing aquaculture industry [2].

Some of the main advantages of airlift pumps over conventional mechanical pumps is the low maintenance, ease of installation, and reliability [1]. All the moving parts can be kept outside of the pumping environment. An additional benefit of the airlift pump for aquaculture applications is the enhanced mass transfer between phases, promoting the oxygenation of the water [3–5]. The primary shortcomings of the airlift pump are the low pumping head, and difficulty in precisely controlling the discharge rate.

The airlift pump must be distinguished from the airlift loop reactor. As the name suggests, the goal of the airlift pump is to transport a working fluid. Whereas the airlift loop reactor circulates the fluid within a contained vessel, no net transport occurs.

1.1 Problem Background

1.1.1 Airlift Pump

The airlift pump is a multiphase flow device that utilizes the buoyancy effects of gas to lift liquid (two-phase) or liquid-solid mixtures (three-phase). For the sake of brevity the following discussion is in reference to two-phase airlift pumps, although the same general principles also apply to an airlift pump operating in three-phase flow [6, 7].

Airlift Pump Geometry

The airlift pump consists of four main components:

1. A source of liquid to be pumped.
2. A **suction pipe** where the liquid enters.
3. An air injection apparatus where compressed gas enters.
4. A **riser pipe** (sometimes referred to as an eduction pipe) where the two-phase mixture flows upward and is discharged at the outlet.

Typically, circular pipes (of diameter D) are used for the riser and suction pipes but rectangular channels and tapered pipes have also been used. Airlift pump construction varies depending on how the source of liquid is supplied. Figure 1.1(a) shows a common airlift configuration in practical applications, referred to in the present work as **immersed-riser**. The riser is immersed in the body of liquid it is pumping. In most situations, the basin is very large such that the free surface of the liquid supply remains constant as the airlift pump operates. The **U-tube** configuration in Figure 1.1(b) is more often used in experimental setups. Liquid is continuously added to the supply tank by a secondary system to maintain the level of the free surface.

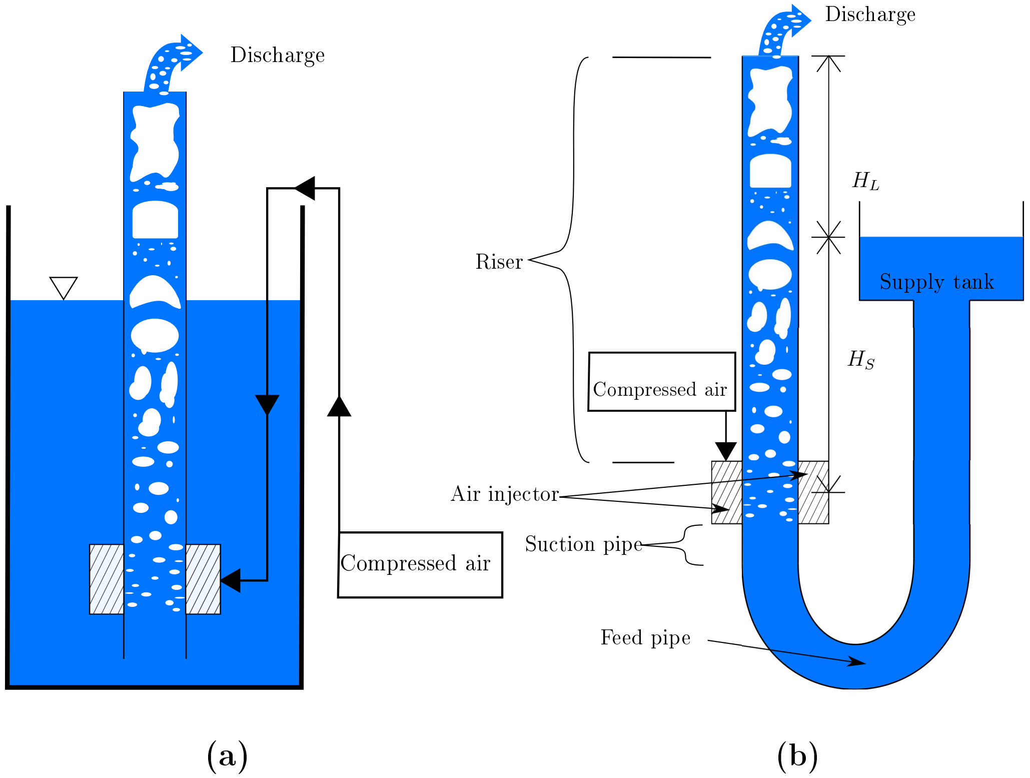

Figure 1.1: Schematic of airlift pump setups: (a) immersed-riser type, (b) U-tube type.

The **submergence ratio** (S_r) is an important parameter for understanding the performance of an airlift pump. It represents how far submerged the riser pipe is relative to its length. In experimental apparatus constructed in the U-tube style, the supply tank is moved up or down to adjust the submergence ratio.

$$S_r = \frac{H_S}{H_S + H_L} = \frac{H_S}{L} \tag{1.1}$$

where H_S is the submerged depth, H_L is the static lift, and L is the length of the airlift riser. In addition to the submergence ratio, the length and diameter of the riser, and the air injector also effect the performance of an airlift pump. The effect of each parameter is discussed in greater detail in Section 2.1.

Regardless of the airlift pump configuration, a variety of different devices have been used to introduce the gas into the liquid. The effects of the air injection devices are discussed in further detail in Section 2.1. Presently, they will be classified into five categories:

Airjacket (AJ) A larger pipe (jacket) is placed around the riser pipe. A large number of small holes made in the interior pipe. The gas is supplied to the jacket through one or several large holes, from there it distributes amongst the many small ones entering the riser in the radial direction.

Nozzle (N) A footpiece with one or several holes is positioned inside the riser pipe. The gas is injected axially in a more concentrated region.

Dual (D) The gas is injected both radially similar to an airjacket, and axially around the perimeter of the inner pipe wall. Typically the footpiece is located concentrically within the entrance pipe.

Swirl (S) The gas is injected tangentially from the wall of the pipe at some upward angle with respect to the axial direction. A moderate number of the swirl injection ports are located around the circumference.

T-junction (T) The gas enters radially from the horizontal branch of a T-junction pipe fitting. The liquid enters through the bottom branch, and the two-phase mixture exits the top branch.

Airlift Pump Physics

A unique characteristic of the airlift pump is that the liquid flow rate is not directly specified; instead, it is a function of the gas flow rate. Once the gas is introduced, a two-phase flow develops and travels up the riser. Because the density of the mixture is lighter than the single phase liquid, a favorable pressure gradient exist to draw in more liquid through the suction pipe. The liquid flow rate is an implicit result of the two-phase flow phenomena occurring in the riser pipe.

Because of the unsteady and chaotic nature of two-phase flow, the local instantaneous flow rate of liquid will not be constant. When the liquid flow rate is averaged over a sufficiently long period of time, the average liquid flow rate in and out of the airlift pump converge to a constant value. This average liquid flow rate is referred to henceforth as the **liquid discharge rate**. The instantaneous flow rate of liquid entering the airlift pump (drawn in through the suction pipe) and exiting the riser pipe are referred to as **suction flow rate** and **eduction flow rate**, respectively. The liquid discharge rate is calculated over a period of pseudo-steady operation. During pseudo-steady operation, the fluctuations in liquid flow rate are solely due to the two-phase flow and any transient or startup effects would have dampened out. The suction flow rate will be nearly constant with respect to time. The eduction rate will always vary with time due to the intermittent nature of the two-phase flow. Transient or startup effects can occur when the gas flow rate is changed. When the transient effects do not dampen out over time the airlift pump is said to be unstable. Airlift pump instabilities are discussed further in Section 2.1.4.

The liquid discharge rate is the key quantity of interest when considering the performance of an airlift. The relationship between gas flow rate and liquid discharge rate is commonly presented with a **performance curve**, as seen in Figure 1.2. The operation of the airlift pump can be described by three regions. There is a minimum gas flow rate required to initiate liquid discharge (region I). The size of region I is exaggerated in Figure 1.2 for clarity. Once the minimum gas flow rate threshold is surpassed, there is a period where the water flow rate increases rapidly with increased gas flow rate, as seen in region II. In region III, the water flow rate begins to plateau and remains constant or decreases slightly with increased gas flow rate. The behaviour of the airlift performance curve is attributed to a change in the two-phase flow regime, as discussed further in Section 2.1.

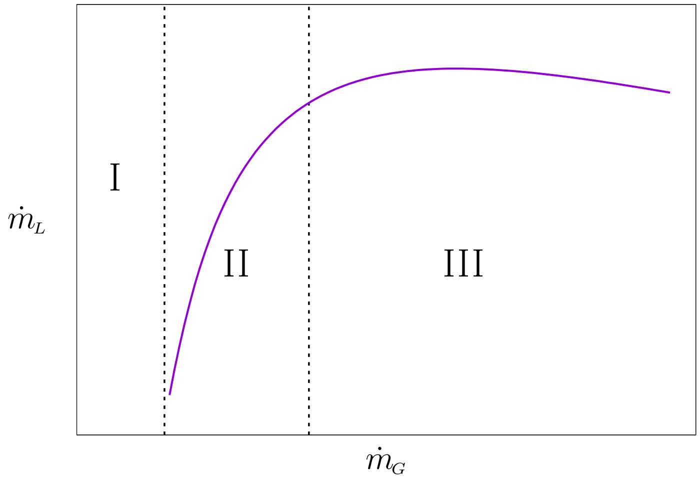

Figure 1.2: Sketch of a typical performance curve of an airlift pump.

The liquid discharge rate is not the only quantity for evaluating an airlift pump, the pumping effectiveness and efficiency are also used. **Pumping effectiveness** is defined as the ratio of liquid flow rate to gas flow rate:

$$E = \frac{\dot{m}_L}{\dot{m}_G} \tag{1.2}$$

Considering the generic performance curve seen in Figure 1.2, the effectiveness increases at first in region II until it reaches a maximum then decreases through region III.

The **airlift pump efficiency** defined by Nicklin [8] represent the ratio of the work needed to lift the liquid above the free surface to the work done by the isothermal expansion of gas:

$$\eta = \frac{\rho_L g \dot{Q}_L H_L}{P_{\text{atm}} \dot{Q}_G \ln({}^{P_{\text{inj}}}/_{P_{\text{atm}}})} \tag{1.3}$$

Because the air injection pressure appears in Eq. (1.3), the air injector design can affect efficiency. The curve of airlift pump efficiency versus gas flow rate typically has a steep left skewed bell-shaped profile. The maximum efficiency point does not necessarily correspond to the maximum effectiveness, as discussed further in Section 2.1.6

1.1.2 General Two-Phase Flow Theory

In order to study the airlift pump, understanding of the fundamental concepts of multiphase flow is required. It is not the intention of this work to provide a comprehensive review of the literature on two-phase flow. Rather, topics most relevant to the airlift pump are highlighted.

Traditionally, two-phase flow in vertical pipes has been studied by controlling the flow rate of each phase entering the pipe independently. This approach is different from the airlift pump where the pressure at the entrance of the pipe, not the liquid flow rate, is constrained. Despite this difference of inlet boundary condition, the vast majority of standard two-phase flow theory is applicable to the airlift pump. The buoyancy driven two-phase flow of the airlift pump can be considered a special case of standard gas-liquid flows.

Terminology

Slip is the ratio of gas velocity to liquid velocity. It is typically greater than 1 due to buoyancy.

$$s = \frac{U_G}{U_L} \tag{1.4}$$

Volume fraction is the fraction of a volume occupied by a particular phase. The volume fraction of all phases must sum to unity.

$$\beta = \frac{\dot{Q}_G}{\dot{Q}_G + \dot{Q}_L} \tag{1.5}$$

Quality Is the mass fraction of the gas phase.

$$\chi = \frac{\dot{m}_G}{\dot{m}_G + \dot{m}_L} \tag{1.6}$$

Void fraction represents the ratio of the area occupied by a given phase to the total area. The void fraction does not equal the volume fraction unless slip ratio $s = 1$. In the homogeneous numerical model the local volume fraction within a control volume is equal to the local void fraction. For either phase $q = G, L$

$$\alpha_q = \frac{A_q}{A} \tag{1.7}$$

Superficial velocity is the volumetric flow rate flux. It can be interpreted as the bulk velocity if the given phase was flowing alone. The superficial velocity is related to the true velocity. For either phase $q = G, L$

$$J_q = \frac{\dot{Q}_q}{A} = U_q \alpha_q \tag{1.8}$$

Disperse phase Phase distribution characterized by small interfacial length scales such as small bubble, droplet, or solid particle. A dispersed phase is distributed within a continuous phase, typically with a small volume fraction.

Continuous phase Phase distribution characterized by largely uninterrupted regions over large length scales. As previously stated, a continuous phase can act as a carrier phase for dispersed phase. Alternatively, several continuous phases can be present in separated or stratified flows.

Discrete phase Phase distribution characterized by large interfacial length scales. The regions of each phase are distinct, separate, and well defined. Both phases can be said to be continuous. Free surface, stratified, and slug flows are cases when discrete phases are present.

Homogeneous model All phases are assumed to be traveling at the same local velocity. Further discussion of the homogeneous approach as it pertains to the CFD modeling of gas-liquid flows is provided in Appendix A.2.1.

Multi-fluid model A more general case of the two-fluid model. A set of conservation equations is solved for each phase. The interfacial momentum transfer is required for closure of the momentum equation. Further information can be found in Appendix A.2.2

1-D drift flux model is a popular model for gas-liquid flows in pipes. The flow is modeled using area-averaged properties and the total superficial velocity, ($J_{\text{tot}} = J_G + J_L$). The drift flux model provides a means of predicting the average void fraction.

$$\frac{J_G}{\langle \alpha_G \rangle_{\text{A}}} = C_0 J_{\text{tot}} + v_d \tag{1.9}$$

where C_0 is the **distribution coefficient**, and v_d is the **drift velocity**. Physically, the distribution coefficient accounts for the effect of the velocity gradient in the primary phase. It depends on geometry, fluid properties and flow rate. The drift velocity represents the relative velocity of the gas phase with respect to the coordinate frame of the total velocity. A number of empirical expressions are available for determining C_0 and v_d depending on the flow regime.

Upward Vertical Flow Regimes

Flow patterns or regimes categorize multiphase flows based on recurring interfacial structures [9]. Consensus has been reached on four main flow patterns for vertical pipe flow, although terminology still varies. Figure 1.3 depicts the morphology of the vertical upward pipe flow patterns, namely: bubbly, slug, churn, and annular. The present discussion is limited to slug and churn flow because they are the most commonly encountered flow regimes in the airlift pump. A more thorough description of all the flow regimes is provided in Appendix A.1

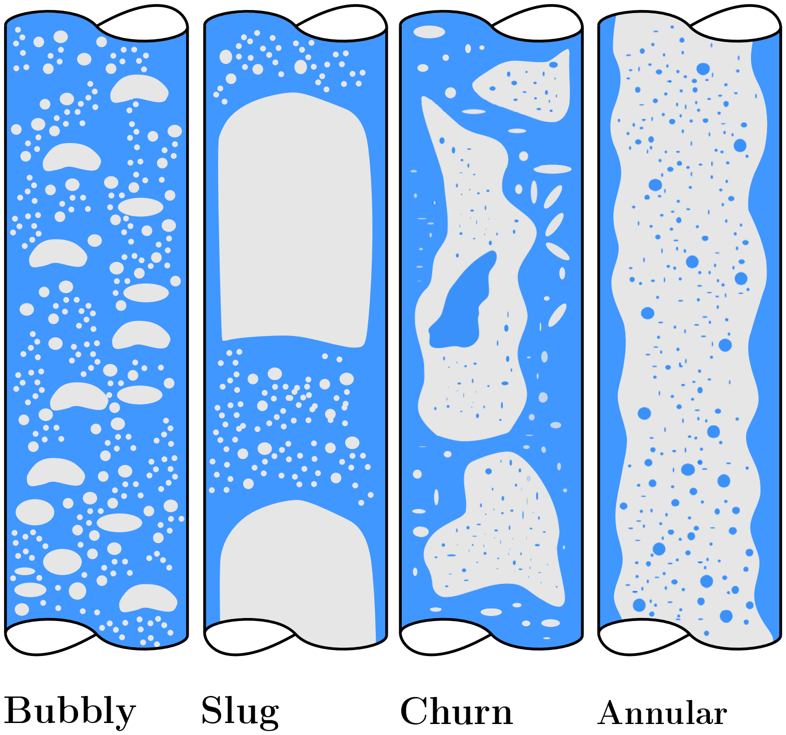

Figure 1.3: Sketch of upward vertical gas-liquid flow regimes.

The slug flow regime is categorized by the formation of large bullet-shaped bubbles know as slugs, or Taylor bubbles. Alternating gas slugs and liquid slugs travel up the pipe in a regular manner. In churn flow, the gas forms large irregular structures that may contain smaller pockets of liquid within them. Churn flow is highly turbulent and chaotic in appearance compared to slug flow.

The flow regimes represent well-developed two-phase flow where average quantities do not change with respect to length. Local two-phase flow structures near changes in geometry, entrance regions, or other obstruction do not necessarily abide by the established flow patterns shown in Figure 1.3. The development length for multiphase flow patterns depends on the flow pattern and how the phases are introduced. The well-developed flow pattern, however, is independent of the injection method. The physical mechanisms of each of the four vertical upward flow patterns are briefly discussed in the following sections.

Identification of Flow Regimes

In practice, it is not as easy to distinguish between flow regimes as the sketches in Figure 1.3 suggest. The structures do not make discontinuous jumps between regimes, rather there is a gradual transition from one regime to the next. Visual identification is the most commonly used technique for identifying flow regimes but it has disadvantages (for more information, see Appendix A.1.1) due to its subjective nature. The statistical analysis of local flow fluctuations provides objective methods for determining flow regimes and characterizing the two-phase flow [10]. Stochastic methods allow for the quantification of flow behaviour during regime transition.

Statistical Signatures of Two-phase Flow

The flow regime can be indirectly determined by studying the fluctuations of various measured quantities, such as the time signal of cross-sectional-averaged void fraction. The probability density (PD) is calculated from the time signal categorizing the fluctuations over time. The different flow regimes have distinctly different signatures to their probability density function (PDF), as shown in Figure 1.4. For faithful prediction of the flow pattern, the time series of average void fraction must be measured in the well-developed region of the flow.

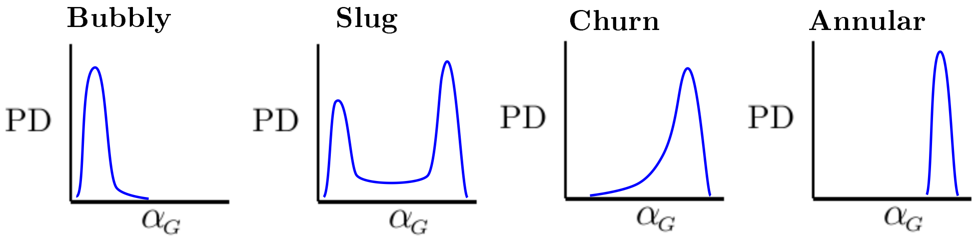

Figure 1.4: Sketch of void fraction PDF signatures for vertical upward two-phase flow regimes.

The differences in probability density distribution are related to the physical nature of each flow regime. The relatively small bubbles compared to tube diameter and dispersed nature of bubbly flow means the void fraction averaged over a pipe cross-section is essentially steady with time. This corresponds to a PDF signature of a concentrated spike at a low void fraction.

In slug flow, the time series of void fraction and the corresponding PDF reflect the regular passing of discrete pockets of each phase. The void fraction alternates between high and low values in a step function type profile. The void fraction PDF has a bimodal distribution (U-shaped profile) with high occurrence of low and high void fraction, and low occurrence of intermediate void fraction.

In churn flow, the amplitude, and frequency of oscillations in the void fraction time series is the greatest of all flow regimes. There is no consistent or repeatable pattern to the oscillations in the signal, unlike slug flow. Despite the seemingly random nature of the instantaneous values, the PDF of the void fraction has a recognizable signature of a left skewed distribution. Statistical methods are especially valuable for studying churn flow because the fluctuations are chaotic and the interfacial structures are irregular.

The interfacial structures of annular flow are far more stable than churn flow, resulting in a much steadier instantaneous value of average void fraction. The average void fraction time series and PDF of annular flow is similar to that of bubbly flow, except at a high value of void fraction, in contrast to a low value for bubbly flow.

Flow Regime Map

Flow regime maps are a useful tool when dealing with multiphase flow. They predict which flow regime is likely to occur based on integral scale flow parameters, typically involving superficial velocities. The prediction of flow regime transition for improved flow map accuracy is still an ongoing endeavor [11]. Numerous authors have proposed different transition lines based on theoretical or empirical analysis. The upward vertical flow maps by Taitel *et al.* [12], Mishima and Ishii [13], and Hewitt and Roberts [14] are commonly used in the literature, although there are many others.

The transition lines of the Taitel *et al.* [12] flow map (shown in Figure 1.5) depend on pipe diameter, and in the case of slug-to-churn transition also on the ratio of length to diameter. Although the transition lines are drawn through discrete points, regime transition occurs over a zone of finite width. It should be emphasized that flow maps have been derived from data collected from well-developed two-phase flow where the inlet flow rate of both phases is regulated and constant with respect to time.

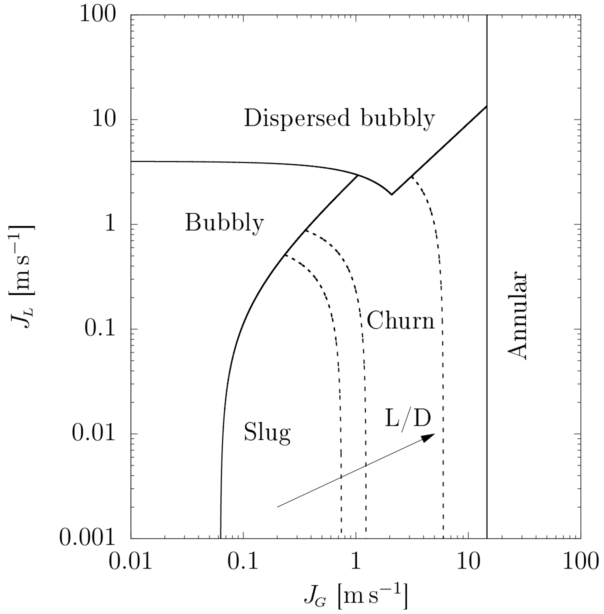

Figure 1.5: Vertical gas-liquid flow map by Taitel *et al.* [12] for air-water system, $D = 25$ mm.

1.2 Thesis Objectives

The purpose of this thesis is to study the hydrodynamics and two-phase flow characteristics of the airlift pump using a detailed 3-D CFD model. It will be demonstrated in Section 2.2 that the details of the flow in an airlift pump riser have not received considerable attention in the literature. Improved understanding of the two-phase flow in the airlift pump is required to advance the simplified modeling tools used in airlift pump design, and ultimately improve airlift pump performance. This work will address these shortcomings by accomplishing the following objectives:

1. To develop an appropriate detailed numerical model of an airlift pump system.
2. To assess the accuracy of the liquid discharge rate predicted by the numerical model and the validity of the observed two-phase flow physics.
3. To explore relevant trends and physics of the airlift pump. In particular, the affects of gas flow rate, submergence ratio, and riser length on the transient behaviour of the liquid suction rate, two-phase flow regime and time-averaged quantities.

Chapter 2

Literature Review

This chapter first focuses on the literature directly related to the airlift pump. Secondly, supporting literature related to the numerical modeling techniques to be used later in this work are covered. Lastly, the rationale for this work is presented and it is discussed how this work fits within the current state of the art in the open literature.

2.1 Airlift

The majority of research on airlift pumps has been conducted experimentally. The subsequent review is limited to airlift operating in two-phase flow. Air and water are typically used as the working fluids, however the trends are the same regardless of the specific gas and liquid used. For practical reasons, the U-tube style of airlift (Figure 1.1(b)) is most commonly used in experimental apparatus. The riser pipe is more accessible for installation of measuring instruments and the view of the flow is not obstructed by the supply liquid.

2.1.1 Experimental Studies

The geometric parameters of each of the subsequent studies are summarized at the end of this section, in Table 2.1. The U-tube style was used in all of the studies discussed below unless otherwise stated.

Stenning and Martin [15] measured airlift pump performance for a range of submergence ratios. The airlift was constructed using the immersed riser style. Values for slip ratio and effective friction factor were extracted from the measured flow rates for calibration of their proposed model. The experimentally determined slip ratio had good agreement with the empirical predictions for fully-developed flow, whereas the friction factor measured in the airlift pump was approximately two times greater than the theory.

Todoroki *et al.* [16], and Clark and Dabolt [17] performed limited experiments in order to validate their theoretical models. The liquid discharge rate was recorded for several airlift pump configurations but no new performance behaviour or trends were reported.

Parker [18] studied the effect of air injector design with airjacket and nozzle footpieces. The airlift was constructed using the immersed riser style, the nozzle was positioned some distance below the bell mouth opening to the riser pipe. For both injector types, the total area and hole distribution were varied. Trials were performed for several submergence ratios, with one riser length and diameter. The airlift performance was practically independent of injector design when the airjacket style was used. A nozzle injector with small area was found to increase water discharge rate at high gas flow rates (region III of Figure 1.2); however, this came at the expense of decreased effectiveness and efficiency. For both airjacket and nozzle injectors, peak efficiency occurred with the largest hole size. This was attributed to a smaller pressure drop across the air injection orifice. Overall, the efficiency curves of the airjacket and nozzle injectors were comparable, although the nozzle had a slightly higher maximum efficiency.

Kouremenos and Staïcos [19] devised an air injection apparatus that maintained ‘perfect’ slug flow. A nozzle-style orifice was supplied with a pulsating air supply. This configuration was reported to produce perfect and constant slug flow for all experiments. The experiments considered several riser diameters and submergence ratios but the range of gas flow rates was limited compared to most airlift pump studies.

Reinemann *et al.* [20] focused their study on airlift pumps with small riser tube diameters (3 to 19 mm). Measurements of liquid flow rate were recorded for a range of submergence ratios and a fixed length. The bubble rise velocity was determined by timing the Taylor bubble traveling over a known distance marked on the riser pipe. The two-phase flow behaviour in small diameter pipes differs from large diameters pipes because capillary effects (see Appendix A.1)become significant. For diameters less than 20 mm, the maximum efficiency and the optimum submergence ratio increased with a decrease in diameter. In addition to the performance trends, a more rigorous analysis of the slug flow occurring in the riser was presented. The distribution coefficient in a small diameter airlift operating at low Reynolds number (Re) was found to differ from the value obtained from a single gas slugs rising in a continuous and regulated liquid stream of equivalently small Re. The authors theorized that the buoyancy-driven liquid flow in the airlift resulted in a turbulent velocity profile in the liquid at Re as small as 500. This was supported by the observation of erratic motion of small gas bubbles trapped in the liquid slugs.

de Cachard and Delhaye [21] designed an experimental apparatus that could function as an airlift pump (where the liquid flow rate is not specified) or a standard two-phase flow test section (where both gas and liquid flow rates are controlled). In the controlled flow cases, the instantaneous void fraction and pressure drop were recorded at a series of axial locations. The gas and liquid flow rates were specified to values similar to the average flow rates encountered in airlift pump operation. The flow measurements of the controlled flow experiments were used to support the theoretical modeling and discussion of the airlift pump behaviour. The frictional pressure drop was higher at the location nearest to the air injector where the flow regime was developing, and lower at the top of the riser where the flow regime was well-developed. The airlift pump cases were performed for two submergence ratios and only the water flow rate was measured. Churn flow was observed in the entrance region, even when the developed flow pattern was slug flow. They concluded that neglecting the entrance effects in shorter risers ($^{L}/_{D} < 250$) would lead to errors in modeling and performance prediction.

Khalil *et al.* [22] performed an experimental study of airlift pumps with different nozzle geometries. The airlift pump was constructed using the immersed riser style, and the nozzle was positioned within the riser pipe. The airlift pump performance and efficiency were recorded for nine different nozzles and a range of submergence ratios. The nozzles had similar total injection area but varied in the number and size of holes. The nozzle design was found to affect both the performance and efficiency. The nozzle geometry with the highest effectiveness for a given air flow rate did not have the highest efficiency. Efficiency favored a nozzle with fewer holes and a larger hole diameter. This trend is consistent with the work of Parker [18].

Lawniczak *et al.* [23] conducted an experimental study of short airlift pumps operating at low submergence ratios. A nozzle-style air injector was used where a nozzle was positioned in a tapered (bell-mouth) entrance pipe. The effect of the vertical position of the nozzle within the bell-mouth was also studied. It was found that all efficiency curves had a well defined maximum, which increased in magnitude and shifted towards lower gas flow rates as the submergence ratio increased. The efficiency curves had a steeper peak for the smaller diameter riser. The influence of nozzle position depended on the riser diameter and submergence ratio. When the nozzle was too close to the riser pipe it obstructed the flow lowering maximum efficiency, once the nozzle was sufficiently far away further displacement had a negligible effect on the efficiency. A universal optimum nozzle position was not found. A dimensionless empirical relationship was correlated to prediction the maximum efficiency. The correlation was developed using only the authors own data.

Castro *et al.* [24] recognized a lack of experimental data in the literature for short (small L/D) airlift pumps. Their descriptions of the experimental apparatus and air injection method are incomplete. Water discharge rate was recorded for a short airlift pump over a comprehensive range of diameters, lengths, and submergence ratios. Several new arrangements were used for plotting the experimental data to highlight the effect of the independent parameters. The length had a substantial effect on the performance of the short airlift pump, and was amplified with increased submergence ratio.

Kassab *et al.* [25, 26] examined the effect of tube length and submergence ratio on airlift performance and efficiency. The two-phase flow patterns in the riser were studied visually, and their effect on airlift behaviour was considered. Slug flow was always present when the optimum efficiency occurred. Slug flow was always present when the maximum liquid discharge was achieved; however, this point did not correspond to the maximum efficiency. As submergence ratio increased, both performance and efficiency increased. For an equivalent submergence ratio, increasing riser length increased both performance and efficiency.

Moisidis and Kastrinakis [27] studied the flow structure in an airlift riser over a range of submergence ratios. Two-point conductivity probes were used to measure the instantaneous void fraction at several locations along the length of the riser. The time signals of void fraction, along with visual observation were used to analyze the flow regime. Consistent with other works, bubbly flow was not observed in practical operating conditions. When slug flow occurred, the liquid slugs were highly contaminated with dispersed gas bubbles, resulting in high frequency chaotic fluctuations in the otherwise periodic conductivity signal. Because of the relationship between submergence ratio, fluctuations in the liquid flow, and instabilities in the phasic interface, the submergence ratio affects the two-phase flow pattern. A flow regime map unique to airlift pumps was proposed with superficial gas velocity and submergence ratio as the coordinate axes. The proposed regime transitions were expected to shift to higher superficial velocities for a longer airlift riser, but additional experiments were not performed to confirm this.

Using the same experimental setup from their previous work, Moisidis and Kastrinakis [28] studied the pressure distribution in the airlift riser. Pressure transducers were used to record the differential pressure at numerous axial locations. The experimental findings were consistent with the assumptions of Stenning and Martin [15]; specifically, that the hydrostatic pressure gradient is much larger than the frictional pressure drop. Using the airlift model equation by Stenning and Martin [15], Moisidis and Kastrinakis [28] found higher values of the slip ratio better fit their data at lower submergence ratios, conversely lower values of slip fit higher submergence ratios.

Tighzert *et al.* [29] studied the effects of submergence ratio on performance, efficiency, and void fraction. Quick closing valves were used to measure the volume fraction in the riser. The optimum efficiency point for a given submergence ratio was found to occur when the slip ratio was at a minimum, just before the flow regime transitions from slug to churn. The maximum efficiency increased with submergence ratio up to 0.75, then decreased with further increase in submergence ratio. The void fraction in the riser decreased with an increase in submergence ratio for a given air flow rate. At low gas flow rates the void fraction in the riser fluctuated more chaotically than at higher gas flow rates. The agreement between the existing drift flux models and the measured void fraction improved with an increase in submergence ratio.

Hanafizadeh *et al.* [30, 31] proposed several airlift pump design equations based on their experimental results for a large diameter airlift pump. The water flow rate was recorded for multiple submergence ratios. Hanafizadeh *et al.* [30] defined an the airlift efficiency based on an exergy analysis.

$$\eta = \frac{\dot{m}_L \Delta\Psi_L}{\dot{m}_G \Delta\Psi_G} \tag{2.1}$$

where $\Delta\Psi$ is the change in exergy of the phase. The efficiency decreased with increasing superficial slip ratio. Hanafizadeh *et al.* [31] defined a pumping head unique to the airlift pump as

$$H^* = \frac{H_L}{\frac{P_{\text{air}}}{\rho_{mix} g}} \tag{2.2}$$

where P_{air} is the absolute pressure at the air injector and ρ_{mix} is the mixture density determined from the volume fraction. When the airlift pump head was plotted as a function of effectiveness, the data grouped in lines of constant air flow rate and were independent of the value of the submergence ratio.

Kim *et al.* [32] performed an experimental study of small diameter airlifts ranging from 8 mm to 24 mm. The authors' goal was to extend the application of airlift pumps to transporting molten fuel in direct carbon fuel cells. As a preliminary investigation, however water and air were used as the working fluids. The airlift was constructed using the immersed riser style. The airlift performance was presented in terms of dimensionless volume flow rates to facilitate comparison between different riser diameters. It was found that the smaller the riser diameter, the greater the peak effectiveness, and the lower the minimum dimensionless gas flow rate at which liquid discharge was initialed.

Ahmed *et al.* [33] conducted experiments to improve the design of the air injection system for airlift pumps. A number of different injection orientations and patterns were tested namely: radial, axial, dual, and swirl, with a steady or a pulsating air supply. A single riser geometry and submergence ratio was used to test the air injectors. The liquid discharge rate was measured and a high speed camera was used to visualize the flow. Improvements to the air injector had a minor effect on airlift effectiveness and a more substantial effect on efficiency. When a steady air supply was used, the dual air injector was found to be the most efficient. Pulsating the air supply at 1 Hz increased the efficiency of all air injectors. The potential of offsetting the pulsating air supply to the radial and axial portions of the dual injector was explored. The pulsating dual air injector performed best when the radial and axial injections were synchronized. The dual injector developed in this work was patented by Badr and Ahmed [34].

Abou Taleb and Al-Jarrah [35] experimentally studied the effect of airjacket hole size on airlift performance and efficiency. The airlift was constructed using the immersed riser style. Three airjackets with constant injection area, but varying size and number of uniformly distributed injection ports were considered. The airlift performance and efficiency were examined for a range of low submergence ratios. The intermediate hole size (4mm diameter) proved to be the most effective and efficient over the entire range of submergence ratios. The same trends associated with the submergence ratio previously stated in literature were also observed.

Bukhari [2] and Shallouf [36] conducted experiments on an airlift pump using the patented dual air injector by Badr and Ahmed [34]. Both a laboratory apparatus and field tests at an aquaculture facility were used to collect data. In the lab tests, only the submergence ratio was varied. The void fraction was measured near the middle of the riser using a capacitance sensor and values were reported by Bukhari [2]. In the field tests, different riser diameters were used at a fixed submergence ratio and riser length. Water discharge rate was the only quantity recorded in the field tests. Only the laboratory tests are reported in Table 2.1.

Wang *et al.* [37–40] conducted several analyses from one experimental setup. Wang *et al.* [37] analyzed the characteristics of the two-phase flow structures in the airlift riser by decomposing the pressure fluctuations with wavelet packet transform (WPT) and recurrence plots. The WPT decomposes the signal into different frequency ranges known as sub-signals. The energy distribution between the sub-signals provides insight into the flow characteristics that are otherwise difficult to observe. The recurrence plot is a way of visualizing the dynamic behaviour of the sub-signals. A pressure transducer located approximately one quarter of the way up the airlift riser was used to record the pressure fluctuations at a high sampling rate. The recurrence plots showed distinctly different characteristics for slug, slug-churn, and churn regimes considered by the authors. The chaotic fluctuations in the pressure increased with increasing the air flow rate. A periodic fluctuation in the high-frequency band was observed for slug-churn and churn flow, this was attributed to the motion of small bubbles entrained in the liquid.

Wang *et al.* [38] focused on airlift pumps operating in slug flow. A high speed camera was used to measure the Taylor bubble and liquid slug velocities, and a PIV system was used to measure the liquid film velocity. The high speed camera and PIV measurements were not synchronized due to conflicting lighting requirements. A mechanistic model of the slug flow was proposed based on a unit cell accounting for the coalescence of small gas bubbles between successive slugs. The measured slug flow parameters were compared against the theoretical prediction, and found to be in good agreement. The predicted Taylor bubble velocity, liquid velocity, and film velocity were within 14% of the experimental measurements.

Wang *et al.* [39, 40] used a high speed camera to visualize the flow in the riser, and LDV to study the flow in the airlift suction pipe. From the highspeed recordings of the flow, periodically occurring regions of falling liquid film, bubbly mixture, and ascending liquid film were observed and measured. The proportion of these aforementioned flow characteristics were plotted as a function of supplied gas flow rate and submergence ratio. The falling film decreased with increasing gas flow rate until it was no longer present. The opposite was observed with respect to gas flow rate for the ascending film. The occurrence of the bubbly mixture was essentially independent of gas flow rate but increased with increasing submergence ratio. The velocity of the liquid in the suction pipe was found to fluctuate considerably compared to classical two-phase flow. The fluctuations of liquid in-flow affect the two-phase flow structures in the airlift riser. Specifically, the flow transitioned from slug to churn flow more easily due to increased instability of the Taylor bubbles. Furthermore, wispy-annular flow was found to occur at high gas flow rates instead of the commonly reported annular flow regime. It was argued that the film thickness of annular flow is too thin to support the water flow rates seen on the airlift performance curve at high gas flow rates.

Zuo *et al.* [41] conducted an experimental investigation of different nozzle designs. Total inlet area and the size, shape, and distribution of holes was varied. A nozzle with small injection area increased pumping effectiveness at high airflow rate where the water flow rate typically plateaus. The injection pressure increased rapidly, however, with at higher air flow rates. Those findings are consistent with the similar work by Parker [18]. The hole shape (round vs. square) did not have a significant effect on the airlift performance or efficiency provided the total hole area was maintained. A significant effect of hole distribution was observed only for the smallest total injection area (25 mm^2) at high gas flow rates. The footpieces with one or two holes produced a higher liquid discharge rate and higher injection pressure than the footpiece with eight smaller holes.

Fayyadh *et al.* [42] performed experiments to evaluate an improved air injector design for an airlift pump operating at low submergence ratios. The air injector had 36 axial injection ports around the circumference of the pipe, similar to the axial component of the dual injector by Badr and Ahmed [34]. The injector developed by Fayyadh *et al.* [42], however did not have a radial component. The diameter of the suction pipe and air injector was larger than the riser pipe. A tapered section connected the air injector to the riser. The proposed air injector improved airlift performance and efficiency compared to a standard air injection system (of which complete details were not given). The optimum efficiency points coincided with either slug or churn flow regime.

Summary of Airlift Pump Experimental Conditions

The geometric configuration of the airlift pumps used in the aforementioned experiments are summarized bellow in Table 2.1. The maximum gas flow rate provides an indication of the range of flow regimes occurring in the airlift pump. Many airlift pump studies reported performance curves in units of mass flow rate, which is sensible when there is only one tube diameter. The superficial velocity, however is more appropriate for making comparisons between tubes of differing diameter. For the range of diameters seen in Table 2.1, the flow regime transition lines (based on the flow regime map of Taitel *et al.*) do not change appreciably with change in diameter.

Table 2.1: Summary of experimental studies.

Author	Year	L [m]	D [mm]	S_r	Air Injection	max J_G [m s^{-1}]
Stenning and Martin [15]	1968	4.27	25.4	0.44 – 0.71	AJ	10.5
Todoroki *et al.* [16]	1973	6.8,7.5	28.3, 50.6	0.4 – 0.8	AJ	7.15
Parker [18]	1980	1.28	38	0.6 – 0.82	AJ, N	2.0
Kouremenos and Staïcos [19]	1985	12 – 19	0.9	0.55 – 0.7	N	0.34
Clark and Dabolt [17]	1986	ns[1]	38	0.5, 0.70	T	0.5
Reinemann *et al.* [20]	1990	1.8	3 – 18	0.57 – 0.98	N	1.7
de Cachard and Delhaye [21]	1996	8	10	0.5, 0.70	T	4.0
Khalil *et al.* [22]	1999	2	25.4	0.5 – 0.75	N	2.3
Lawniczak *et al.* [23]	1999	1	30,50	0.2 – 0.6	N	12
Samaras and Margaris [43]	2005	ns	28, 40	0.6 – 0.8	ns	10
Castro *et al.* [24]	2005	0.3 – 3.7	12.7 – 76.2	0.4 – 0.7	ns	17
Kassab *et al.* [25]	2009	1.75 – 3.75	25.4	0.484 – 0.74	AJ	7.3
Moisidis and Kastrinakis [27, 28]	2010	3.1	30	0.3 – 0.6	N	12
Tighzert *et al.* [29]	2013	3.1	33	0.22 – 0.94	AJ	2.0
Hanafizadeh *et al.* [31]	2014	6	50	0.25 – 0.75	AJ	14
Kim *et al.* [32]	2014	0.5	8 – 24	0.8 – 1	ns	1
Ahmed *et al.* [33]	2016	2	31.75	0.5	AJ, D, S	7.5
Abou Taleb and Al-Jarrah [35]	2017	ns	50.8	0.18 – 0.49	AJ	3.5
Bukhari [2]	2018	1.57	31.8	0.5 – 0.9	D	3
Shallouf [36]	2019	1.57	25.4	0.9	D	4.5
Wang *et al.* [37–40]	2018	2.1, 2.8	40	0.3 – 0.7	T	13
Zuo *et al.* [41]	2020	1.5	30 – 50	0.3 – 0.9	N	2.1
Fayyadh *et al.* [42]	2020	2	31.75	0.15 – 0.3	unique[2]	10.4

1 ns indicates the information was not specified.

2 described in the prior discussion

Cross-Comparison of Published Airlift Pump Data

It is common practice in other areas of research to compare one's own experimental data to results published by others for a similar experiment. No such comparison has been made for airlift pump data. Admittedly, cross-comparison of airlift data is more challenging than standard pipe flow because dimensionless similarity cannot be used. In order to make a comparison, two nominal riser lengths ($L = 1.75$ m and $L = 3$ m) were selected such that multiple studies have data close to that of the nominal values. For the $L = 3$ m nominal length, a low and a high nominal submergence ratio was selected, $S_r = 0.4$ and $S_r = 0.7$, respectively. Only one nominal submergence ratio ($S_r = 0.5$) was available for the $L = 1.75$ m nominal length. The airlift pumps used in the experimental datasets grouped around the nominal configurations do not necessarily have the same air injector, as indicated in Table 2.1. The airlift pump performance curves for the nominal groupings are plotted together in Figure 2.1.

Some deviation between datasets is inherent to the slightly different riser lengths. With the exception of the Wang *et al.* [39] data, the relationship between liquid discharge rate and riser length of the datasets seen in Figure 2.1(a) are consistent with the established trend. The expected difference in magnitude, however, is unclear due to the additional uncertainty of the air injector effects. The results of Wang *et al.* [39] at the nominal tube length of 1.75 m are shifted towards much higher gas flow rates relative to other data.

For the $L = 3$ m nominal tube length shown in Figure 2.1(b and c), the variation seen between datasets by different authors is not consistent with the known trends of submergence ratio and tube length. Furthermore, the trends between datasets are not consistent between the two nominal submergence ratios shown. Overall, there is a fairly large degree of deviation between datasets in Figure 2.1, suggesting differences in the construction of the airlift besides submergence ratio, length, and diameter have a measurable effect on the airlift performance. Additionally, some of the scatter in the data may be attributed to measurement uncertainty.

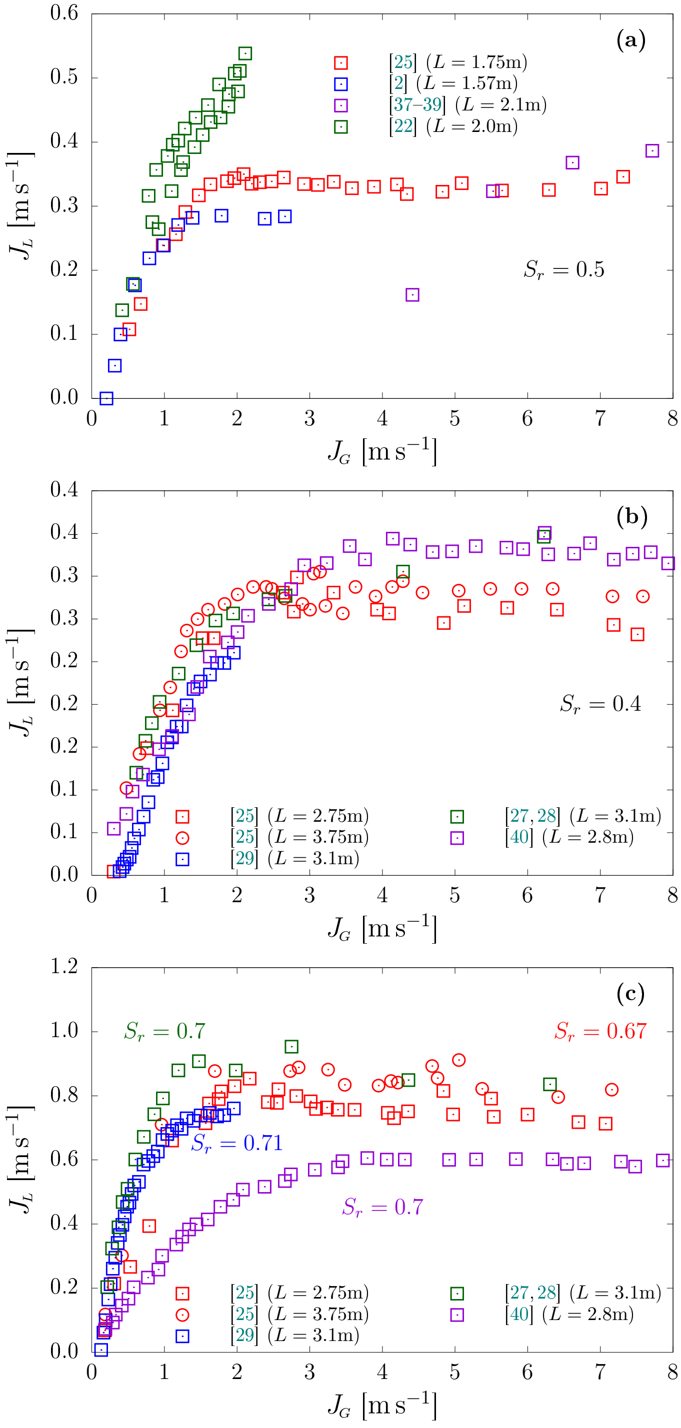

Figure 2.1: Comparison of performance curves for several published datasets. Nominal configurations of: (a) $L = 1.75$ m $S_r = 0.5$, (b) $L = 3$ m $S_r = 0.4$, and (c) $L = 3$ m $S_r = 0.7$.

Experimental measurements of average volume fraction in the airlift riser are available for a subset of the data considered in Figure 2.1. Data are available for the nominal riser length of 3 m but not at the same nominal submergence ratios. In general, the void fraction is a function of J_G and J_L; but in the case of the airlift pump J_L is a function of J_G, thus the void fraction can be presented as a function of J_G, as seen in Figure 2.2. The void fraction data of Wang *et al.* [40] is far less sensitive to change in submergence ratio than the data of Tighzert *et al.* [29]. The curves of void fraction from different sources are grouped more closely together than the performance curves.

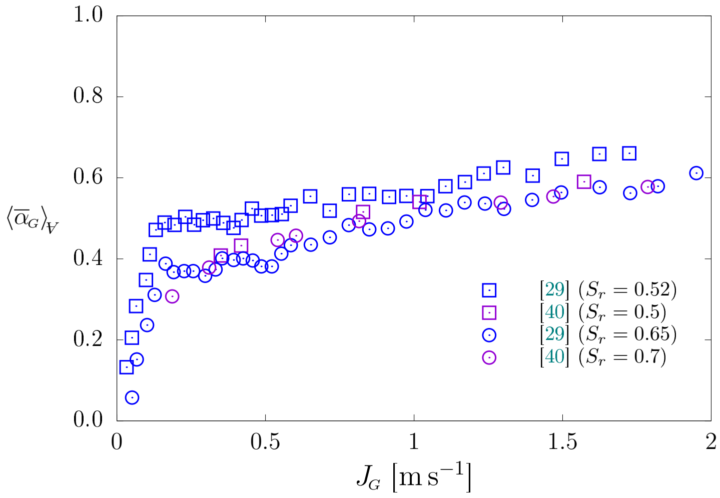

Figure 2.2: Comparison of average riser void fraction for several published datasets with a nominal riser length of 3 m and diameter of 35 mm.

2.1.2 Steady-State Algebraic Models

A number of simplified models for predicting airlift pump performance have been proposed in the literature. Although they have been derived in different ways, they share a number of similarities. The flow is assumed to be steady and represented by average quantities. Some form of conservation equation is written for the riser pipe. The forces acting on the two-phase flow in the riser are:

- The pressure differential between the bottom of the riser and the atmosphere ($\Pi_{\Delta P}$).
- The acceleration or momentum differential between the single phase liquid entering and the two phase mixture exiting ($\Pi_{\Delta \text{mom}}$).
- The weight of the two-phase mixture or the static pressure gradient (Π_{weight}).
- The wall shear force or frictional pressure drop (Π_{fric}).

The pressure at the bottom of the riser acts as a boundary condition to include the effect of submergence ratio. The momentum flux is approximated based on the bulk flow rates of each phase. Existing two-phase flow correlations are employed to predict the void fraction (required to determine the weight of the column) and frictional pressure drop. Accurate predictions of the void fraction and frictional pressure drop are essential for an accurate prediction of the liquid discharge rate because they are the dominant forces involved. Selecting an appropriate correlation often requires assuming a flow regime; typically slug or churn flow. The correlations required for closure assume steady and well-developed flow and neglect the unsteady nature of the two-phase flow in the airlift pump. Because the correlations required for closure are often complex functions of liquid flow rate, an explicit equation for liquid discharge rate is often not possible. Consequently, the majority of airlift models described below require an iterative solution technique.

Framework for Steady-State Airlift Model

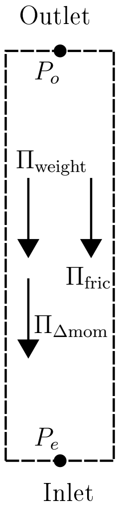

Figure 2.3: Forces acting on airlift riser control volume.

A control volume approach is adopted to express the steady-state (SS) models in a general form, as written below. The purpose of this general form is to demonstrate the similarity between models and summarize the different closure correlations used, as seen in Table 2.2. It does not fully describe the complete mathematical form of all models. The balance of forces acting on the control volume pictured in Figure 2.3 is mathematically expressed as:

$$\Pi_{\Delta P} = \Pi_{\text{weight}} + \Pi_{\text{fric}} + \Pi_{\Delta\text{mom}} \tag{2.3}$$

$\Pi_{\Delta P}$ represents the pressure difference from the entrance of the airlift pump to the outlet location.

$$\Pi_{\Delta P} = A(P_e - P_o) \tag{2.4}$$

P_o is taken as atmospheric pressure or 0 relative pressure depending on how P_e is defined. P_e is related to the hydrostatic head for a known submergence ratio. Many authors stated that singularity coefficients can be applied to account for the pressure drop across fittings at the outlet or inlet, although they are seldom applied. The specific expressions used in each model are summarized in Table 2.2.

$\Pi_{\Delta\text{mom}}$ represents the change in momentum experienced by the flow in the airlift.

$$\Pi_{\Delta\text{mom}} = \left[\int_A (\rho \boldsymbol{U}\boldsymbol{U}) dA\right]_{\text{out}} - \left[\int_A (\rho \boldsymbol{U}\boldsymbol{U}) dA\right]_{\text{in}} \tag{2.5}$$

Because the cross-sectional distribution of density and velocity is not known the integral must be approximated. In a 0-D or 1-D axial model only the bulk velocity and mass flow rate are available to calculate the momentum flux. The momentum flux at the inlet location represents the single phase liquid flow entering the airlift.

$$\int_A (\rho \boldsymbol{U}\boldsymbol{U}) dA \approx \dot{m}_L J_L \tag{2.6}$$

Similar expressions could be written for the gas phase should it be entering in the axial direction. The momentum flux of the two-phase mixture exiting the riser has been approximated in different ways, and are presented below under a discussion of the published models.

Π_{weight} represents the weight of the two-phase mixture in the airlift riser. As previously stated, the weight is proportional to the volume fraction. Neglecting the mass of the gas,

$$\Pi_{\text{weight}} = (1 - \alpha_G)\rho_L g L A \tag{2.7}$$

Π_{fric} represents the frictional pressure drop. Generally some empirical expression is used to relate a single-phase frictional loss to the frictional loss of the two-phase flow. The hypothetical single-phase frictional pressure drop is calculated using standard single-phase correlations for the friction factor. How the hypothetical single-phase velocity is defined (total volume flow or total mass flow) varies between two-phase modelling approaches.

Discussion of Published Models

Information regarding the correlations used to predict void fraction and frictional pressure drop is given as necessary in this section. A complete description of the correlations is provided in Appendix B

Nicklin [8] applied a theoretical analysis based on slug flow to the airlift pump. The pressure gradient in the riser was expressed as the sum of the hydrostatic and frictional pressure gradients. The analysis was limited to the riser and neglected the entrance and injector regions. The riser force balance equation was combined with the efficiency equation (Eq. (1.3)) to produce curves of theoretical maximum efficiency for the airlift pump.

Stenning and Martin [15] developed a model by combining force balances on the airlift riser and pipe in the air injector region. The gas was treated as incompressible. The force balance on the riser control volume consisted of the pressure differential, frictional pressure drop, and the weight of the column. It was assumed that there was no change in momentum across the riser control volume. Rather, the change in momentum was assumed to occur in the injector control volume. The injector control volume was assumed to be of negligible length relative to the riser, consequently the weight and frictional pressure drop were neglected. The conservation equations for the two control volumes were related to each other through the common pressure term. The slip ratio was assumed to be equal to one in the injector control volume, leading to

$$U_{L,o} = U_{G,o} \tag{2.8}$$

and the momentum differential as

$$\begin{aligned}\Pi_{\Delta\text{mom}} &= \dot{m}_L J_{\text{tot}} - \dot{m}_L J_L \\ &= \dot{m}_L (J_L + J_G) - \dot{m}_L J_L = \dot{m}_L J_G = \Pi_{\text{m1}}\end{aligned} \tag{2.9}$$

The shorthand Π_{m1} is used to represent this approach in Table 2.2. The void fraction in the riser was expressed as a function of the slip ratio. The authors present a correlation for the slip ratio based on the drift flux model of Griffith [44], but use a constant value of s for a given airlift performance curve. The two-phase frictional pressure drop was determined using the method proposed by Griffith and Wallis [45]. No equations for determining the friction factor were presented, instead a constant value of f was used. When calculating the airlift performance curve, the authors assumed constant values of $\frac{fL}{D}$ and s; however, this does not mean the frictional pressure drop and void fraction remain constant.

Todoroki *et al.* [16] applied a control volume to the airlift riser and suction pipe. The momentum was approximated using the bulk velocity of each phase as calculated based on the void fraction $U = \frac{J}{\alpha}$. The momentum differential becomes

$$\Pi_{\Delta\mathrm{mom}} = (\dot{m}_L U_{L,o} + \dot{m}_G U_{G,o}) - \dot{m}_L J_L = \Pi_{\mathrm{m2}} \tag{2.10}$$

The shorthand Π_{m2} is used to represent this approach in Table 2.2. The mass of the gas was neglected in the weight of the mixture and momentum differential. The model was compared against several experimental datasets for a range of riser lengths, $4\text{ m} \leq L \leq 42\text{ m}$. The error between the model and experiments increased significantly for the longer riser length of 42 m. The authors attributed the error to neglecting the expansion of gas and resulting increase of gas superficial velocity along the length of the riser in their model.

Parker [18] modified the Stenning and Martin model [15] for the prediction of airlift pump performance with a nozzle-style air injector. The same force balance was used for the riser, but a new force balance was written to better reflect the injector region. The same mixture momentum assumptions from Stenning and Martin were used with the additional contribution from the gas jet. The area of the jet was assumed to be 0.63 of the nozzle area. As with the Stenning and Martin model, constant values of friction factor and slip ratio were used. Consistent with the findings of Stenning and Martin [15], the friction factor required to give good agreement with the experimental measurements is higher than the theoretical value determined as if water were flowing alone at J_{tot}. The friction factor was better predicted by liquid flowing at the total mass flow rate.

Kouremenos and Staïcos [19] used a control volume approach that included the riser pipe and single phase entrance regions. The model accounted for change in slip ratio and friction factor as a function of flow rates. The authors demonstrated that the variation of slip and friction factor was necessary to predict a physically consistent functional relationship of $J_L = f({}^{J_G}/_{J_L})$. The model used a loss coefficient for the air injector that was correlated to the authors' own data (based on their 'perfect' slug flow injector) but a value was not given.

Clark and Dabolt [17] considered the forces acting on the flow in the riser in differential form. The pressure differential was integrated analytically over the length of the riser to obtain an implicit equation for water flow rate. This method allowed the authors to account for the change in air density and gas superficial velocity along the length of the riser. The effects of the air injector were not accounted for in the model. This model has limitations because the correlations for void and frictional pressure drop must be in an integrable form.

Reinemann *et al.* [20] assembled a model specific to small diameter airlifts where capillary effects are important. The gas was treated as incompressible. A single force balance was used for the riser, neglecting the change in momentum and the effects of the air injector. A drift flux model specific to small diameter pipes was used to determine the void fraction. The rise velocity of a Taylor bubble in still fluid was correlated to a function of Eötvösnumber (Eo). The model was presented using dimensionless flow rates $J^* = \frac{J}{\sqrt{gD}}$.

de Cachard and Delhaye [21] derived a model for an airlift pump operating in the slug and churn flow regimes. Separate analyses were performed for slug and churn flow, and then blended together to produce the final predictive model. The same drift flux model was used to predict the average void fraction in the slug flow and churn flow models. The slug flow and churn flow models differed in how the frictional losses were determined. The slug flow model used a unit cell approach accounting for the liquid slug and the falling film around the Taylor bubble. The churn flow model used a more empirical approach based on a separated two-phase flow model. The frictional pressure drop predicted by the churn model is greater than that of the slug model. The experimentally measured frictional pressure drop more closely matched the slug model prediction at low flow rates, and trended towards the churn predictions at higher flow rates. This behaviour was attributed to the gradual transition from ideal slug flow to churn flow. Consequently, the frictional pressure drop in the final airlift model was interpolated between the slug and churn models as a function of dimensionless gas superficial velocity. The authors neglected the momentum and weight of the gas phase. An expression for the differential pressure was assembled and numerically integrated along the length of the riser assuming a linear change in gas density. The pressure at the entrance and outlet of the riser were used as boundary conditions for the integrated expression and the pressures at the entrance of the riser was determined using a Bernoulli equation accounting for losses in the upstream piping. The presented model accurately predicted airlift performance for both the authors' own experiments and the experiments conducted by Reinemann *et al.* [20]. de Cachard and Delhaye demonstrated their model provides superior predictions of airlift pump performance than the model by Reinemann *et al.*, especially at higher gas flow rates where the Reinemann *et al.* model overpredicts the frictional pressure drop.

Kassab *et al.* [25] modified the 0-D model by Stenning and Martin [15] to account for the change in slip ratio and frictional pressure drop with change in flow rate. The same correlation for slip ratio was used as suggested by Stenning and Martin, but the value was calculated as a function of the flow rates, meaning it was iterated as part of the solution for liquid discharge rate. The friction factor was calculated in a similar manner using the Colebrook equation by Haaland [46]. Care must be taken when using the model to ensure the frictional pressure drop is calculated properly. Stenning and Martin [15] used the Fanning friction factor; however, the Colebrook equation is for the Darcy-Weisbach friction factor, which is 4 times the Fanning friction factor.

Ahmed *et al.* [33] wrote a momentum balance model to account for their dual air injector. The momentum differential is calculated using Π_{m2} plus the momentum flux of the gas injected axially. As with the Kassab model, the values of the frictional pressure drop and the void fraction were updated at each air flow rate, but different correlations were used.

Yoshinaga and Sato [47] proposed a 1-D area-averaged model to predict airlift performance with or without solid particles. Wang *et al.* [39] adapted this model for gas-liquid flow. The 1-D approach divided the airlift riser into a number of smaller control volumes along the length. The force balance on each control volume is essentially the same as the 0-D models previously discussed. The 1-D model allowed for the air density and superficial velocity to change along the length of the riser. The effects of the air injector were accounted for with a singularity pressure drop coefficient. The 1-D model also extended to the single phase entrance pipe.

Using the base modeling approach of Kassab *et al.* [25], Bukhari [2] assembled an airlift model accounting for multiple flow regimes. The gas-liquid flow regime was determined using the transition criteria from Taitel *et al.* [12]. The closure correlation for void fraction was selected for the appropriate flow regime. Although bubbly to slug, slug to churn, and churn to annular transitions were considered in the modeling, slug to churn transition was the only regime change observed in practical airlift operation. The piecewise nature of the model results in a discontinuity of the airlift performance curve at the regime transition point. Only the void fraction correlation for the slug flow regime is reported in Table 2.2. Alternative correlations were not considered for the frictional pressure drop. The agreement of the model was within 50% for nearly all experimental comparison points.

Analogous to the modifications made by Kassab *et al.* [25] to the Stenning and Martin model, Zuo *et al.* [41] included the calculation of slip ratio and friction factor in the model equation by Parker [18]. The model gave excellent predictions for the limited conditions tested.

Summary of Auxiliary Relations

The axillary relations used in the SS models are summarized in Table 2.2. The drift flux approach is denoted by DF and the model coefficients are given when applicable. Details of the correlations listed in Table 2.2 can be found in Appendix B.

Table 2.2: Summary of auxiliary relations used in the steady-state models.

Author	void fraction	two-phase frictional pressure drop	friction factor	$\Pi_{\Delta\text{mom}}$	P_e
Nicklin [8]	DF: $C_0 = 1.2$, $v_d = 0.35\sqrt{gD}$	$(1-\alpha_G)\left(\frac{dP}{dx}\right)_{(G+L)}$	not specified	0	Na
Stenning and Martin [15]	DF: $C_0 = 1.2$, $v_d = 0.35\sqrt{gD}$	GW: $\frac{J_L}{J_\text{tot}}\left(\frac{dP}{dx}\right)_{(G+L)}$	constant $\frac{fL}{D}$	Π_m1	$\rho_L g H_S - \frac{1}{2}\rho_L J_L^2$
Todoroki *et al.* [16]	DF: $C_0 = 1.2$, $v_d = 0.35\sqrt{gD}$	$(1-\alpha_G)^{-1.75}\left(\frac{dP}{dx}\right)_\ell$	not specified	Π_m2	$\rho_L g H_S - \frac{1}{2}\rho_L J_L^2$
Parker [18]	DF: $C_0 = 1.2$, $v_d = 0.35\sqrt{gD}$	GW: $\frac{J_L}{J_\text{tot}}\left(\frac{dP}{dx}\right)_{(G+L)}$	constant $\frac{fL}{D}$	$\Pi_\text{m1} - \rho_G J_G\left(\frac{J_L}{0.63 A_N}\right)$	$\rho_L g H_S - \frac{1}{2}\rho_L J_L^2$
Kouremenos and Staïcos [19]	DF: $C_0 = 1.2$, $v_d = 0.345\sqrt{gD}$	$(1-\alpha_G)^{-1.75}\left(\frac{dP}{dx}\right)_\ell$	Blasius [48]	Π_m1	$\rho_L g H_S - \frac{1}{2}\rho_L J_L^2$
Clark and Dabolt [17]	DF: $C_0 = 1.2$, $v_d = 0.35\sqrt{gD}$	L-M simplified $\phi(1+1.5\alpha_G)$	0.01	0	$\rho_L g H_S$
Reinemann *et al.* [20]	DF: $C_0 = 1.2$, $v_d = \Gamma\sqrt{gD}$, see App. B.1.1	$(1-\alpha_G)\left(\frac{dP}{dx}\right)_{(G+L)}$	Blasius [48]	0	$\rho_L g H_S$
de Cachard and Delhaye [21]	DF: $C_0 = 1.2$, $v_d = \Gamma\sqrt{gD}$, see App. B.1.1	combination of slug unit and general churn	Blasius [48]	Π_m2	$\rho_L g H_S - \frac{1}{2}\rho_L J_L^2 - \text{losses}$
Kassab *et al.* [25]	DF: $C_0 = 1.2$, $v_d = 0.35\sqrt{gD}$	GW: $\frac{J_L}{J_\text{tot}}\left(\frac{dP}{dx}\right)_{(G+L)}$	Colebrook [46]	Π_m1	$\rho_L g H_S - \frac{1}{2}\rho_L J_L^2$
Ahmed *et al.* [33]	LM: see Eq. B.9	LM: $\phi_\ell^2\left(\frac{dP}{dx}\right)_\ell$	Colebrook [46]	Π_m2	$\rho_L g H_S$
Wang *et al.* [39]	Smith [49], see App. B.1.2	Based on [50,51]		Π_m2	$\rho_L g H_S$
Bukhari [2]	DF: $C_0 = 1.2$, $v_d = 0.35\sqrt{gD}$	GW: $\frac{J_L}{J_\text{tot}}\left(\frac{dP}{dx}\right)_{(G+L)}$	Fang *et al.* [52]	Π_m1	$\rho_L g H_S - \frac{1}{2}\rho_L J_L^2$
Zuo *et al.* [41]	DF: $C_0 = 1.2$, $v_d = 0.35\sqrt{gD}$	GW: $\frac{J_L}{J_\text{tot}}\left(\frac{dP}{dx}\right)_{(G+L)}$	Colebrook [46]	$\Pi_\text{m1} - \rho_G J_G\left(\frac{J_L}{0.63 A_N}\right)$	$\rho_L g H_S - \frac{1}{2}\rho_L J_L^2$

The high degree of similarity between SS models can largely be attributed to five of the thirteen models being derivatives of Stenning and Martin [15]. The drift flux model is the most commonly used technique for determining the void fraction of the models shown in Table 2.2. Some authors, namely Reinemann *et al.* [20] and de Cachard and Delhaye, use different correlations for the drift flux coefficients that include more parameters in order to make them valid for a wider range of gas-liquid flow phenomena. For standard air-water flows, the more detailed correlations produce essentially the same drift velocity as the common $v_d = 0.35\sqrt{gD}$. The correlations used to determine the friction factor are not a significant source of deviation between airlift pump models given that there is much greater uncertainty in other areas. It is therefore justified to use a simple explicit equation for convenience instead of the Colebrook equation (implicit). The two-phase frictional pressure drop and momentum differential prediction are the most significant point of difference among the SS models. The accuracy of these closure relations will be compared against the CFD results of the present work in Section 5.5.1.

2.1.3 Numerical Studies of Airlift Pumps

Considerable effort has been spent developing simplified numerical models for airlift pimps with very long riser pipes (20 to 1600 m) typically used in deep sea mining or artificial ocean upwelling. Full-scale experiments are far more expensive than for short-riser airlift pumps. Due to the enormous length scale, detailed 3-D numerical simulations are not feasible. A variety of different numerical techniques have been used, for example: Tomiyama *et al.* [53] used a steady-state 1-D area averaged two-fluid model, Kajishima and Saito [54] used a transient 1-D drift flux model, Pougatch and Salcudean [55,56] used a transient 2-D axisymmetric multi-fluid model, and Meng *et al.* [57] used a transient Euler-Lagrange model. The applicability of these methods to shorter airlift pumps largely depends on whether the flow regimes are consistent. Due to the nature of the tasks long-riser airlift pumps are typically used for, they operate at a high submergence ratio. Because the submergence ratio is very close to 1, and the expansion effects of the gas are considerable, a relatively small gas flow rate was needed to lift the liquid. Consequently, the flow is modeled as bubbly rather than the slug or churn flow patterns associated with the shorter airlift pumps. This suggests the aforementioned numerical models are not the ideal choice for simulating the flow in short length airlifts.

Hanafizadeh *et al.* [58] derived a 1-D steady-state two-fluid model applicable to the riser pipe of an airlift pump. The work focused on extending the single-phase Physical Influence Scheme to the solution of two-phase flow. The proposed numerical technique compared well against similar numerical methods. The gas and liquid flow rates were specified in the boundary conditions. Therefore, the ability of the numerical model to predict the air lift pump performance was not accessed.

Hanafizadeh *et al.* [59, 60] applied a 3-D steady-state two-fluid model to the study of airlift pumps with either a tapered riser pipe or a step expansion of the riser pipe. The interfacial area (required for closure of the two-fluid model) was determined by a correlation for equivalent particle diameter. In both articles, details of the interfacial closure and boundary conditions were unclear. The airlift pump performance predicted by the numerical results were in good agreement with experimental results published by others.

Hanafizadeh *et al.* [61] evaluated the ability of multiphase CFD techniques in commercial CFD codes to model the gas-liquid flow structures in the airlift. The flow rates of both phases were specified in the modeling, so that the airlift pump performance was not actually predicted. Regardless of the short comings of the numerical modeling, the homogeneous VOF model was found to produce more physically realistic flow structures than the two-fluid model.

Li *et al.* [62] simulated an airlift pump with a small diameter (12 mm) riser using a homogeneous RANS VOF model. The flow was assumed to be 2-D axisymmetric and incompressible. The continuum surface force (CSF) model was used for surface tension effects, and wall adhesion was specified. A time-dependent solution was obtained using ANSYS Fluent. The turbulence model used to close the RANS equations was not specified. Qualitatively, the CFD model resolved physically reasonable slug flow behaviour consistent with the expected flow regime. The airlift performance was over predicted by approximately 10%. The oscillations in water eduction rate increased with increasing gas flow rate.

Wahba *et al.* [63] used a homogeneous LES VOF model to simulate select experiments from Kassab *et al.* [7]. The Smagorinsky model with a van Driest damping function was used to approximate the subgrid scale stress tensor. The CSF model was used in the filtered equations, and the contributions of the surface tension force on the subgrid scale were neglected. A complete 3-D computational domain including the airlift riser, air jacket, suction pipe and feed tank was simulated. Zero relative pressure boundaries were applied to the riser outlet and free surface of the supply tank. Approximately 3 million cells with a tetrahedral core and prism layer at the wall were used in the working mesh. The liquid flow rate predicted by the simulation was within 10% of the experimental results.

Alasadi and Habeeb [64] performed a 2-D axisymmetric simulation using the homogeneous VOF model in ANSYS Fluent. A time-dependent solution method was used. The predicted airlift performance compared well with the authors' own experiments.

Shallouf *et al.* [36, 65] used ANSYS Fluent to simulate an airlift pump for aquaculture applications using a homogeneous VOF model. A $k-\varepsilon$ turbulence model was applied to the homogeneous velocity field. The computational domain consisted of a quarter tube (90° segment of the airlift riser) and air injector including the internal structures. Zero gradient boundaries were applied to the symmetry planes. A pressure boundary equal to the hydrostatic head of the stationary water column was assigned to the suction pipe. This pressure boundary imposed the submergence ratio on the simulation. Single-phase simulations were performed on the air injector region to study the flow in the patented dual air injection device. Steady-state simulations were used to assess the mesh sensitivity for the two-phase simulations, but the liquid discharge rate predicted by the steady-state simulations was 2 to 6 time greater than predicted by the transient simulations performed with the working mesh. The airlift performance was predicted within 25% of the authors' own experimental measurements. Contours of void fraction were qualitatively compared to images captured from the experiment.

2.1.4 Stability Analysis

The steady state airlift models discussed in Section 2.1.2 average out the true transient nature of the airlift pump. The average discharge rate alone does not completely describe the operation of the airlift pump. The liquid eduction rate will always fluctuate to some degree due to the inherent transient nature of the two-phase flow regimes the airlift operates in; however, the airlift is considered unstable when the flow rates fluctuate beyond the normal threshold. In the worst case scenario, the airlift riser completely empties then refills with liquid in a repeating manner. Unstable behaviour can occur at certain operating points, typically below a critical submergence ratio. Violent, low frequency, large amplitude oscillations of the liquid discharge rate are undesirable in many applications. Consequently, several authors have attempted to identify the sources of instability, and factors influencing the propagation of instabilities in the system.

Hjalmars [66] theorized that the instabilities observed in airlift pumps were caused by the failure of the airlift to act as a self-controlling system. In order to mathematically describe the time-dependent perturbations of the system, many assumptions were made. The two-phase flow in the riser was modeled as a frictionless homogeneous mixture, and the liquid was assumed to be supplied from a stationary basin. Apazidis [67] built on the work of Hjalmars, more appropriately modeling the flow with an algebraic slip ratio two-fluid model and accounting for compressibility effects of the gas, but wall friction was still neglected. Predicted critical lift and oscillation period were in reasonable agreement with the experimental measurements and captured the relevant trends. The period of oscillation decreased with increased gas flow rate.

de Cachard and Delhaye [68] performed linear stability analysis using a time dependent version of their 0-D momentum balance model. The momentum balance model of de Cachard and Delhaye is more sophisticated than the models used by Hjalmars [66] and Apazidis [67] for the airlift riser, because it accounts for all relevant physical phenomena. Furthermore, de Cachard and Delhaye expanded the scope of the stability analysis to account for the effects of single-phase liquid and gas supply. The flow inertia from the liquid supply line and compressibility in the gas supply line were found to play significant roles in the stability of the airlift pump. An empirical stability criterion was proposed for engineering applications.

2.1.5 Miscellaneous Gaslift Studies

Several non-standard riser geometries have been studied. Mahrous [69] studied the effect of bends in an S-shaped riser using a momentum balance model. Hanafizadeh *et al.* [59] and Zaraki *et al.* [70] found an airlift with a tapered expanding riser improved the performance and efficiency, but narrowed the operating range, compared to a conventional airlift. Hanafizadeh *et al.* [60] found a riser expanding in steps to be more effective than the standard riser geometry. Rectangular cross-section risers were studied by Ligus *et al.* [71], Essen [72], and Tramba *et al.* [73]. Sohn *et al.* [74] experimentally studied the airlift performance and two-phase flow structures in an airlift with a blunt body inserted along the centerline of the riser. Oueslati and Megriche [75] studied the effect of temperature and humidity on airlift performance. Dare and Oturuhoyi [76] collected experimental data for airlift pumps operating at different diameters and submergence ratios with different working liquids. Dimensional analysis was applied, resulting in a pump dimensionless number (PDN), and a lift dimensionless number (LDN). The experimental data had an approximately linear relationship when LDN was plotted vs PDN. Catrawedarma *et al.* [77] experimentally studied a bubble generator driven airlift pump. The bubble generator is an alternative method to typical air injectors, which improved airlift performance. The airlift performance results of Catrawedarma *et al.* [77] cannot be directly compared to standard airlift pumps, but their method of analysis is transferable. Differential pressure transducers were used to record instantaneous fluctuations in pressure. The pressure signals were used to perform a statistical analysis of the flow patterns using well established PDF and FFT methods.

For examples of airlift pumps operating in three-phase flow an interested reader is directed to: Tomiyama *et al.* [53], Yoshinaga and Sato [47], Kassab *et al.* [7], Moisidis and Kastrinakis [28], Hu *et al.* [78], and Ramdhani *et al.* [6]. Hanafizadeh and Ghorbani [1] conducted a thorough review of information regarding airlift pumps published prior to 2012. The supporting two-phase flow theory, airlift modeling techniques, past experimental studies, and common applications of airlift pumps were covered.

2.1.6 Summary

Performance Trends

Overall, the effect of riser length, riser diameter, and submergence ratio on airlift pump performance have been well established in the literature. Increasing length and submergence ratio increases liquid discharge rate, effectiveness, and efficiency [22, 24, 25, 29]. The average volume fraction in the riser is proportional to the gas flow rate and inversely proportional to the submergence ratio [29, 40]. The riser diameter has a significant effect on small diameter tubes (3 to 19 mm) and a negligible effect on moderate diameters (20 to 50 mm) [20, 21]. This distinction occurs because of the capillary force's influence on the two-phase flow structure in small diameter pipes. For small diameter airlift pumps, the maximum effectiveness and efficiency are inversely related to the diameter [20, 32]. Regardless of riser diameter, it has consistently been shown that the optimum efficiency does not correspond to the maximum discharge rate or peak effectiveness [25, 42]. In general, efficiency increases with increase in submergence ratio [18, 25, 29]. Tighzert *et al.* [29] observed that the airlift efficiency decreases beyond a critical high submergence ratio ($S_r = 0.75$ in their work), but this value is likely to depend on the specific air injector used.

Effect of Air Injector

Attempts have been made to design more effective and efficient air injectors [33]. Different air injectors have been shown to affect the discharge rate [18, 19, 22, 23, 41, 42]. The role of specific parameters such as total injection area, injection area distribution, and direction have not been quantified. Nozzle-style air injectors with a small injection area have consistently been shown to improve the liquid discharge rate in region III of the performance curve but the efficiency is not optimal [18, 41]. Consequently, the nozzle style air injector does not provide a practical advantage over other air injection methods.

Prevalence of Two-phase Flow Regimes in Airlift Pumps

It has repeatedly been shown that the airlift pump does not operate in bubbly flow under normal operating conditions [1, 25, 27, 29, 43]. Bubbly flow will occur in region I of the performance curve (Figure 1.2) where the gas flow rate is insufficient to discharge liquid. If $S_r \to 1$, liquid may be discharged during the bubbly flow regime. As previously stated, this situation of very large submergence ratio does not commonly occur in practical applications. Slug and churn flow regimes span the majority of the performance curve, particularly region II which has the most significance for practical operation. The optimum efficiency occurs in region II, with either slug or churn flow. The presence of annular flow in airlift pumps is debated by some authors [27, 40]. The gas flow rate required to enter the range of annular flow is well into region III of the performance curve. The airlift effectiveness and efficiency at the high gas flow rate are far below the optimal values. Therefore, the two-phase flow pattern at high gas flow rates is not of critical importance for practical use of airlift pumps. Moreover, many of the experimental studies in Table 2.1 do not have gas flow rates exceeding the superficial velocity required to initiate annular flow (approximately 10 $\mathrm{m\,s^{-1}}$).

2.2 Numerical Modeling of Slug and Churn Flow

It has been shown in Section 2.1.3 that no single technique has been used consistently to simulate the two-phase flow in the airlift pump. There is more insight to be gained from the plentiful literature available on the numerical modeling of standard two-phase flow. The wide range of interfacial length scales and distinctly different flow regimes makes the universal modeling of multiphase flows essentially impossible. Different multiphase modeling techniques are used depending on the flow regime, as discussed in Appendix A.2. It has been well established slug and churn flow are the primary flow regimes occurring in the airlift, so the following discussion of multiphase CFD techniques is limited to those regimes.

Slug Flow

Slug flow can be modeled using the general purpose homogeneous VOF model, or slug-flow specific models where the frame of reference is attached to a gas slug and periodic boundary conditions limit the domain to one or several slug units [79]. The slug-specific models are not appropriate to the general prediction of the flow in an airlift pump. Many authors have demonstrated the capabilities and limitations of a homogeneous VOF model to simulate slug flow [80–85].

Churn Flow

Montoya *et al.* [86] published an excellent review of modeling techniques for churn flow. Churn flow is an especially difficult flow regime to accurately capture due to the wide range of interacting length scales and highly turbulent nature [86]. The homogeneous VOF model has been applied with limited success. The two primary shortcomings of the homogeneous approach are the effects of small bubbles and droplets are lost and the uncertainty in the accuracy of the turbulence modeling [87]. Multi-scale large interface capturing approaches have shown promise in modeling churn flow because they can better capture the effects of small interfacial scales lost in the homogeneous model [88].

Modelling Considerations for Homogeneous VOF Approach

Hernandez-Perez *et al.* [89] demonstrated that the type of mesh construction had an impact on the phase distribution and two-phase flow structures predicted by the simulation. The authors simulated slug and churn flows using a homogeneous VOF multiphase model, the predicted phase distribution was compared to wire mesh sensor (WMS) and electrical capacitance tomography (ECT) experimental measurements. The half pipe simulations did not produce physically reasonable flow structures. Of the full pipe meshes tested, the rectangular O-grid type (used in Figure 4.7) mesh was recommended because it produces a physically consistent phase distribution, and is flexible for refining the mesh near the wall.

The work of Tekavčič *et al.* [90] also found that a full 3-D domain is required to faithfully predict the phase distribution of churn flow. Numerical results from 2-D axisymmetric homogeneous VOF models in CFX, Fluent, and 2-D and 3-D multi-scale models in Neptune CFD, of the same experiment were compared. The 2-D simulations were prone to a physically unrealistic accumulation of liquid in the centre of the pipe. This phenomena was explained by considering what happens when a mass of liquid breaks away from the wall and travels towards the centre of the pipe. With the symmetry boundary conditions, the liquid mass is met by an identical amount of liquid mass traveling in the exact opposite direction, causing the liquid mass to repel and accumulate near the centre, leaving a ring of gas between the centre and the wall. In reality, the probability of the water mass being repelled by an identical one is incredibly low due to the turbulent antisymmetric nature of the local instantaneous flow field.

The homogeneous VOF model typically requires a finer mesh and is more sensitive to mesh density than the two-fluid model [91]. Because the homogeneous assumption (shared velocity within a control volume) breaks down in highly dispersed regions, it is imperative to resolve a sharp interface between phases. This is accomplished in two ways: controlling the mesh density, and using an interface sharpening or reconstruction scheme. Yeoh and Barber [92] published a comprehensive test and review of both interface sharpening and reconstruction schemes for the homogeneous VOF model. The compressive interface sharpening scheme required a finer mesh than reconstruction schemes but was more numerically stable and less computationally expensive for an equivalent mesh.

2.3 Motivation

Although the major trends in airlift pump performance are widely accepted, there are many inconsistencies between the work done by different authors. The definition of submergence ratio, specifically where the total length is measured from, varies from author to author. The air injection pressure is not always determined from the same location when calculating efficiency per the definition by Nicklin. Furthermore, different definitions of efficiency are sometimes used [31, 41].

No standard set of flow regimes and regime transitions are used between authors. For example, Kassab *et al.* [25] considered slug, slug-churn, and annular flow patterns, whereas Wang *et al.* [40] considered slug, churn, whispy annular, and annular flow patterns. The inconsistent definition of churn flow is not unique to the study of the airlift pump; rather, this same problem occurs in other two-phase flow literature [86].

Flow maps by Hewitt and Roberts [14], and Taitel *et al.* [12] have both been used for predicting the flow regime in airlift pumps, but they predict very different transitions between slug and churn flow. The slug to churn flow transition is the most important regime transition for the airlift pump because the optimum efficiency point is commonly located near this transition. To further complicate the matter, the work of Moisidis and Kastrinakis [27] suggests the flow regime transition in airlift pumps is better described as a function of the submergence ratio. The flow map presented by Moisidis and Kastrinakis [27] cannot be considered universally applicable to all airlifts because of the small sample of data used.

The majority of experimental studies of airlift pumps only report the liquid discharge rate. State-of-the-art experimental techniques for measuring gas-liquid flow structures have not been used for the airlift pump. Flow regime identification has typically been performed visually, if at all. Visual identification of flow regimes is prone to error and inconsistency as discussed in Section 1.1.2. Moisidis and Kastrinakis [27] used conductivity probes, but the time signals were only compared qualitatively; no statistical means were used to characterize the flow. The value of statistical analysis was demonstrated by Ramdhani *et al.* [6] who used PDFs to characterize difference in flow structures between airlifts operating in two-phase and three-phase flow. Furthermore, Catrawedarma *et al.* [77] performed a thorough statistical analysis of the two-phase flow patterns in a bubble-pump driven airlift. Wang *et al.* [37] used signal processing methods to study the flow, but their performance curve data are not consistent with other works, as seen in Figure 2.1(a).

The experimental study of airlift pumps presents additional challenges compared to standard two-phase flow. Because the liquid flow rate in the airlift pump is driven by the pressure gradient, intrusive measurement techniques will affect the flow structures in the airlift riser, and in turn alter the liquid discharge rate. Consequently, popular two-phase measurement tools such as WMS cannot be used for airlift pumps.

The steady-state algebraic models provide a reasonable estimation of liquid discharge rate for many engineering applications. These simplified models however, are not useful for design optimization studies because they do not account for the details of the air injector or the dynamic nature of the system. The dynamic model of de Cachard and Delhaye [68] does provide great insight into the instabilities of the flow in an airlift pump, yet it also does not account for the details of the air injector. The stability analysis of the airlift pump suggests the inlet pressure constraint has an effect on the two-phase flow patterns in the airlift riser due to the oscilations in the liquid flow rate. The details of the two-phase flow structures, however, are not resolved in the simplified model. Thus, more advanced modeling techniques are required to improve the fundamental understanding of the flow and lead to better airlift pump designs.

Three-dimensional CFD modelling has the capability of accounting for the air injector and providing information about the local flow structures in the airlift riser. Three-dimensional CFD modeling has not been used as extensively to study the airlift pump as experimental means. Only two instances of 3-D CFD modeling of an airlift pump were found in the literature, namely Shallouf *et al.* [65] and Wahba *et al.* [63]. Considering the pertinent information given in Section 2.2, from the more established field of CFD modeling of standard two-phase flow, the CFD modeling of airlift pumps can be revisited with a more critical lens. Given the large length scales of the problem, the RANS approach is reasonable. The use of an LES model by Wahba *et al.* [63] is an uncommon choice for slug or churn flows. LES turbulence modeling can be used for a range of mesh densities; the coarser the mesh the less the turbulence modeling deviates from RANS, conversely the finer the mesh, the more the modeling approaches DNS. The mesh density used by Wahba *et al.* [63] is on the coarser end of the spectrum. The validity of the $^1/_4$ pipe symmetry boundaries used by Shallouf *et al.* [65] is in doubt because of the findings of Hernandez-Perez *et al.* [89] and Tekavčič *et al.* [90]. The use of steady-state simulations to determine mesh sensitivity of a simulation that requires a time dependent solution is not common practice.

It is worth emphasizing that Wahba *et al.* [63] and Shallouf *et al.* [65] compared the predicted liquid discharge rate against experiment and the flow pattern was essentially studied visually through the inspection of contour plots. Regardless of the quality of their modeling techniques, neither work explored the details of the two-phase flow structures. The examination of void fraction contour plots from the CFD results is analogous to the study of high-speed camera snapshots of the flow from an experiment. Such visual inspection does not provide the same depth of information as a statistical analysis of the two-phase flow structures. An advantage of CFD simulations over experimental studies is more information about the flow can be acquired at many locations more easily. Neither work of Shallouf *et al.* [65] or Wahba *et al.* [63] fully utilized the depth of information available from CFD simulation results.

Considering the summary of the literature presented, it is evident the liquid discharge rate is a result of the two-phase flow structures occurring in the airlift riser, and the the liquid discharge rate varies with airlift configuration. Therefore, the two-phase flow structures are sensitive to the airlift configuration. Understanding of the characteristics of the two-phase flow structures in airlift pumps is lacking. It has not been established how the inlet pressure constraint of the airlift pump affects the two-phase flow patterns occurring in the riser pipe. CFD modelling is an effective tool to address these shortcomings in the existing understanding of airlift pumps.

Chapter 3

Mathematical and Numerical model

It was indicated in Section 2.2 that a homogeneous VOF type of model is an appropriate choice for simulating the flow in the airlift pump. Further justification and background information supporting why the homogeneous VOF approach was used in the present work is provided in Appendix A.2.

The homogeneous VOF model requires the mesh to be fine enough to resolve discrete regions of either phase. Because of the assumption of shared velocity within a control volume, no interfacial momentum transfer closure is required. The present modeling focuses on the hydrodynamics of the flow; heat and mass transfer between phases is not considered.

3.1 Domain Definition

Figure 3.1 shows a generic computational domain for the airlift pump adopted in this work. It consists of the riser, air injector region, and entrance pipe. The internal structures of the air injector are not included in the computational domain. The short length of entrance pipe maintains consistency with experimental apparatus, and improves numerical stability of the liquid inlet boundary condition. It is not good practice to have a boundary condition near a region where recirculation and complex flow occurs.

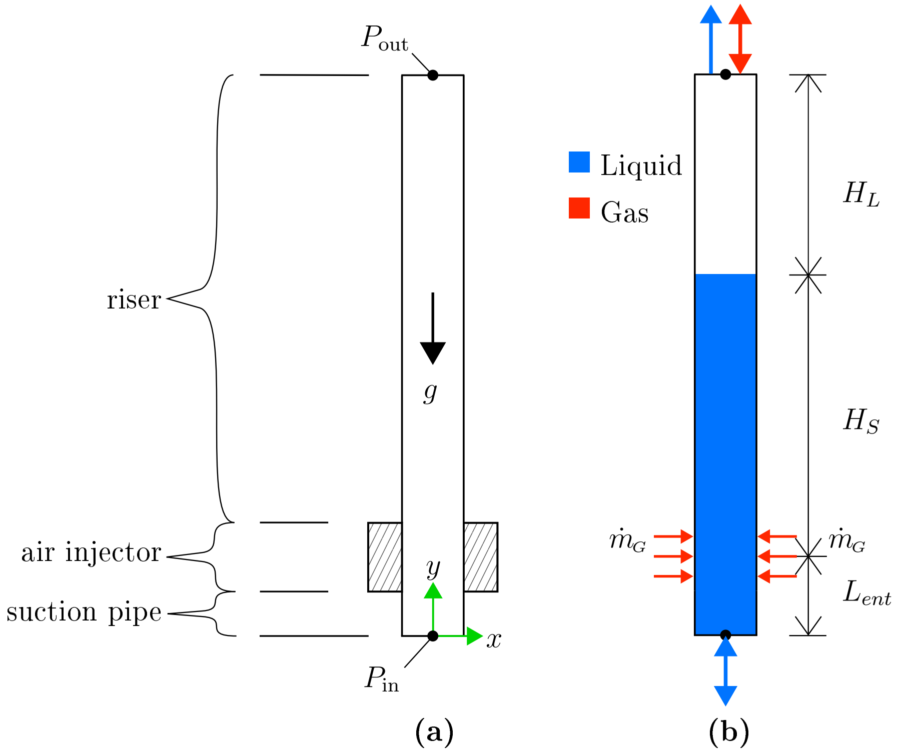

Figure 3.1: Simplified computational domain for modeling an airlift pump. (a) Shows a schematic of the generic airlift pump section to be modeled. (b) Shows the initialization state and the direction of flow prescribed to the boundaries.

The liquid inlet pressure boundary condition is an essential part of a predictive simulation of airlift pump performance. Firstly, it allows the liquid flow rate to be an implicit result of the simulation. Secondly, the magnitude of P_{in} imposes the value of the submergence ratio on the simulation. The inlet condition is specified as an opening (indicated by a double arrow) such that liquid can flow into the domain or any fluid can flow out, depending on the local pressure gradient. The air flow rate is specified as a boundary condition because it is a specified input condition to the airlift pump. A complete description of the specification of the boundary conditions are given in Section 3.2.2. The details of how the air is supplied to the air injector depend on the particular physical conditions of interest, which are specified in Section 4.1.

3.2 Governing Equations

The governing equations and their solution strategy are provided for the homogeneous VOF model in ANSYS CFX (version 19.2). This model is referred to as the homogeneous free surface model in the CFX documentation. The flow is assumed to be isothermal with no mass transfer. The liquid phase is incompressible, whereas the gas phase is treated as an ideal gas. The equations are given in a generic form for N many phases where applicable; however, the flow in the airlift consists of two phases, liquid and gas.

3.2.1 Homogeneous Multiphase Model

In any given control volume (CV) the phases are assumed to have the same velocity. In the case of the present simulation, $\boldsymbol{U_G} = \boldsymbol{U_L} = \boldsymbol{U}$. In instances where there are discrete regions of only one phase, the velocity will be that for only one of the phases, which may be different from the velocity representing another region of a discrete phase nearby. For example, in the case of Taylor bubbles in a slug flow, the gas pockets rise with a relative velocity to the surrounding liquid because each discrete region is comprised of many CVs, each with its own velocity. The assumption of shared velocity within a CV does not represent the flow well in highly dispersed regions where discrete phasic interfaces cannot be resolved by the length scales of the mesh.

Because of the shared velocity assumption, the volume fraction within a CV is equivalent to the void fraction, α. For consistency with the presentation of results in later sections α is used in the following equations, however strictly speaking the equations are based on volume fraction (β).

Continuity

Conservation of mass for each phase q (where in this case phase $q = G$, L) assuming no interphase mass transfer can be written as:

$$\frac{\partial(\alpha_q \rho_q)}{\partial t} + \nabla \cdot (\alpha_q \rho_q \boldsymbol{U}) = 0 \tag{3.1}$$

The volume fraction constraint ensures that the volume fraction of all phases must sum to unity.

$$\sum_{q=1}^{N} \alpha_q = 1 \tag{3.2}$$

where in this case $N = 2$. The volume fraction constraint allows for one phasic continuity equation to be replaced by the sum of all continuity equations.

$$\sum_{q=1}^{N} \frac{1}{\rho_q} \left(\frac{\partial(\alpha_q \rho_q)}{\partial t} + \nabla \cdot (\alpha_q \rho_q \boldsymbol{U}) \right) = 0 \tag{3.3}$$

Equation (3.3) is used to calculate the volume fraction of the primary phase (liquid). The $N-1$ copies of Eq. (3.1) for the secondary phases are referred to as volume fraction transport equations as they are responsible for advecting the volume fraction through the domain. The volume fraction transport equation is commonly solved using specialized advection schemes to keep the phasic interface sharp, the details of which are given in Section 3.3. Equation (3.3) is integrated over a CV to obtain a discrete equation for pressure, analogous to the transformation of the single phase continuity equation to a pressure equation to achieve pressure-velocity coupling.

Momentum

The momentum equations of the homogeneous model are essentially single phase equations with variable fluid properties. The local fluid properties in a given CV are calculated by volume-fraction-weighted average of single phase properties for each fluid.

$$\rho = \sum_{q=1}^{N} \alpha_q \rho_q = \alpha_L \rho_L + \alpha_G \rho_G \tag{3.4}$$

$$\mu = \sum_{q=1}^{N} \alpha_q \mu_q = \alpha_L \mu_L + \alpha_G \mu_G \tag{3.5}$$

The shared momentum equation:

$$\frac{\partial(\rho \boldsymbol{U})}{\partial t} + \nabla \cdot (\rho \boldsymbol{U}\boldsymbol{U}) = -\nabla \tilde{P} + \nabla \cdot (\boldsymbol{T}) + (\rho - \rho_{\text{ref}})\, \boldsymbol{g} + \boldsymbol{S_M} \tag{3.6}$$

$\boldsymbol{T}$ is the stress tensor including viscous and turbulent stresses:

$$\boldsymbol{T} = (\mu + \mu_t)(\nabla \boldsymbol{U} + (\nabla \boldsymbol{U})^T) \tag{3.7}$$

Buoyancy is an important phenomena in most gas-liquid flows. This is especially true for the airlift pump. When buoyancy is activated, CFX uses a modified pressure ($\tilde{P}$).

$$\tilde{P} = P - \rho_{\text{ref}} \boldsymbol{g}(\boldsymbol{r} - \boldsymbol{r}_{\text{ref}}) \tag{3.8}$$

Where $\boldsymbol{r}$ is a Cartesian position vector measured from the origin, which in the present simulation is located at bottom centre of the tube. The modified pressure requires setting a reference density, and location. The reference density was set to the density of the heavier phase. The reference location is located at the top of the riser. The term $(\boldsymbol{r} - \boldsymbol{r}_{\text{ref}})$ determines the distance of point $\boldsymbol{r}$ from the reference location. Setting the reference values in such a way eliminates the hydrostatic pressure gradient in the liquid phase and reduces roundoff error [93]. The modified pressure is used in the conservation equations and boundary conditions, but the absolute pressure is required to evaluate material properties such as gas density.

$$P_{\text{abs}} = P + P_{\text{ref}} = \tilde{P} + \rho_{\text{ref}}\boldsymbol{g}(\boldsymbol{r} - \boldsymbol{r}_{\text{ref}}) + P_{\text{ref}} \tag{3.9}$$

In this work the reference pressure is set to atmospheric pressure, $P_{\text{ref}} = P_{\text{atm}} = 101.3\,[\text{kPa}]$ and the reference temperature is 298 k.

The momentum source, $\boldsymbol{S_M}$ is used to impose the surface tension force approximated by the continuum surface force (CSF) model [94]. The CSF model transforms the surface tension force (a surface force acting on the interface boundary) to a body force active in the transitional CVs located at the interface.

$$\boldsymbol{S_M} = \boldsymbol{F}_{LG} = \boldsymbol{f}_{LG}\delta_{LG} \tag{3.10}$$

The interface delta function (δ_{LG}) is zero away from the interface:

$$\delta_{LG} = |\nabla\alpha_{LG}| \tag{3.11}$$

and

$$\boldsymbol{f}_{LG} = -\sigma\kappa_{LG}\hat{\boldsymbol{n}}_{LG} + \nabla_s\,\sigma \tag{3.12}$$

The first term of Eq. (3.12) represents the normal component and the second term represents the tangential component of the surface tension force. The curvature coefficient is

$$\kappa_{LG} = \nabla\cdot\hat{\boldsymbol{n}}_{LG} \tag{3.13}$$

Where, $\hat{\boldsymbol{n}}_{LG}$ is the unit vector normal to the interface, and ∇_s is the gradient on the interface. The density of gas is calculated by the ideal gas law

$$\rho_G = \frac{MP_{\text{abs}}}{\mathcal{R}T} \tag{3.14}$$

Where M is the molecular weight of the gas phase, $\mathcal{R}$ is the universal gas constant, and T is the absolute temperature. The flow is assumed to be isothermal, so $\rho_G = f(P_{\text{abs}})$

3.2.2 Boundary and Initial Conditions

The pipe walls are represented as a standard no-slip boundary condition. No wall adhesion is specified. The outlet is a zero relative pressure opening, averaged over the cross-sectional area. This allows the two-phase flow mixture to exit the top of the riser pipe and air to flow back into the domain depending on the local pressure gradient. As stated in Section 3.1, the submergence ratio is imposed by the inlet pressure boundary condition. CFX interprets the pressure specified at boundaries in terms of the modified pressure. Based on the reference density and location describe in Section 3.2.1, the pressure boundaries are set as follows. Equation (3.16) is obtained from substituting Eq. (3.15) into Eq. (3.8) and solving for $\tilde{P}$ at the inlet location. It should be noted g in Eq. (3.15) is a scalar value of 9.81, whereas $\boldsymbol{g}$ is a vector with a component of −9.81 in the y-direction.

$$P_{\text{in}} = \rho_L g L(S_r) + \rho_G g L(1 - S_r) \tag{3.15}$$

$$\tilde{P}_{in} = -(\rho_L - \rho_G) g L(1 - S_r) \tag{3.16}$$

$$P_{\text{out}} = \tilde{P}_{out} = 0 \tag{3.17}$$

The boundary pressure specified at an opening is interpreted by CFX as the dynamic pressure if flow is entering the domain and static pressure when flow is exiting the domain. The fluid flow entering the domain through openings had a uniform velocity profile and traveled in the direction normal to the boundary surface. The turbulence intensity was set to 5% at all openings.

An initial condition must be specified for a transient simulation. The very beginning of the simulation was initialized from the situation seen in Figure 3.1. A static column of liquid filled the domain to the submerged depth and the gas filled the remainder of the riser. The velocity everywhere in the domain was set to zero and the pressure field was set to the hydrostatic gradient. Physically, this can be interpreted as the resting state of the airlift when no air is supplied. The CEL code used for the domain initialization can be found in Appendix D.1.

3.2.3 Turbulence Closure

The turbulence field is modeled with the assumption of homogeneity, analogous to the homogeneous momentum equations. Two-equation turbulence models, either the $k-\varepsilon$ or SST, were used to close the homogeneous momentum equations. No modifications are made to the single-phase turbulence equations to account for two-phase flow effects.

k-epsilon model

$$\frac{\partial(\rho k)}{\partial t} + \nabla\cdot(\rho\boldsymbol{U}k) = \nabla\cdot\left((\mu+\frac{\mu_t}{\sigma_k})\nabla k\right) + (P_k - \rho\varepsilon) \tag{3.18}$$

$$\frac{\partial(\rho\varepsilon)}{\partial t} + \nabla\cdot(\rho\boldsymbol{U}\varepsilon) = \nabla\cdot\left((\mu+\frac{\mu_t}{\sigma_\varepsilon})\nabla\varepsilon\right) + \frac{\varepsilon}{k}\left(C_{\varepsilon P}P_k - C_{\varepsilon D}\rho\varepsilon\right) \tag{3.19}$$

$$P_k = 2\mu_t\boldsymbol{\gamma}\boldsymbol{\gamma} \tag{3.20}$$

$\boldsymbol{\gamma}$ is the strain rate tensor of the mixture phase defined as:

$$\boldsymbol{\gamma} = \frac{1}{2}\left(\nabla\boldsymbol{U} + (\nabla\boldsymbol{U})^T\right) \tag{3.21}$$

The turbulence model constants given in Table 3.1 are identical to the standard single phase values. The $k-\varepsilon$ model in CFX uses a scalable wall function to approximate the boundary layer. No modifications to the wall function are made for two-phase flow.

Table 3.1: Turbulence model constants for the k-epsilon model.

	C_μ	$C_{\varepsilon P}$	$C_{\varepsilon D}$	σ_k	σ_ε
$k-\varepsilon$	0.09	1.44	1.92	1	1.3

Shear Stress Transport (SST) model

The SST model blends the $k-\omega$ model at the wall and $k-\varepsilon$ model in the free shear region.

$$\frac{\partial(\rho k)}{\partial t} + \nabla\cdot(\rho \boldsymbol{U} k) = \nabla\cdot\left((\mu+\frac{\mu_t}{\sigma_k})\nabla k\right) + (P_k - C_\mu \rho\omega k) \tag{3.22}$$

$$\frac{\partial(\rho\omega)}{\partial t} + \nabla\cdot(\rho \boldsymbol{U}\omega) = \nabla\cdot\left((\mu+\frac{\mu_t}{\sigma_\omega})\nabla \omega\right) + \left(C_{\omega P}\frac{\rho P_k}{\mu_t} - C_{\omega D}\rho\omega^2\right) + \xi_\omega(1-F_1) \tag{3.23}$$

where

$$\xi_\omega = \frac{2\rho}{\sigma_{\omega 2}}\frac{\nabla k\cdot\nabla\omega}{\omega} \tag{3.24}$$

The blending function F_1 varies between 1 for $k-\omega$ at the wall, and 0 for $k-\varepsilon$ away from the wall:

$$F_1 = \tanh\left(\left(\min\left[\max\left[\frac{\sqrt{k}}{C_\mu\omega y_{\text{wall}}}, \frac{500\mu}{\rho\omega y_{\text{wall}}^2}\right], \frac{4y_{\text{wall}}^{-2}\rho\frac{k}{\sigma_{\omega 2}}}{\max\left[\xi_\omega, \xi_{min}\right]}\right]\right)^4\right) \tag{3.25}$$

where $\xi_{min} = 1\times 10^{-10}$ and

$$\mu_t = \frac{\rho k}{\max\left[\omega, F_2\frac{\sqrt{2\gamma\gamma}}{C_{\omega P}}\right]} \tag{3.26}$$

$$F_2 = \tanh\left(\left(\max\left[\frac{2\sqrt{k}}{C_\mu\omega y_{\text{wall}}}, \frac{500\mu}{\rho\omega y_{\text{wall}}^2}\right]\right)^2\right) \tag{3.27}$$

The automatic wall function is used for the SST model. It switches between the scalable wall function, and the low Reynolds number formulation depending on the y^+. The low Reynolds number formulation accounts for the viscous sublayer. Standard turbulence model constants were used, as listed in Table 3.2. In the SST turbulence model, the constants are interpolated between the values for the $k-\varepsilon$ and $k-\omega$ models using the blending function: $\phi = F_1\phi_1 + (1-F_1)\phi_2$, where ϕ is σ_k, σ_ω, $C_{\omega P}$, and $C_{\omega D}$.

Table 3.2: Turbulence model constants for the SST model.

	C_μ	$C_{\omega P}$	$C_{\omega D}$	σ_k	σ_ω
$k-\omega$ (index 1)	0.09	$5/9$	0.075	1.176	2
$k-\varepsilon$ (index 2)	0.09	0.44	0.0828	1	1.168

3.3 Numerical Methods

The governing equations presented above in Section 3.2 form $N+6$ many equations, $N+5$ of which are partial differential equations (PDEs). For the present case of $N=2$ phases, seven PDEs are solved at every time step. CFX uses an element-based finite volume approach. Standard finite element gradient approximations are used for diffusion terms and the high resolution scheme was used for advection terms for the momentum equations. A first order upwind scheme is used for the turbulence equations. By activating the free surface model in CFX, the compressive differencing scheme is used for the volume fraction transport equations (Eq. (3.1)). The compressive scheme adds anti-diffusion terms to the upwind advection scheme. The anti-diffusion terms are a numerical strategy to keep the phasic interface sharp, and no interface reconstruction is used. The free surface model VOF implementation in CFX is fully implicit and the interface sharpness does not depend on time step size [95]. The linearized equations are solved iteratively using a solver that couples the mass, momentum, and volume fraction equations. Additive correction multigrid is used to accelerate convergence.

A time-dependent solution is required for numerical stability and physically meaningful results. The phasic interface being tracked with the VOF approach is constantly deforming and moving throughout the domain, so a transient simulation is necessary. The strongly nonlinear physics require a relatively small time step and large number of iterations per time step. Details of the time step size, solver expert parameters, and convergence criteria used in the present work are covered in Section 4.3

3.4 Procedure for Simulating Performance Curve

Starting from the initial condition described in Section 3.2.2, the inlet air flow rate was progressively increased to advance along points in the airlift pump performance curve. In practice, many separate transient simulations are needed to collect the necessary data. Each simulation period is initialized from the previous one at the same operating point; essentially joining the transient simulations. To move between operating points on the performance curve, the gas flow rate is increased gradually in a linear ramp function rather than a step change. This prevents disturbances to the flow that can lead to numerical convergence problems or physical perturbations to the system that may take a long period of time to subside. The ramping up method can be understood physically as gradually opening the gas supply valve to adjust the flow rate.

The simulation results for a performance curve were not necessarily collected in a sequential manner. The simulation of one pseudo-steady operating point does not have to be completed before moving on to ramp up to another operating point. Once the first operating point was reached two simulations could be run simultaneously; one of the pseudo-steady operation and the other ramping up to the next operating point. The pseudo-steady operation of the airlift does not depend on the transient path to reach the operating point. Therefore, neither the rate of the ramping function nor the initial conditions influence the final answer. The flow during the transient periods of airlift operation was not examined in this work.

Chapter 4

Model Verification

This chapter presents the specific details of the CFD model geometry and the experimental data used for comparison, as well as the steps taken assess the reliability of the simulation results. Sensitivity studies were performed to examine the effects of: a reduced computational domain, mesh density, and turbulence model. The convergence of the CFD simulation and the liquid discharge rate were evaluated.

4.1 Geometry Specification

Many experimental studies of the airlift pump were listed in Section 2.1, one such study is used as the basis of the CFD model setup and for comparison of results in the present work. The experimental study was selected based on: range and number of airlift parameters varied, thorough documentation of the experimental apparatus, prevalence within the literature. Furthermore, preference was given to smaller airlifts because of the lesser computing time. Based on the aforementioned criteria, the work of Kassab *et al.* [25] was selected. Several different riser lengths and submergence ratios are used in this work, as described in Section 4.1.3

Because the CFD model is based on the experiments of Kassab *et al.* [25] it is appropriate to also compare the CFD model against the steady-state algebraic model proposed by Kassab *et al.* [25]. Details of the model implementation and verification are provided in Section 4.7.

4.1.1 Description and Modeling of Kassab *et al.* Geometry

The experiment used a U-tube style airlift apparatus with a feed tank that was moved up and down to adjust the submergence ratio. Because there is insufficient details on the construction of the liquid supply line and the fittings connecting the bottom of the entrance pipe to the supply tank, the losses are neglected when specifying the P_{in} boundary condition.

Further simplifications were necessary in modeling the air jacket. In the experiments, air was supplied from an air compressor to an airjacket, then ultimately introduced to the liquid through 56 circular injection ports 3 mm in diameter. The injection ports were distributed as seen in Figure 4.1, with 8 evenly spaced columns and 7 rows. For ease of meshing, the circular injection ports were approximated as squares of equal area. The centre-to-centre spacing (L_1) of the injection ports is 10 mm [96]. The length of the suction pipe (L_{suc}) is 20 cm.

The mass flow rate of gas is likely to vary between injection ports due to the internal structure and pressure distribution within the airjacket device. Furthermore, the compressibility of the gas in the supply line between the compressor and airjacket could cause the flow to to fluctuate with time. In the absence of such details, the specified constant mass flow rate was uniformly distributed over all the injection ports.

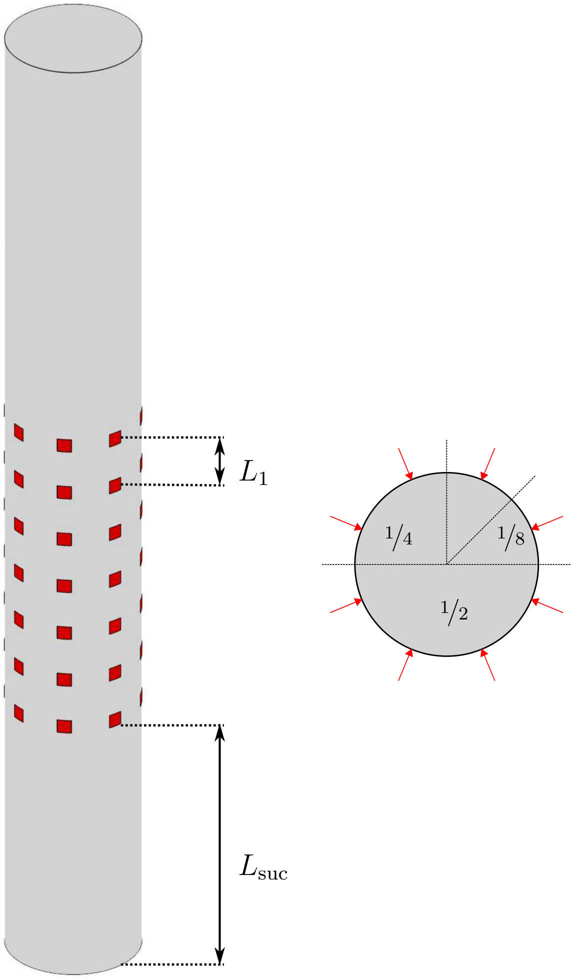

(a) **(b)**

Figure 4.1: CFD model representation of the location of air injection areas used to simulate Kassab *et al.* [25] experiments. (a) isometric view, riser pipe not to scale. (b) Top view. Air injector locations indicated by arrows and geometric symmetry planes indicated by dashed lines.

Careful examination of the geometry presented in Figure 4.1 suggest the computational domain may be reduced through the use of symmetry. The geometry consists of repeated 45-degree segments. Although symmetry is valid geometrically, there is no guarantee the hydrodynamics are symmetric and the literature discussed in Section 2.2 suggests a full geometry is required. This is explored in the following, Section 4.2.

4.1.2 Specification of Boundary Conditions

A test case was run for 1 s using configuration C1 and $\dot{m}_G = 0$ kg h^{-1}. The height of the static column remained constant, confirming the boundary conditions and initialization were behaving as expected.

4.1.3 Simulated Cases

Due to the computational demands of the simulation, it was not feasible to simulate every experimental configuration performed by Kassab *et al.* [25]. Instead, three configurations of different riser length and submergence ratio were selected for comparison. The specific geometric parameters of these configurations are summarized in Table 4.1. For each configuration, multiple gas flow rates (operating points) were simulated. Gas flow rates ranging from 2 to 10 kg h^{-1} in 2 kg h^{-1} increments were considered. For convenience the following shorthand will be used to indicate a particular operating point. For example, C1m2 refers to C1 $\dot{m}_G = 2$ kg h^{-1}, or specifically $L = 1.75$ m $S_r = 0.5$ $\dot{m}_G = 2$ kg h^{-1}.

Table 4.1: Experimental conditions simulated.

Configuration	L [m]	D [mm]	S_r
C1	1.75	0.0254	0.5
C2	2.75	0.0254	0.74
C3	2.75	0.0254	0.5

Simulation of the different tube lengths required the use of a different mesh, the details of which are covered in Section 4.4. The $k-\varepsilon$ turbulence model is used for the majority of the present work. The SST turbulence model is used for a select case of the C1 configuration for comparison against the $k-\varepsilon$ results. It will be demonstrated in Section 4.8 that there is not a significant difference in airlift performance between the two turbulence models, thus it is justifiable to use the $k - \varepsilon$ model for all simulations.

4.2 Symmetry

Preliminary tests were performed to access the validity of a reduced computational domain using the C1m4 operating point as a representative case. The divisions used to form the reduced computational domains are located halfway between injection ports, as shown in Figure 4.1 with dashed lines. Zero gradient boundary conditions were applied to the symmetry planes. A similar grid structure to the full tube (see Section 4.4), was used for the 1/4 and 1/2 tube domains. The mesh cross-section was essentially cut at the symmetry boundaries. The reduced computational domains had a similar mesh density to the working mesh selected in Section 4.4, but no formal mesh independence study was performed. It was not possible to form the mesh for the 1/8 segment in the same way, instead a Y-grid style blocking was used. Numerical difficulties due to high mesh skewness at the tip of the wedge were encountered with the 1/8 domain. Consequently, a converged solution for liquid discharge rate was not obtained for the 1/8 segment. No attempt was made to improve the mesh, and in turn simulation stability for the 1/8 segment. It was deemed unnecessary based on the results of the 1/4 and 1/2 tube domains, as discussed below.

4.2.1 Comparison of Time-Averaged Results

Table 4.2 summarizes the liquid discharge rate predicted by the three computational domains. The liquid discharge rate is clearly sensitive to the use of symmetry. Therefore, the full tube domain must be used. It is coincidental that the 1/4 tube predicts a discharge rate similar to the full tube. Closer examination of the two-phase flow structures in the reduced domains will demonstrate the 1/4 is not a viable approximation of the flow physics. The root mean square

(RMS) of the eduction flow rate time signal ($\dot{m}_{L,\mathrm{out}}^{\mathrm{rms}}$) is a convenient tool for comparing the dynamic nature of the simulations. Despite the average discharge rates being similar between the $1/4$ and full tube, the RMS is very different. The RMS of the $1/2$ tube is very similar to the full tube. These trends in integral parameters are consistent with the observations of local flow structures discussed below.

Table 4.2: Effects of domain size for for the case of C1m4.

	$1/4$	$1/2$	full
$\overline{\dot{m}}_L$ [kg h^{-1}]	744	554	716
$\dot{m}_{L,\mathrm{out}}^{\mathrm{rms}}$ [kg h^{-1}]	677	397	428

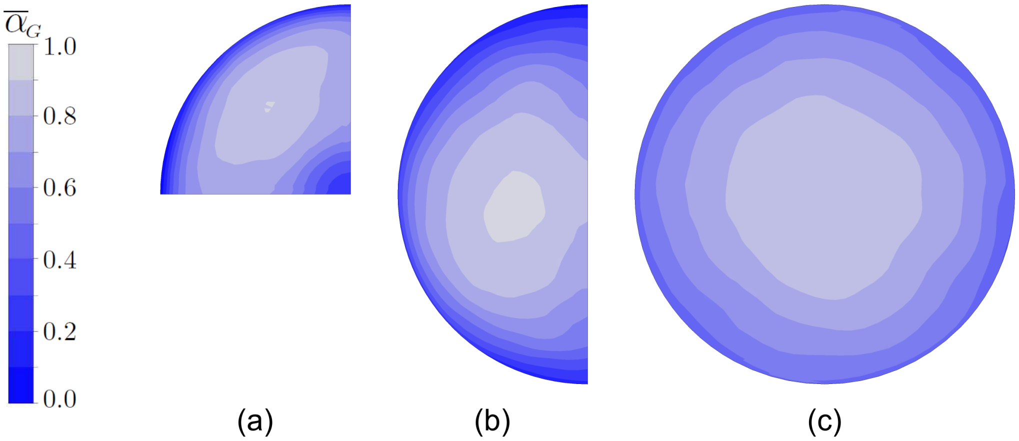

Figure 4.2: Contour of time-averaged void fraction at $y = 1.5$ m cross-section: (a) quarter, (b) half, (c) full.

Figure 4.2 demonstrates how the time-averaged results of the quarter and half domains are not consistent with the solution obtained with the full geometry. Specifically, if the $1/4$ or $1/2$ tube results were mirrored about the symmetry plane(s), the resulting void distribution is physically unreasonable and does not match the full domain.

4.2.2 Comparison of Instantaneous Results

The presence of liquid at the centre point of the quarter pipe in the time-averaged contour (Figure 4.2) is indicative of liquid being trapped in the centre of a gas ring, as discussed in Section 2.2. This is confirmed in Figure 4.3, which shows instantaneous contours from the side view. In Figure 4.3, the $^1/_4$ and $^1/_2$ tube solution have been mirrored to show a hypothetical full tube. The pockets of liquid in the centre are not predicted by the full tube simulation, nor are they physically reasonable.

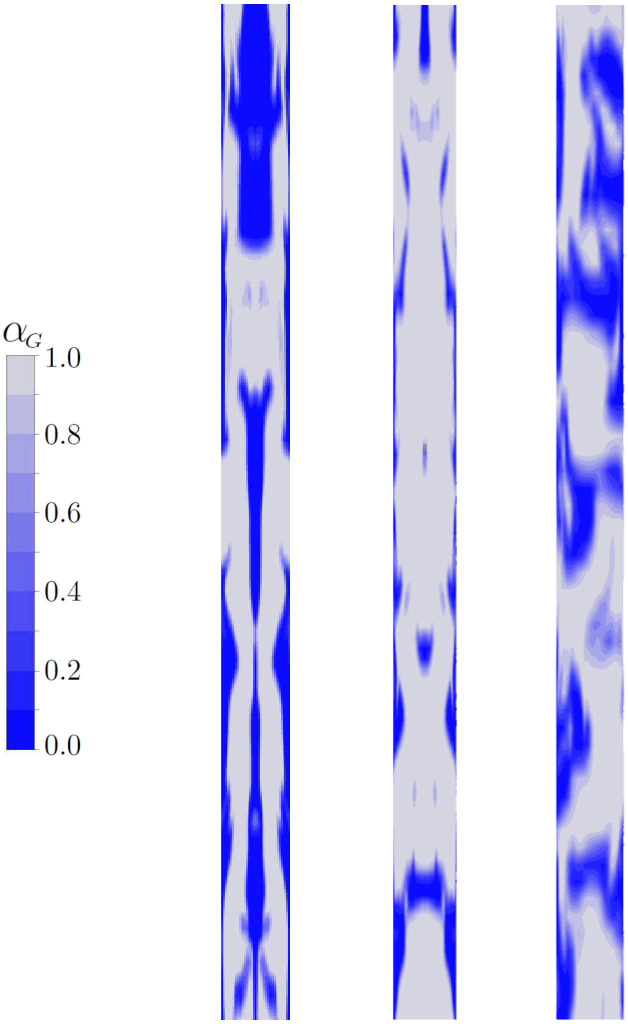

(a) **(b)** **(c)**

Figure 4.3: Sample phasic distribution in the airlift riser pipe for: (a) quarter, (b) half, and (c) full tube domains.

Comparing the time-averaged and instantaneous phase distribution of the full tube in Figures 4.2(c) and 4.3(c), respectively; the time average distribution is practically axisymmetric but the instantaneous distribution is not. Because the instantaneous contour shows a single snapshot in time the transient nature of the flow is not immediately clear. Similar contours at the same location at different instances in time will show gas pockets in different locations within the tube. Summing a large number of these instantaneous contours (time averaging) shows that, in general, the gas tends to occupy the centre of the tube and liquid at the walls. The axisymmetric nature of the time-averaged void fraction suggests there is no preferred path of motion for the large gas pockets. All three of the flow regimes expected in the airlift pump, namely slug, churn and annular flow, qualitatively have similar distribution of $\overline{\alpha}_G$, but distinctly different contours of α_G.

The contour plots demonstrate that the phase distribution is not symmetric, but they do not describe the motion of the flow. Streaklines were used to study the non-axisymmetric motion of the instantaneous flow. A streakline is a visual representation of the path of a massless particle which originated from a prescribed location and is carried by the flow. In Figure 4.4 two seeding locations are used: one per opposing injection port in the middle row. The resulting streaklines highlight the irregular motion of the flow. The paths have a chaotic corkscrewing motion with a reasonable likelihood of occupying any sector of the pipe. Figure 4.4 represents a single snapshot in time. At another instant in time, the path will be completely different. Clearly a symmetry plane boundary condition would unrealistically constrain the motion of the flow; nor is a periodic boundary condition appropriate because one angular sector of the flow is not correlated to the opposing sector.

Figure 4.4: Streaklines of velocity from air injection ports.

Time series of pressure at individual injection ports were also investigated to explore evidence of the non-axisymmetric flow behaviour. The middle ring of injection ports was arbitrarily label P1 – P8 sequentially around the circumference. A uniform and constant mass flow rate is specified over all injection ports but the pressure, and in turn the gas velocity, is not constrained by the boundary condition. The fluctuation in pressure at an injection port was calculated relative to the average injection pressure at that ring as follows:

$$P'_{Pi} = P_{Pi} - \frac{1}{8}\sum_{n=1}^{8} P_{Pn} \tag{4.1}$$

The RMS of the pressure fluctuations were calculated for all points P1 – P8, giving $\approx 285\,\mathrm{Pa}$ for all injection ports. This definition of pressure fluctuation indicates that all injection ports fluctuate by the same amount and there is no preferred orientation to the flow but does not show the relationship between the injection ports. An alternative method is to calculate the fluctuating pressure at injection ports P2 – P8 relative to P1.

$$P'_{Pi} = P_{Pi} - P_{P1} \tag{4.2}$$

It was found that there is an inverse relationship between pressure fluctuations at adjacent injection ports. The pressure oscillates in a fairly regular manner about a central value with evenly numbered injection ports a half period out of phase from the odd numbered injection ports. Two points, P2 and P3, are used as an example in Figure 4.5. P'_{P3} is much smaller in magnitude because at any instance P_{P3} is close in value to P_{P1}. It is expected that if the flow was axisymmetric, the difference in pressure between injection ports located in a ring would be small and random. The clear pattern in angular direction supports the conclusion that axisymmetry is not applicable in this case.

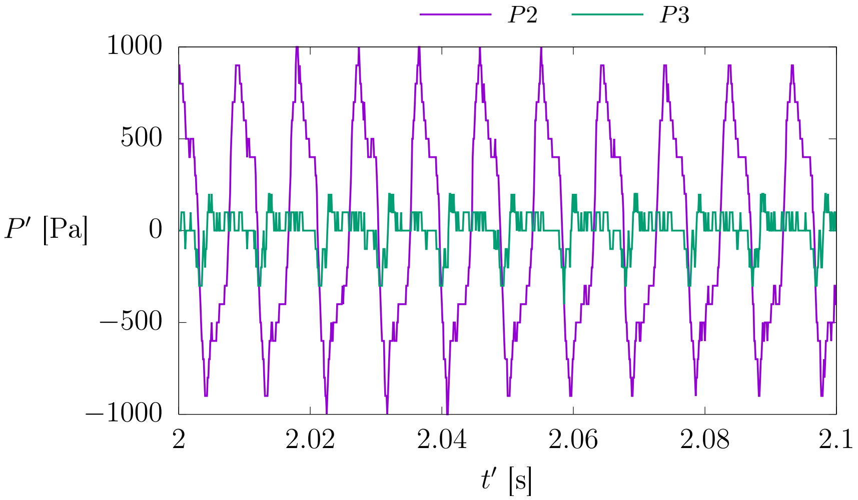

Figure 4.5: Representative sample of relative fluctuations in injector ports.

Table 4.3 shows the RMS of the P' time signals plotted in Figure 4.5. The high degree of correspondence within points P2, P4, P6, P8, and points P3, P5, P7, confirms that the behaviour shown in Figure 4.5 is representative of all points.

Table 4.3: RMS of injection port pressure fluctuations relative to P1.

Point:	P1	P2	P3	P4	P5	P6	P7	P8
P_{Pi}^{rms} [Pa]	0	559	114	557	155	558	106	561

The existence of this behaviour was verified for other flow rates and submergence ratios. There was no distinguishable pattern to the fluctuations between rows of injection ports. The magnitude of the pressure fluctuations was generally the largest at the centre row. The relationship between pressure monitor points was also examined using the two-point correlation. The normalized correlation coefficient was approximately 0.95 for injection ports an even number apart and -0.95 for injection ports an odd number apart. the magnitude of the correlation coefficient decreased between points located in different rows. The interpretation of the two-point correlation is consistent with alternating bursts around the circumferential ring of injection ports.

In summary, it has been clearly demonstrated that the full geometry must be used in order to predict physically reasonable two-phase flow structures. Furthermore, the use of a reduced computational domains with symmetry planes impacts the liquid discharge rate predicted by the simulation.

4.3 Numerical Convergence

No formal sensitivity studies were performed for convergence criteria or time step. The long computing times and transient nature of the problem make such studies infeasible. Instead, reasonable values were selected based on experience solving two-phase flow problems, and monitoring residuals and balances during preliminary trials.

4.3.1 Optimum Time Step

The time step size has a considerable influence on the rate the transient simulation progresses through simulated time. A certain number of iterations (dependent on the time step size) are required at every time step to reach the convergence target before progressing to the next time step. The computing time for each iteration is dependent on the number of nodes and computing resources. The optimum simulation rate is achieved when the number of total iterations is at a minimum. A larger time step requires fewer time steps to reach the desired elapsed time but the number of iterations per time step increases. Conversely, a smaller time step leads to fewer iterations per time step but more total time steps. There is no formula for the optimum time step size, although a rule of thumb is 3 to 5 iterations per time step for standard flows with CFX [93]. Due to the highly nonlinear physics of two-phase flow, 10 to 15 iterations per time step was found to give a superior simulation rate. This corresponded to a fixed time step size of 1×10^{-4} s. In some instances at higher gas flow rates ($8 \mathrm{kg\,h^{-1}}$) a smaller time step size of 5×10^{-5} s was required for numerical stability.

The impact of the time step size on the accuracy of the solution must also be considered. If too large of a time step is used, the simulation will not properly resolve the dynamic nature of the problem because of temporal discretization errors. No formal sensitivity analysis was performed for time step size because the optimum time step of 1×10^{-4} s is and within the range commonly used in literature for comparable simulations, as mentioned in Appendix A.2.1. In a limited comparison of the preliminary trials obtained with time steps of $5{\times}10^{-5}$ s and $1{\times}10^{-5}$ s, no difference in the dynamic characteristics of the solution was observed. The maximum Courant number was generally below 8 and the RMS average Courant number was approximately 0.4.

4.3.2 Convergence Criteria

In general, numerical convergence is more difficult to achieve with simulations of multiphase flows than single phase simulations. Strict equation maximum residual criterion often cannot be met; instead global conservation is more often used as a primary indicator of convergence. In the present work, a criterion of 1×10^{-5} was used for the RMS of equation residuals, and 1% imbalance was used for the global conservation criterion.

The CSF model implements the surface tension force in a nonconservative manner which can lead to greater difficulty achieving satisfactory mass conservation. The same conservation target was used for all solution fields, but special attention was paid to the water mass imbalance as it was typically the largest. The imbalances of the other solution fields were approximately an order of magnitude smaller than the water mass imbalance.

It was not possible to satisfy the convergence criteria at every time step; however, a convergence failure once every thousand time steps should not have an appreciable effect on the overall result. Figure 4.6 shows the typical convergence behaviour of a run. The solution residuals fluctuate around an acceptable threshold with sporadic spikes. The domain imbalances also spike sporadically with the equation residuals. The domain imbalance of water mass was observed to be as high as 20% at some time steps, but the average over the course of the simulation was below 0.5%.

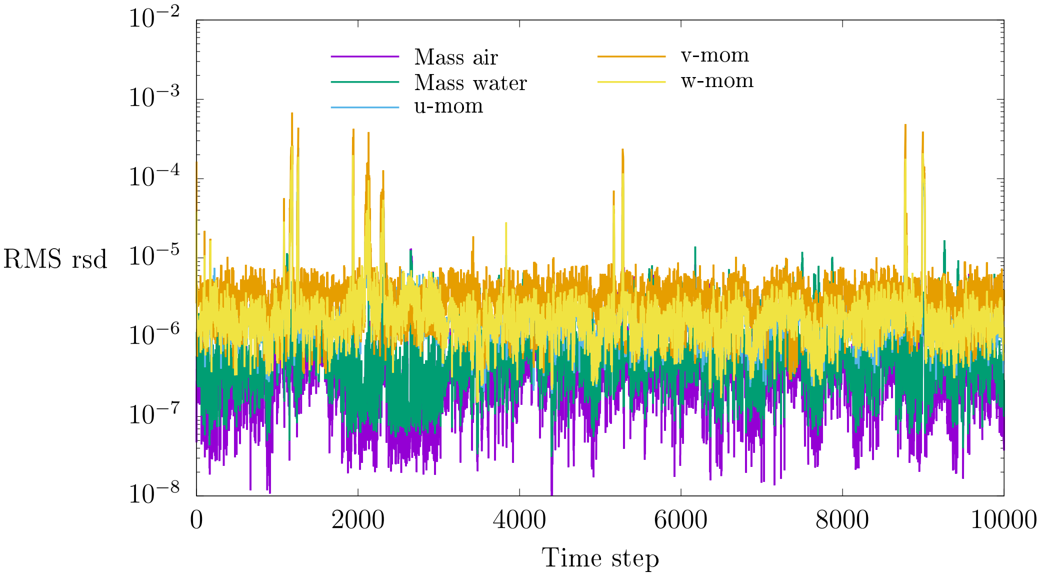

Figure 4.6: Typical convergence behaviour of solution residuals.

4.3.3 Partitioning Considerations

The addition of the CSF model made the solution stability sensitive to partitioning. The linear solver is prone to failure when the motion of free surface aligns with partition boundaries [93]. To combat this, the partitioning direction was specified along the axial direction of the domain (y-axis), and the solver overlap relaxation factor was reduced to 0.8. The separate mesh regions were defined as sub-domains in CFX to facilitate solution monitors. Coupled partitioning was used so the sub-domains were all partitioned together as if it were one continuous domain, which improves numerical stability.

4.4 Mesh Sensitivity

The meshing requirements are often different for multiphase flows than single-phase flows. How the interfacial interactions are modeled greatly impacts meshing considerations. With the homogeneous VOF multiphase model, the bulk flow rate is not the primary factor impacting mesh independence; rather, the regime is paramount. If the flow in an airlift pump behaves in slug or churn flow, the same mesh density should be appropriate regardless of the change in flow rate.

4.4.1 Mesh Generation

A structured hexahedral mesh with an O-Grid face mesh swept along the axial length of the domain was used. An O-Grid style mesh is best option for interface tracking of slug flow [89]. The face mesh, as seen in Figure 4.7(a), had inflation layers to refine the mesh near the wall. The distance of the first node from the wall (Δ_{x1}) is an important parameter for turbulence modeling, and accurately resolving the phasic distribution near the wall. A small Δ_{x1} is desirable for both aforementioned considerations; however, a small Δ_{x1} presents aspect ratio challenges in a long tube such as the airlift riser.

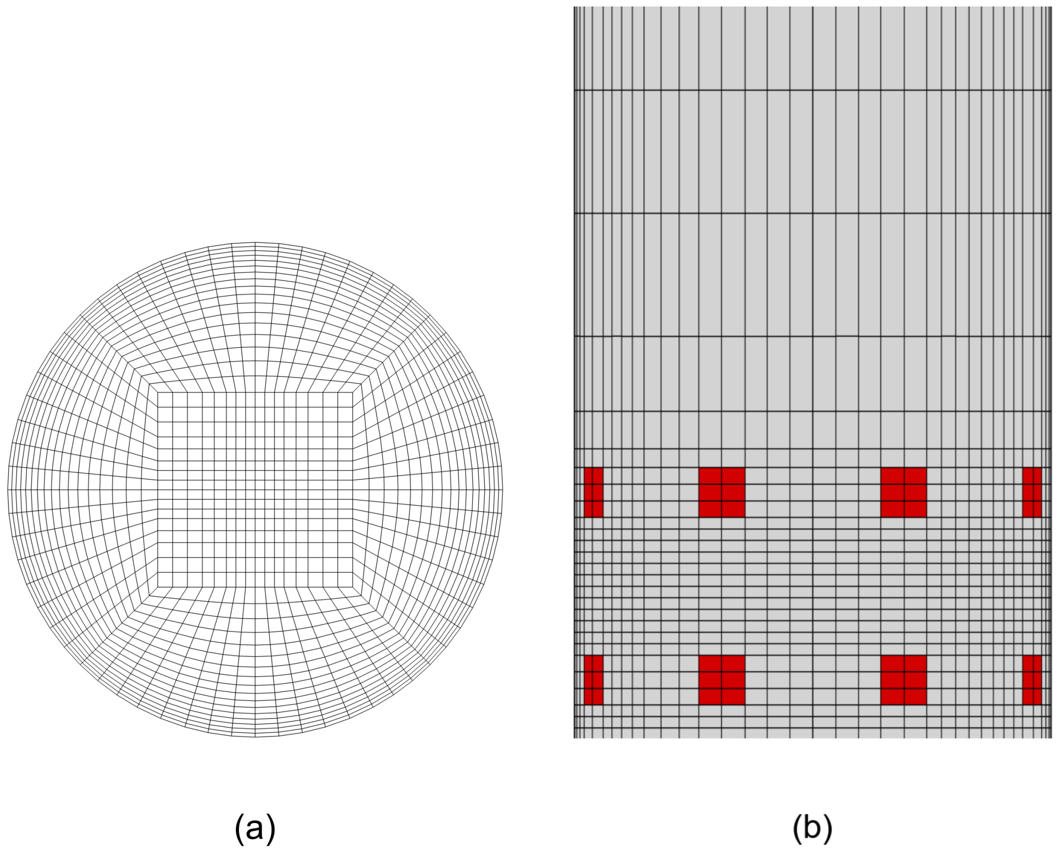

Figure 4.7: Sample mesh: (a) O-Grid cross-section, (b) air injector and riser axial expansion.

The meshing of the computational domain was broken into three components, as indicated in Figure 4.8. The injector region was further broken into two sub-pieces: a disk containing one ring of injection ports and a disk for the space in between injection ports. The aforementions sub-pieces were copied to assemble the complete air injector region.

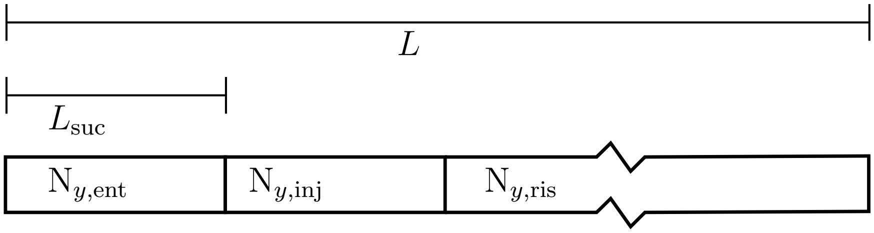

Figure 4.8: Diagram of mesh regions and subdomains. Not to scale.

A minimum of three nodes were distributed across each air inlet face in both the angular and axial direction. The axial distribution of nodes varied considerably along the length of the domain. A minimal mesh was used for the entrance pipe because it is a region of predominantly single-phase flow. For all meshes considered, $N_{y,\text{ent}} = 23$. The axial spacing was refined where the entrance pipe joined the air injector. The requirement of three nodes across each air inlet face dictated the spacing in the entire injector region. The spacing disks between injection ports had a similar axial spacing to that of the injection port disk. The axial spacing of the first interior node of the riser pipe matched the axial spacing of the injection ports. The axial spacing of the riser pipe mesh was expanded along the length of the riser. The maximum axial length ($\Delta_{y,\text{max}}$) was limited by aspect ratio considerations and need to resolve interfacial structures. When the longer riser pipe was used for cases C2 and C3, $N_{y,\text{ris}}$ was increased to maintain a similar axial spacing to that of the shorter riser. Table 4.4 summarizes the important nodal distributions of the meshes presented in the mesh sensitivity study.

Table 4.4: Details of mesh densities tested.

	N_{total}	N_{xz}	$N_{y,\text{inj}}$	$N_{y,\text{ris}}$	Δ_{x1} [mm]	$\Delta_{y,\text{max}}$ [mm]
M1-L175	446 k	1 344	88	201	0.2	7.52
M2-L175	739 k	1 908	94	230	0.1	6.56
M3-L175	1 226 k	3 360	94	230	0.1	6.56
SST-L175	3 143 k	2 480	95	1 118	0.04	1.62
M1-L275	461 k	1 908	94	103	0.1	26.4
M2-L275	1 120 k	1 908	94	441	0.1	5.43

4.4.2 Evaluation of Mesh Independence

Case C1m4 was used for the initial study of mesh sensitivity. The average y^+ of the M1 – M3 meshes was roughly 50, well within the acceptable range for the $k-\varepsilon$ turbulence model used. A goal of $y^+ < 5$ was set for the runs using the SST turbulence model. Because y^+ is proportional to the local velocity, a higher gas flow rate (C1m8) was used to select a mesh for the SST model. The target y^+ was achieved for $\langle y^+ \rangle_\mathrm{A}$, but the maximum local value commonly ranged from 10 – 40 due to oscillations in the local flow, as seen in Figure 4.9. The wall-area average was only calculated over the two-phase regions of the domain. Including the entrance pipe in the average would misleadingly lower the value of $\langle y^+ \rangle_\mathrm{A}$. Although the size of control volumes in the axial direction does not effect the y^+ itself, $\mathrm{N}_{y,\mathrm{ris}}$ had to be increased considerably to maintain a satisfactory aspect ratio (less than 50) in the streamwise direction. The y^+ was slightly higher in the $8\mathrm{kg\,h^{-1}}$ ($\langle y^+ \rangle_\mathrm{A} \approx 4$) case than $2\mathrm{kg\,h^{-1}}$ ($\langle y^+ \rangle_\mathrm{A} \approx 2.3$). The increase in y^+ is an affect of the increase in bulk flow rate. A detailed comparison of the $k - \varepsilon$ and SST results is provided in Section 4.8.

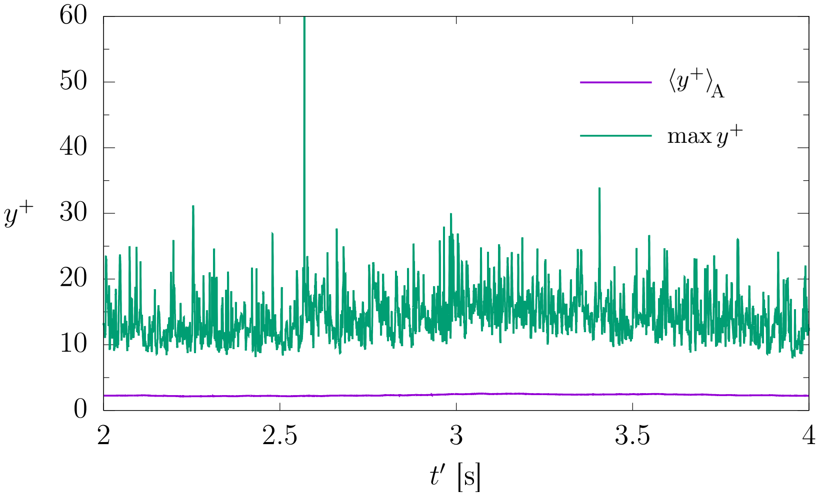

Figure 4.9: Sample of y^+ monitors for C1m2 SST simulation.

Due to the chaotic nature of the flow, it is difficult to compare local or instantaneous values to assess the mesh independence. Averaged values that are independent of the time period they are calculated over must be used for fair quantitative comparison between meshes. Table 4.5 summarizes the relevant quantities for the three sets of mesh independence studies. Comparison of instantaneous void fraction contours qualitatively show finer meshes produce a sharper phasic interface, but this provides no clear justification for selecting a working mesh.

Table 4.5: Time average quantities for mesh independence tests.

		$\overline{\dot{m}}_L$ [kg h^{-1}]	$\dot{m}_{L,\mathrm{in}}^{\mathrm{rms}}$[kg h^{-1}]	$\dot{m}_{L,\mathrm{out}}^{\mathrm{rms}}$[kg h^{-1}]	$\langle\overline{\alpha}_G\rangle_V$	$\max\overline{v}$
C1m4	M1-L175	555	184	424	0.660	8.81
	M2-L175	716	168	428	0.682	6.71
	M3-L175	670	175	399	0.671	6.75
C1m8	M2-L175	890	136	511	0.803	8.01
	M3-L175	897	128	480	0.793	8.01
C2m4	M1-L275	1960	199	899	0.461	21.2
	M2-L275	2013	196	945	0.449	23.9

Regarding the case of C1 $\dot{m}_G = 2$ kg h^{-1}, there is a significant change in liquid discharge with the first refinement (between M1 and M2). With the second refinement, there is an approximately 6% change in liquid discharge rate. The change in liquid discharge rate is on par with the statistical sampling error (described in Section 4.6) in calculating the liquid discharge rate. Additionally, the change of other quantities is smaller with the second refinement than the first. Therefore the mesh M2 was preliminarily selected as the working mesh. Meshes M2 and M3 were tested again at the higher gas flow rate of 8 kg h^{-1}. Again the change between average quantities was negligible, as seen in Table 4.5. Based on the results at 4 and 8 kg h^{-1} gas flow rates for case C1, mesh M2 was selected as the working mesh.

Although the liquid discharge rate predicted my M1-L275 and M2-L275 is similar, the difference in axial nodal distribution has a significant effect on the interfacial structures and numerical stability of the simulation, as discussed in the following section. For these reasons, mesh M2-L275 is used for the simulations of configurations C2 and C3. Mesh M2-L275 is an extrapolation of the shorter riser mesh M2-L175.

Importance of Axial Nodal Distribution

The coarseness of the mesh M1-L275 in streamwise direction produced physically unrealistic interfacial structures, as demonstrated by the void distribution in Figure 4.10(a). The axial length of the control volumes smeared the void fraction, preventing the gas from separating into discrete pockets, as seen in Figure 4.10 (b). Because the gas could not form into large highly deformed bubbles, it remained near the tube wall for a much greater distance with mesh M1-L275. Not only is the gas's motion unrealistic, the wall shear stress in the riser is affected by which phase is in contact with the wall.

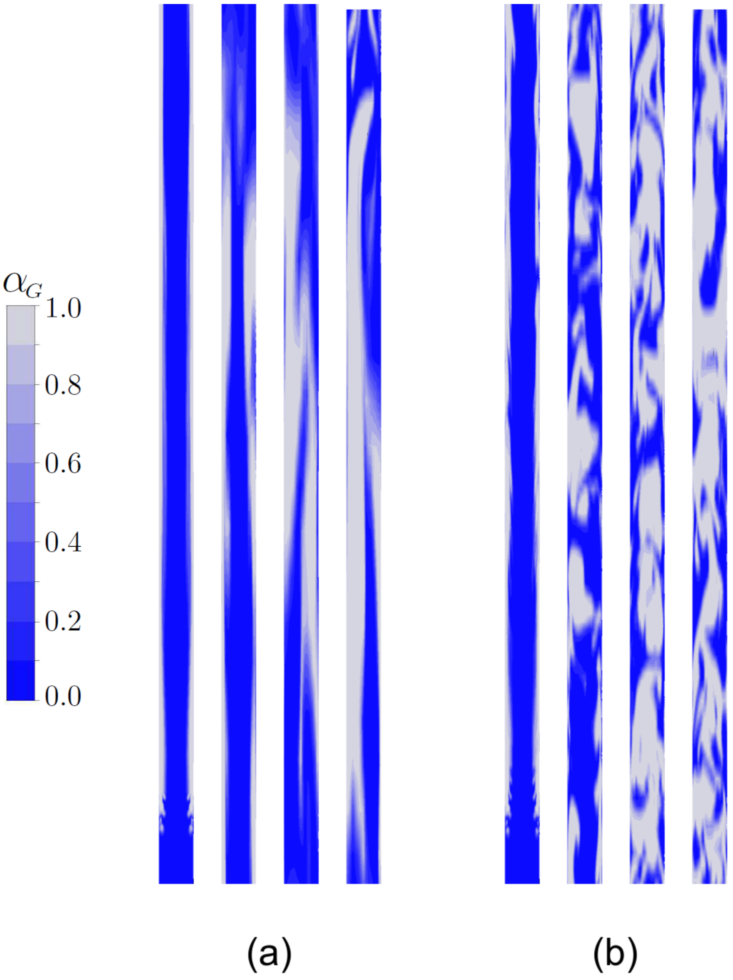

Figure 4.10: Contour of void fraction with riser broken into 4 pieces: (a) M1-L275, and (b) M2-L275.

The large axial length of CVs in mesh M1-L275 was also detrimental to the numerical stability of the solution. The aspect ratio of CVs near the wall was very large, (greater than

200). The poor aspect ratio slowed convergence and in some instances cause the solver to crash. Because the interfacial structures were unrealistic due to by the large axial length of the CVs, the surface tension body force was affected and may have contributed to convergence issues as well.

4.5 Run Times

It is difficult to quote a single representative number for the simulation run times because every case was different. The transient simulation was not run for a predetermined span of time; rather, the total simulated time required for the liquid flow rates to converge depended on the airlift pump configuration and the transient operation leading to the pseudo-steady state, as discussed in Section 4.6.2. Furthermore, the computing time depends on the particular machine used and queuing time for HPC clusters. Considerable computing time was also required to traverse through the startup and transient periods not considered in the pseudo-steady operation.

The majority of simulations were run on Compute Canada HPC clusters. The simulation of each operating point consisted of multiple runs of 5 days' time. The number of cores per compute node and speed of the cores varies between clusters. The SST model required 219 hours per second of simulated time when using 96 cores at 2.4 GHz. With the same set up the L175-M2 model required 132 hours per second of simulated time. To give context to these numbers, a simulated period of approximately 5 s is needed to determine the liquid discharge rate as discussed in Section 4.6.2, meaning the SST simulation requires approximately 46 days of computing time for a single operating point. The C1 configuration, which has the lowest number of nodes, still required roughly 28 days.

Using the C2m6 operating point as an example, the simulation of 4.6 s of pseudo-steady operation required 27 days including queue time. The simulation of the transient airlift operation as the gas flow rate was ramped from 4 $\mathrm{kg\,h^{-1}}$ to 6 $\mathrm{kg\,h^{-1}}$ required an additional 18 days. Therefore, the total time for the C2m6 operating point simulation was 45 days.

4.6 Convergence of Statistics

Due to the unsteady nature of the two-phase flow in the airlift, time averaging of relevant quantities is required for characterizing airlift pump performance and comparing between different airlift pump configurations. For a very large sample size, the time average is equivalent to the ensemble average. When the average value becomes independent of further increase of sample size, the statistic is said to be converged. Once the statistic is converged, the statistical measure of the finite sample accurately represents the true value of the population (an infinitely large sample). The minimum sample size required for convergence depends on the nature of the signal itself and the desired convergence tolerance. Because of the proportional increase in computing time required for an increased sample size, a compromise must be made between accuracy of average values and computational effort. The specific methodology for determining the liquid discharge rate is provided in Section 4.6.2.

4.6.1 First Order Statistics of Time Signals

In this section, the symbol ϕ represents a generic time-dependent continuous variable. The notation presented in this section is used when presenting the procedure for determining the liquid discharge rate.

Accumulating Average

The accumulating average shows how the average value is changing with increasing sample size. For a finite sample of $n = 1...N$ many values

$$\overline{\phi}^{n} = (\frac{1}{n})\phi^{n} + (\frac{n-1}{n})\overline{\phi}^{n-1} \tag{4.3}$$

$\overline{\phi}^{N}$ is equivalent to the arithmetic mean of the complete sample. The accumulating average can be plotted as a function of n as a visual means of determining when the statistic is converged.

RMS of a Time Signal

The root mean square (RMS) of a time signal is a useful means of characterizing the fluctuations of a signal with a single value. It is a measure of how far, on average, the instantaneous value of ϕ is from its mean value ($\overline{\phi}$).

$$\phi^{\text{rms}} = \sqrt{\frac{1}{N}\sum_{n=1}^{N}(\phi^{n} - \overline{\phi})^{2}} \tag{4.4}$$

Statistical Sampling Error

The statistical sampling error quantifies the uncertainty in an average value calculated using a finite sample.

$$\epsilon = \sqrt{\frac{(\phi^{\text{rms}})^{2}}{N_{eff}(\overline{\phi})^{2}}} \tag{4.5}$$

Where N_{eff} is the number of statistically independent samples. Because of the small simulation time step size, the sampling frequency of the monitor point data was less than two times the integral time scale ($\Delta t < 2T_{\text{int}}$). Therefore one sample is not statistically independent of the adjacent sample. The integral time scale, T_{int} was estimated from the time shift required for the autocorrelation of the signal to approach zero (< 0.0001). The autocorrelation was computed using the Matlab `xcorr` function. The effective number of independent samples was estimated as follows:

$$N_{\text{eff}} \approx \frac{N\Delta t}{2T_{\text{int}}} \tag{4.6}$$

Thus

$$\epsilon \approx \sqrt{\frac{2T_{\text{int}}}{N\Delta t}\frac{\left(\phi^{\text{rms}}\right)^2}{\left(\overline{\phi}\right)^2}} \tag{4.7}$$

As previously stated, the statistical sampling error depends on the characteristics of the signal itself. This is clearly demonstrated in Eq. (4.7) by the dependence on the RMS of the signal, and the decorrelation time used to approximate the integral time scale. For example, the statistical sampling error was greater for the liquid mass flow rate monitored at the outlet than at the inlet for a given simulation.

4.6.2 Liquid Discharge Rate

Both the statistical convergence and the physics of the airlift pump must be considered when determining the liquid discharge rate. The instantaneous liquid flow rates were monitored at entrance ($\dot{m}_{L,in}$) and outlet ($\dot{m}_{L,out}$). Not only must each signal converge separately, but the total liquid entering the domain must be equal to the total liquid leaving the domain due to continuity. The unsteady nature of the flow means $\dot{m}_{L,in} \neq \dot{m}_{L,out}$, however if the airlift is operating at a pseudo-steady-state $\overline{\dot{m}}_{L,\text{in}} = \overline{\dot{m}}_{L,\text{out}}$ meaning there is no net storage of mass. The same arguments can be made for the convergence of the gas flow rate, however it was found the gas flow rate converged before the liquid flow rate. Consequently, the convergence of gas flow rates did not serve as a stopping criteria for the simulation.

The accumulating average was calculated for $\dot{m}_{L,in}$ and $\dot{m}_{L,out}$. The liquid discharge rate was said to be converged when the following two criteria were satisfied:

1. The flow rates in and out are within 5%.

$$\epsilon_{m1} = \left| \frac{\overline{\dot{m}}^{\,n}_{L,\mathrm{in}} - \overline{\dot{m}}^{\,n}_{L,\mathrm{out}}}{\overline{\dot{m}}^{\,N}_{L,\mathrm{out}}} \right| \leq 0.05 \tag{4.8}$$

2. The average flow rate is steady with respect to time.

$$\epsilon_{m2} = \left| \frac{\overline{\dot{m}}^{\,n}_{L,\mathrm{out}}}{\overline{\dot{m}}^{\,N}_{L,\mathrm{out}}} - 1 \right| \leq 0.025 \tag{4.9}$$

In order to ensure the liquid discharge rate was accurately predicted, the simulation was run for a period of time such that the two liquid discharge rate convergence criteria were satisfied for a minimum of 0.5 s. This duration was selected based on preliminary trials to prevent prematurely stopping the simulation before the pseudo-steady operation was reached. The statistical sampling error was calculated for each run but was not strictly used as a convergence criterion for the liquid discharge rate. The sampling error was generally larger for the flow rate at the outlet than at the inlet. The statistical sampling error was typically less than 10%. Because $\overline{\dot{m}}_{L,\mathrm{in}}$ and $\overline{\dot{m}}_{L,\mathrm{out}}$ will not be exactly equal, the liquid discharge rate of the airlift pump was calculated as the average of the two.

$$\overline{\dot{m}}_{L} = \frac{\overline{\dot{m}}^{\,N}_{L,\mathrm{in}} + \overline{\dot{m}}^{\,N}_{L,\mathrm{out}}}{2} \tag{4.10}$$

Example Calculation of Liquid Discharge Rate

Figure 4.11 shows the period of transient airlift operation that occurs when the supplied air flow rate was adjusted. t' denotes the time within the pseudo-steady operation, such that $t' = 0$ corresponds to the beginning of the averaging period. The amplitude of the oscillations of the liquid suction rate progressively dampen out over the duration of the transient operation phase. The liquid flow rate at the outlet also exhibited a decaying low frequency oscillation during the transient operation, however it was far noisier. This transitional behaviour of the airlift pump lasted longer than the ramp up period of the supplied gas flow rate. Details of the transient airlift operation were not studied in this work. It is important however, to remove the transient portion of the signal to prevent it from affecting the statistics.

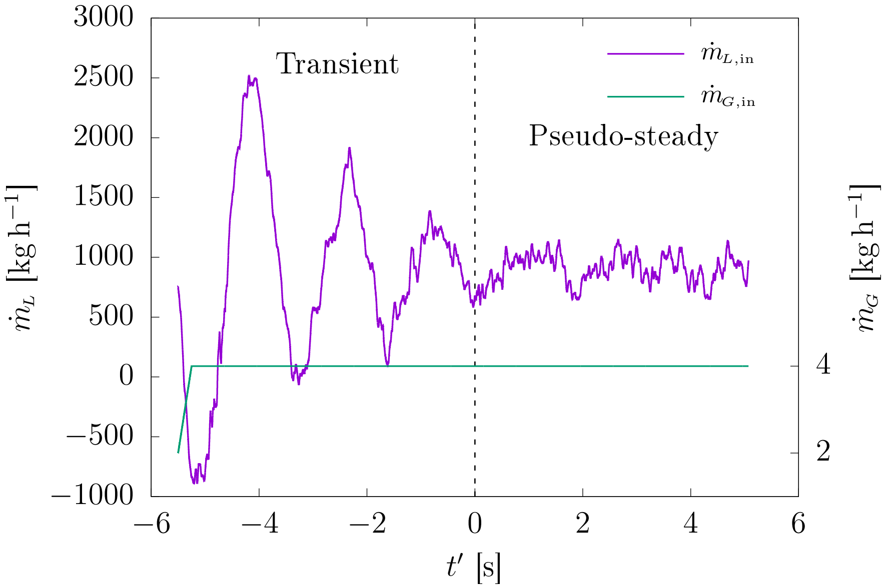

Figure 4.11: Subsiding transient oscillation of liquid flow rates when transitioning from 2 kg h^{-1} to 4 kg h^{-1} air flow rates.

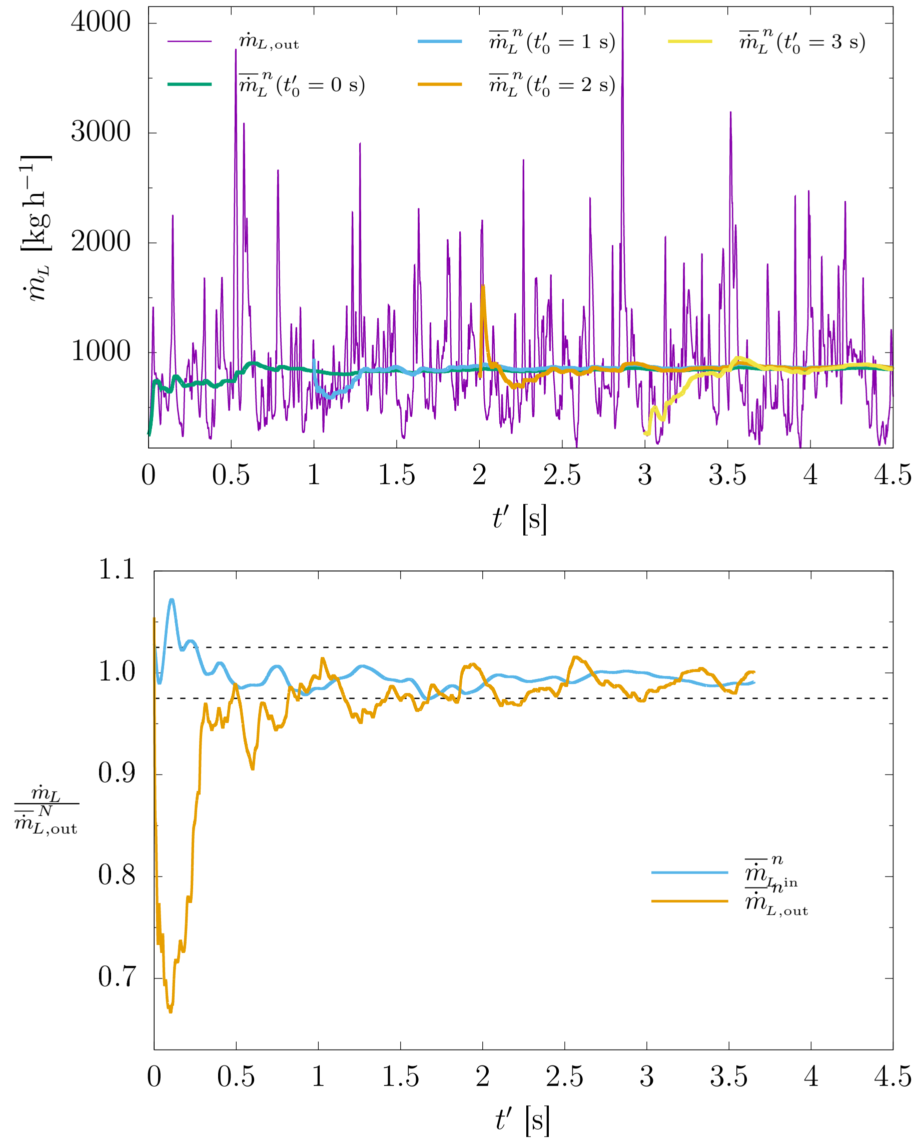

Figure 4.12: Accumulating average independence of sample length and convergence of flow rate. C1m6 operating point.

Figure 4.12 shows the convergence of the accumulating average which was described mathematically in Eqs. (4.8) and (4.9). It is clear that the average liquid flow rate of the inlet converges more quickly than at the outlet because the instantaneous signal is more stable with respect to time. The inlet signal is more stable because the chaotic high frequency oscillations caused by the local two-phase flow structures (as discussed in Section 5.2) are only present at the outlet. The duration of the transient period and the length of time required for the liquid discharge rate to converge during the pseudo-steady operation depends on the stability of the airlift pump (discussed in Section 5.2) at that particular operating point. On average, roughly 5 s of simulated time was needed to obtain a converged estimate of the liquid discharge rate.

CFX Average Solution Fields

ANSYS CFX has the convenient capability of storing an average solution field which can be used to produce time-averaged contour plots and line plots. The average solution field is recalculated and only stored for the current time step. Unlike the monitor point data used to calculate the liquid discharge rate, field values are not stored for every time step to avoid extreme disk space usage. The collection of the average solution field can be reset at the beginning of the simulation (which was done for each operating point) but a portion of the solution cannot be removed from the sample used to calculate the average in order to test the sensitivity. The CFX time-average was verified, however, by comparing an equivalent quantity averaged from monitor point data (such as riser void fraction). The sample duration for the monitor point average could be varied, and the accumulating average could be plotted as was done for the liquid discharge rate. The CFX time-average solution fields were generally consistent with the comparison against monitor points. There is no guarantee that all points within the solution field converge at the same rate.

4.6.3 Probability Distribution

As discussed in Section 1.1.2, comparing the PD distribution of the void fraction is an important tool for the objective determination of two-phase flow regimes. This requires calculating the PDF from a finite time signal of a continuous variable recorded from the simulation.

In the present work, the PDF of relevant time signals (ϕ) was produced using the Matlab `kdensity` function. The signal is broken into 100 discreet bins of equal width covering the range ϕ. The probability density of ϕ is calculated according to the count within the bin relative to the total number of samples. For a sufficiently large sample the discrete PDF accurately approximates the PDF of the continuous variable. The PDF is a normalized measure, meaning the integral of the PDF is always one.

Tests were performed to ensure the PDF profile was independent of sample length, meaning the signal was long enough to accurately capture the phenomena. It was found that if the simulation was run long enough for the liquid discharge rate to converge satisfactorily their was sufficient sample length for the PDF. As an example, the PDF of the same signal for various sample lengths is shown in Figure 4.13. The PD distribution did not change significantly, even with a sample as small as 0.5 s long.

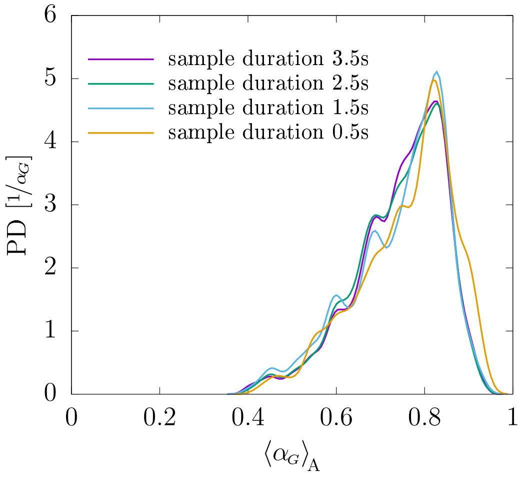

Figure 4.13: PDF of $\langle \alpha_G \rangle_A$ for various sample lengths.

A short sample of the cross-sectional-average void fraction time signal used to produce the PDFs seen in Figure 4.13 is shown in Figure 4.14. The monitor plane used to record the time signal was located 10 cm from the top of the riser. This location was selected to ensure the flow was well developed and the outlet boundary condition did not affect the results. The noisy and irregular nature of the void fraction time signal seen in Figure 4.14 (common to churn flow) emphasizes the need for a statistical analysis of the two-phase flow.

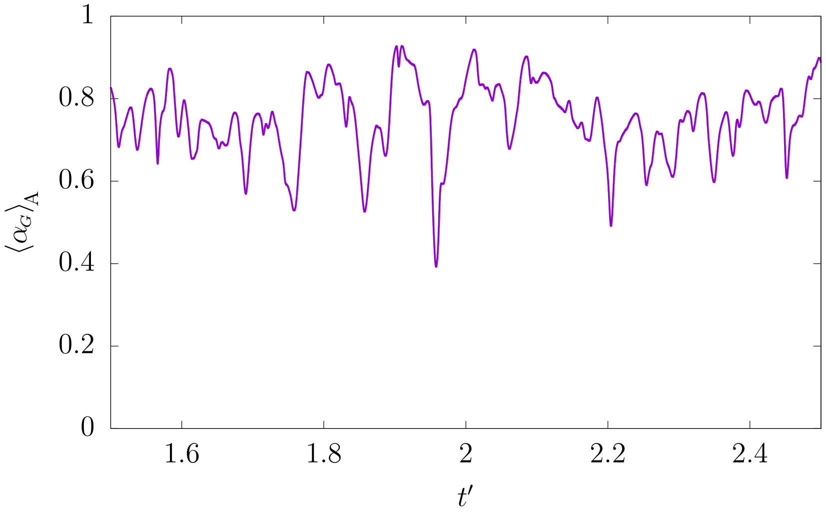

Figure 4.14: Sample of the cross-sectional-averaged void fraction time signal used to generate PDF seen in Figure 4.13.

4.7 Validation of Steady-State Algebraic Model

A Fortran program was written to implement the steady-state model of Kassab *et al.* [25]. The implicit non-linear algebraic equation was solved iteratively for the liquid flow rate using a Newton-Raphson root-search method. The solution of the model was repeated at a series gas flow rates to produced a smooth performance curve. To verify the model was programmed correctly, the results of the present work were compared to the published data of Kassab *et al.* [25]. Very minor deviations between curves were observed, however this can be attributed to the use of slightly different physical properties. A listing of the Fortran code can be found in Appendix D.2.

4.8 Comparison of Turbulence Models

The sensitivity of the simulation to the choice of turbulence model was examined for two operating points of the C1 configuration. The shorter riser length was selected to minimize computing time for the tests. A low and a high gas flow rate (C1m2 and C1m8), were used as a representative sample. The scope of this section is to compare the simulation results obtained from the two different turbulence models. A more focused discussion of the physics of the flow and the effects of gas flow rate and airlift pump configuration are presented in Section 5.

The predicted liquid discharge rate did not change significantly between the CFD simulations using the $k-\varepsilon$ and SST turbulence models for the two operating points tested, as seen in Table 4.6. It is assumed the predicted liquid discharge rate of other operating points are also insensitive to the choice of turbulence model. There are some differences in the finer details of the flow between the $k-\varepsilon$ and SST simulation. It is unclear however, whether the differences are a result of the turbulence model, the mesh density, or a combination of the two. Because of the negligible effect on liquid discharge rate and long computing time (approximately 6 weeks), no attempt was made to isolate the source.

Considering the other flow statistics summarized in Table 4.6, the average void fraction and maximum of time averaged velocity are practically equivalent. The RMS of the instantaneous mass flow rates were similar between models with the exception of the suction flow rate ($\dot{m}_{L,in}$) for the 2 $\mathrm{kg\,h^{-1}}$ operating point. The time series of these signals are shown in Figure 4.15. The different dynamic characteristics of the suction flow rate signals are also seen in Figure 4.16(b). The SST model exhibits a more regular periodic large amplitude oscillation, repeatedly having a negative suction flow rate. The periodic nature of the SST signal is reflected in the two humps in the PDF. The $k-\varepsilon$ model has one brief region of negative inflow but it does not recur. It is possible the simulation using the SST model is exhibiting airlift pump instabilities that are gradually dampening out over time. Increasing the simulation period could provide greater insight into these dynamic effects, unfortunately this was not possible given the computing time restrictions.

Table 4.6: Effect of turbulence model on flow statistics.

		$\overline{\dot{m}_L}$ [$\mathrm{kg\,h^{-1}}$]	$\dot{m}^{\mathrm{rms}}_{L,\mathrm{in}}$ [$\mathrm{kg\,h^{-1}}$]	$\dot{m}^{\mathrm{rms}}_{L,\mathrm{out}}$ [$\mathrm{kg\,h^{-1}}$]	$\langle\overline{\alpha}_G\rangle_V$	$\max\overline{v}$
C1m2	$k-\varepsilon$	347	167	309	0.621	5.022
	SST	373	308	352	0.624	4.678
C1m8	$k-\varepsilon$	890	136	511	0.803	8.01
	SST	918	147	456	0.767	9.13

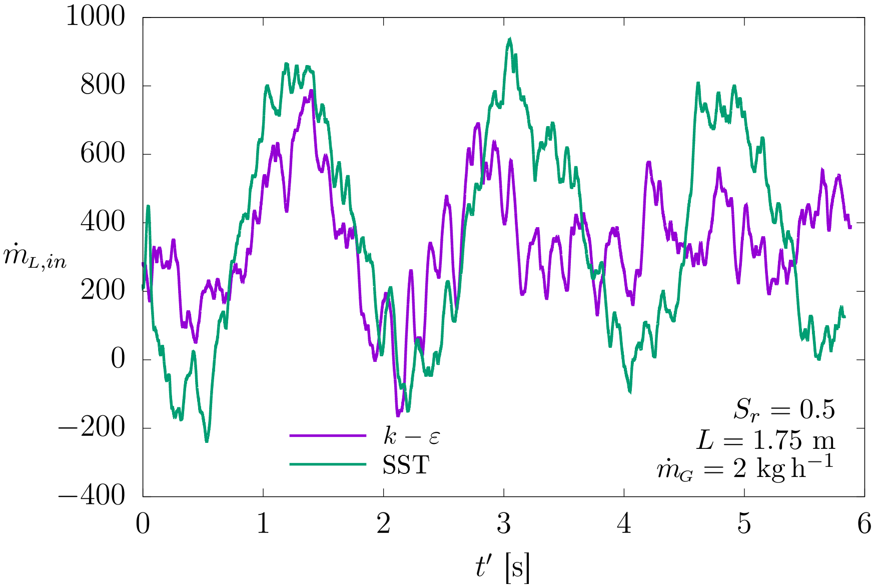

Figure 4.15: Effect of the turbulence model on the dynamic behaviour of the suction flow rate at the C1m2 operating point.

The phasic distribution is relatively similar between models. Visually the SST solutions have sharper contours of α_G, but this is purely due to the increased mesh density. Sample contours demonstrating this can be seen in Appendix C.1. Examining the PD distributions of void fraction seen in Figure 4.16(a), the SST solution has a wider distribution than the $k-\varepsilon$ model at the 2 $\mathrm{kg\,h^{-1}}$ operating point. Conversely, the SST model has a narrower distribution than the $k-\varepsilon$ model at the 8 $\mathrm{kg\,h^{-1}}$ operating point.

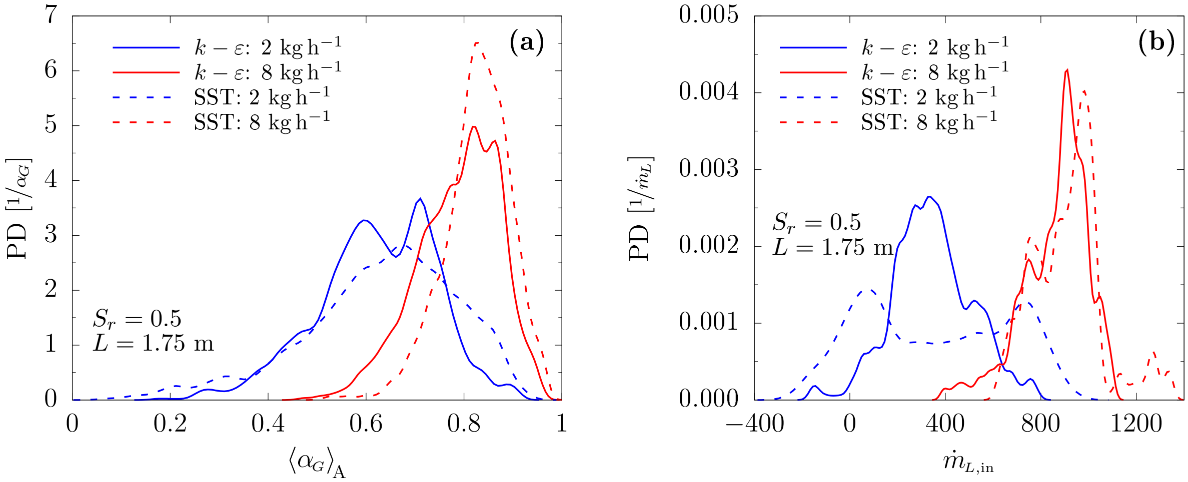

Figure 4.16: Effect of turbulence models on PD distributions of: (a) area-averaged void fraction and (b) suction flow rate.

Regarding the the time-averaged axial profiles shown in Figure 4.17, the $\dot{m}_G = 2$ kg h^{-1} operating point profiles are essentially equivalent given the associated uncertainties in collecting time averaged. The $\dot{m}_G = 2$ kg h^{-1} curves are not as smooth as the $\dot{m}_G = 8$ kg h^{-1} curves because the time-average is not as well converged, despite the fact that the $\dot{m}_G = 2$ kg h^{-1} case has a longer sample length. This is due to the nature of the flow regime at the different operating points. At $\dot{m}_G = 2$ kg h^{-1}, the gas and liquid pockets are larger and more distinct (closer to slug flow) than the $\dot{m}_G = 8$ kg h^{-1} case. The more intermittent the phasic distribution, the slower the statistical convergence of the time-averaged solution field. The large discrepancy in wall shear stress (Figure 4.17(b)) between the $k-\varepsilon$ and SST models at $\dot{m}_G = 8$ kg h^{-1} can be attributed to recirculation of the flow. When reverse flow occurs it effectively lowers the average value because it is a negative value in the arithmetic average.

There is a level of uncertainty to the exact values of the time-averaged axial and radial profiles because they are generated from an averaged solution field calculated by CFX, as discussed in Section 4.6.2. It is possible the time-averaged profiles contain some residual effects from the transient operation. Emphasis should be put on the shape and trends of the time-averaged profiles and not the exact values.

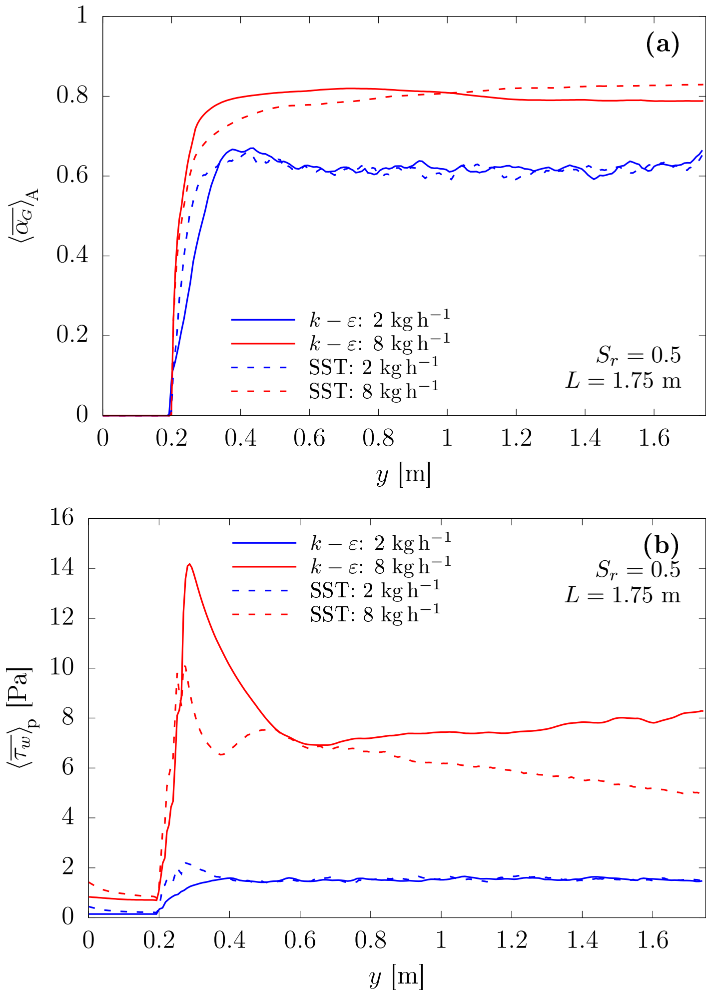

Figure 4.17: Effect of turbulence models on time-averaged axial profiles of: (a) area-averaged void fraction, and (b) perimeter-averaged wall shear stress.

The area-average void fraction is practically equivalent between $k-\varepsilon$ and SST turbulence model results but this does not guarantee the radial distribution is the same. Recall from Section 4.2, the time-averaged solution is essentially axisymmetric (Figure 4.2), therefore the angular location is not significant when considering the radial distribution of time-averaged quantities. The radial profiles of time-averaged void fraction measured from the top portion of the riser where the flow is well-developed are shown in Figure 4.18. The SST results have a lower void fraction near the wall of the pipe and a higher centerline void fraction. The increased mesh resolution near the wall required for the SST model (not just the turbulence model alone) is likely to have influenced the near wall void fraction because smaller interfacial length scales can be resolved in that region. Because the instantaneous phasic distribution varies considerably from the axisymmetric time-averaged solution, it is unclear from Figure 4.18 alone whether the phasic interface is simply sharper in the SST model producing a different time-averaged solution or the phasic interface shape is somewhat different.

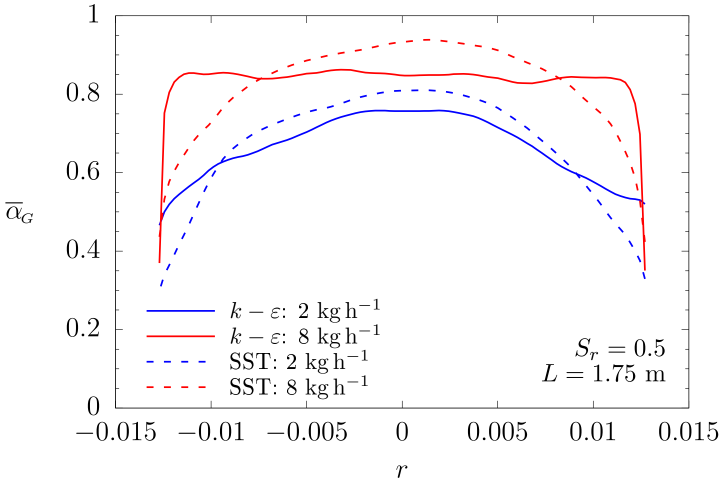

Figure 4.18: Radial profile of time-averaged void fraction at $y = 1.6$ m.

The present analysis indicates that both the CFD model using the $k-\varepsilon$ and the SST turbulence models provided a reasonable prediction of the flow. The average quantities measured from the simulation were practically independent of the choice of the turbulence model. The simulation using the SST model, however, requires significantly more computing time than the simulations using the $k-\varepsilon$ model. Based on these finding, the $k-\varepsilon$ model is used in the remainder of this work.

Chapter 5

Results and Discussion

Simulations were performed for a total of thirteen operating points consisting of three different airlift pump configurations formed from two different riser lengths and two different submergence ratios. Results are only considered for the pseudo-steady-state operation of the airlift pump. The airlift pump behaviour during the start up period is not examined in this work.

The simulation results are first examined in terms of the predicted performance curve and agreement with the experimental measurements, steady-state model, and flow regime map. Next, the dynamic behaviour of the airlift pump and airlift pump instability are studied. The effects of gas flow rate, submergence ratio and riser length on the two-phase flow in the airlift pump are explored using time-averaged axial profiles and PD distributions. Temporal-spatial-averaged quantities of the flow in the airlift pump are examined in relation to the steady-state algebraic model and published two-phase flow correlations. Lastly, topics for the continuation of this research are suggested.

5.1 Prediction of Airlift Pump Performance

The liquid discharge rate predicted by the CFD model is compared against the experimentally measured performance curve and steady-state model of Kassab *et al.* [25], as seen in Figure 5.1. The code used to implement the steady-state model and produce the "Kasssab Model" curves was described in Section 4.7. The "Present work" points are for the simulations using the $k - \varepsilon$ turbulence model. Qualitatively, the CFD simulation data points fit the overall trend of the airlift performance curve.

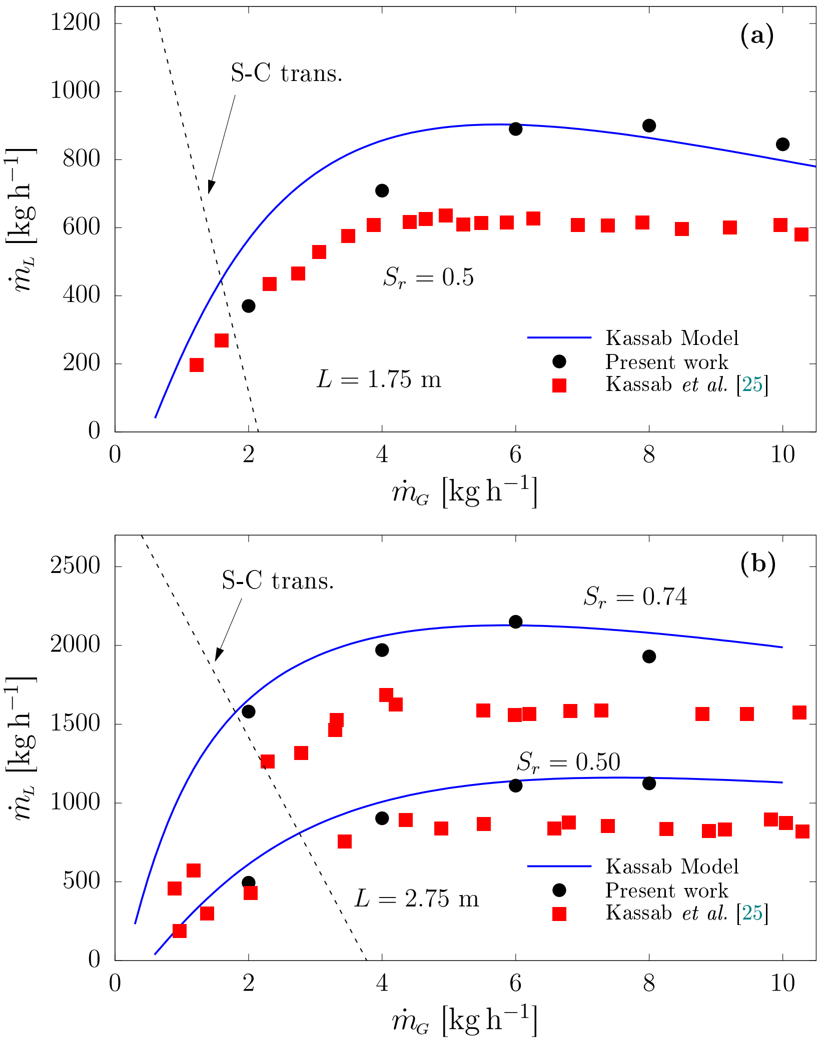

Figure 5.1: Comparison of predicted airlift performance curves to experiment. (a) C1: $L = 1.75$ m $S_r = 0.5$, (b) C2: $L = 2.75$ m $S_r = 0.74$ and C3: $L = 2.75$ m $S_r = 0.5$.

5.1.1 Agreement Between Models and Experiment

The liquid discharge rate predicted by the CFD simulations have superior agreement with the experiment than the steady-state model at lower gas flow rates ($\dot{m}_G \leq 4$ kg h^{-1}), and similar agreement at higher gas flow rates. The RMS deviation between the performance curve predicted by the CFD simulation and the experimental measurements is roughly 30%

for C1 and C2, and 20% for C3.

The deviation between the CFD model and the steady-state model is 17% for the C1 configuration (shorter riser) and less than 10% for the C2 and C3 configurations (longer riser). This implies the predictions of the steady-state model match the CFD predictions more closely when the two-phase flow conditions of the airlift pump better resemble the two-phase flow conditions in which the void and frictional pressure drop correlations were derived for, as elaborated on in Section 5.5.2.

The liquid discharge rate is overpredicted by the present CFD model and the steady-state algebraic model. As mentioned in Section 4.1.1, some assumptions about the gas flow entering the riser pipe through the air jacket were necessary. Both models neglect major and minor head losses occurring between the supply tank and the beginning of the riser pipe. Although these losses are assumed to be minor, they would undoubtedly contribute to the overprediction of the liquid discharge rate. Furthermore, the relative magnitude of the entrance losses would increase with increasing flow rate. Both the present CFD model and the steady-state model do not account for the effects of the internal structure of the airjacket on the gas flow. Because of the way the computational domain was set up, the present CFD simulations represent an idealized case of the airlift pump which shares many similarities with the SS model.

5.1.2 Agreement of CFD with Flow Regime Map

All but one simulated operating points occur within the churn flow region of the Taitel *et al.* [12] flow map. The equations for transition lines have been transformed from units of superficial velocity to mass flow rate. The slug-to-churn transition occurs at different locations on Figure 5.1(a) and (b) because the transition depends on the value of L/D. The other transition lines of the Taitel *et al.* [12] flow map do not appear on Figure 5.1 because they fall outside the range of flow rates encountered in the simulation. Overall, the flow regime observed in the CFD simulation is consistent with the regime predicted by the Taitel *et al.* [12] flow map but a more thorough examination of the flow characteristics is provided in the following sections. Kassab *et al.* [25] found the Taitel *et al.* [12] flow map to be consistent with the experimentally observed flow regimes in their airlift pump experiments.

As discussed in Section 2.1, Moisidis and Kastrinakis [27] proposed flow regime transitions for the airlift pump as a function of J_G and S_r. The slug-to-churn transition would appear as a vertical line on Figure 5.1 at around $\dot{m}_G = 4.7\ \mathrm{kg\,h^{-1}}$ for $S_r = 0.5$ and at around $\dot{m}_G = 9$ $\mathrm{kg\,h^{-1}}$ for $S_r = 0.74$. The transition line of Moisidis and Kastrinakis does not agree well with the CFD results nor does it agree with the standard two-phase flow map of Taitel *et al.* [12].

It should be noted the C3m2 operating point occurs within the slug flow region of the Taitel *et al.* flow map, but slug flow was not observed in the simulation results. At this operating point the simulated airlift pump was exhibiting signs of unstable operation. Unstable behaviour of the airlift pump (discussed in Section 2.1.4) means the flow rate fluctuates significantly with time but an average discharge rate can still be calculated. In regards to the flow regime present at the C3m2 operating point, there were intermittent periods of slug-like flow followed by high void fraction churn-like flow. This phenomena is explored further in Section 5.2.1.

5.2 Dynamic Behaviour of Airlift Pump

The liquid discharge rate (an average value) shown in the performance curves does not give a complete description of the flow. The suction flow rate, however, is an important quantity for understanding the dynamic behaviour of the airlift pump. It will be demonstrated that there is a relationship between the $\dot{m}_{L,in}$, $\langle\alpha_G\rangle_V$ in the riser pipe, and the frequency of oscillations in $\dot{m}_{L,out}$.

The time series of suction flow rate and riser void fraction are plotted for two operating points in Figure 5.2; C3m2 which was previously stated to be unstable, and C2m6 which is stable. In order to make a fair comparison of operating points with different liquid discharge rates, the instantaneous value is normalized by the corresponding time-average. The normalized time signal is denoted by $\widehat{R}$ with a subscript indicating the particular quantity.

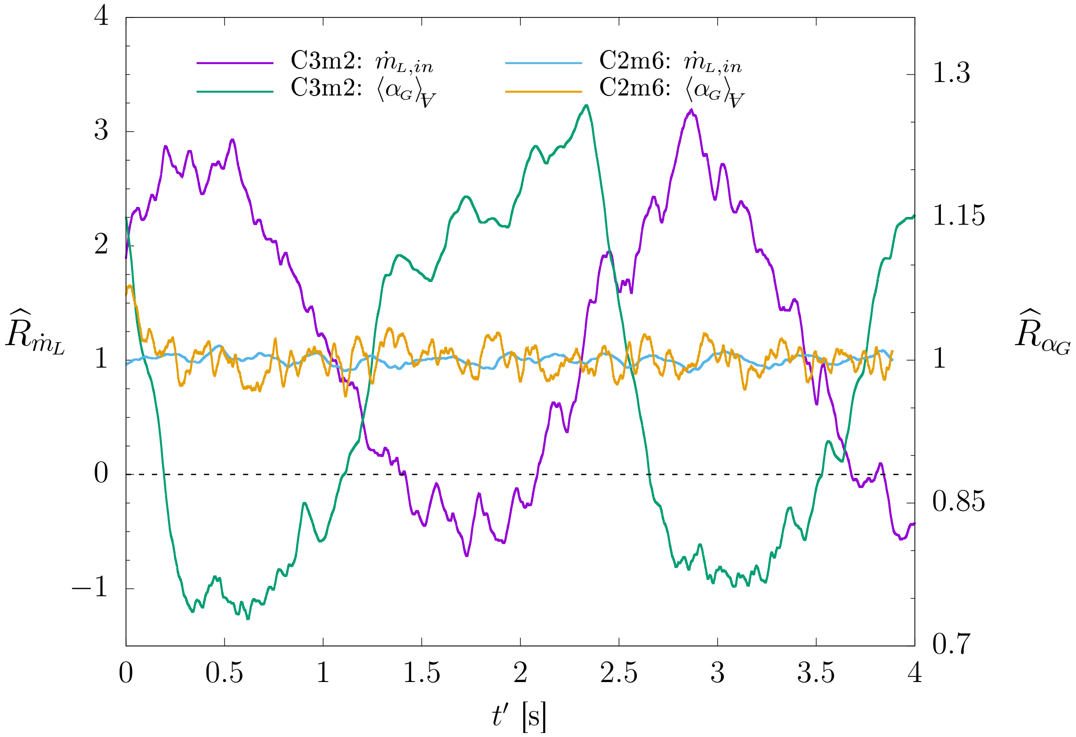

Figure 5.2: Time signal of suction flow rate and riser volume fraction normalized by their respective mean value during stable and unstable airlift pump operation. The dashed horizontal line indicates where negative suction flow rate occurs.

In the C3m2 case, the suction flow rate exhibits a low frequency and large amplitude periodic oscillation about the mean flow rate, as seen in Figure 5.2. The fluctuations caused by two-phase flow structures (such as slugs) occur at a higher frequency (1-20 Hz) [68]. The observed period of ≈ 2.4 s or 0.42 Hz is within the range of airlift pump instability reported by de Cachard and Delhaye based on theoretical analysis [68]. The suction flow rate of the C2m6 operating point is nearly constant with respect to time. The instantaneous riser volume fraction reflects the behaviour of the suction flow rate, but the range of fluctuations with respect to the mean is much smaller. When the suction flow rate has a periodic oscillation, the peak suction rate coincides with a minimum gas volume fraction and vice versa. The $\dot{m}_{L,in}$ and $\langle\alpha_G\rangle_V$ time signals are not exactly a half period out of phase with each other; $\dot{m}_{L,in}$ continues to increase after $\langle\alpha_G\rangle_V$ has reached its maximum and begins to fall. This overshooting behaviour is an indication of instability in the system, which prevents oscillations of the suction flow rate from dampening out. The fluctuations of the riser volume fraction in the C2m6 case are more chaotic than the C3m2 case, and are not clearly related to the suction flow rate.

To examine the relationship between the suction flow rate and the liquid exiting the riser, smoothing had to be applied to the instantaneous signals. A moving mean smoothing ($\tilde{\bar{\dot{m}}}$) is calculated over a central window of 0.3 s. This duration was selected to dampen out the high frequency oscillations of the flow rate associated with the phasic distribution of the two-phase flow, which are observed at the outlet. The same two cases examined above (C3m2 and C2m6) are shown in Figure 5.3(a) and (b), respectively.

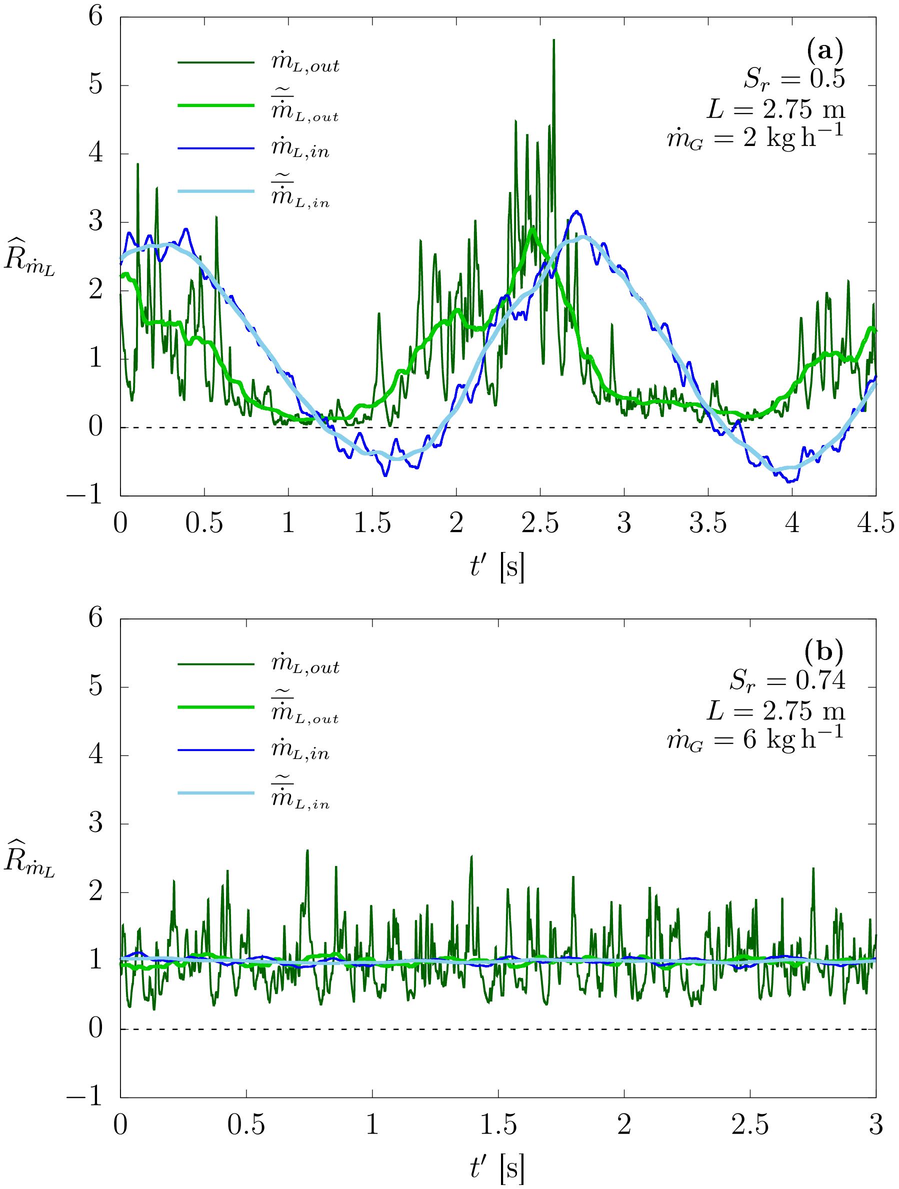

Figure 5.3: Typical flow rate oscillations during (a) unstable, and (b) stable operation.

Considering the unstable case, the large amplitude low frequency oscillations of the liquid flow rate at the outlet are more obvious in the smoothed signal. The amplitude of the periodic oscillation of liquid flow rate is slightly less at the outlet than at the inlet. It is not possible to have a negative liquid flow rate at the outlet because water is not allowed to flow back into the computational domain (per the boundary conditions specified in Section 3.1). As seen in the $\dot{m}_{L,in}$ and $\langle \alpha_G \rangle_V$ signals, the periodic oscillation of $\dot{m}_{L,in}$ and $\dot{m}_{L,out}$ are out of phase. There is a delay between the maximum flow rate at the outlet and inlet.

In the stable case, $\dot{m}_{L,in}$, $\tilde{\tilde{\dot{m}}}_{L,\mathrm{in}}$, and $\tilde{\tilde{\dot{m}}}_{L,\mathrm{out}}$ are essentially constant and only $\dot{m}_{L,out}$ fluctuates considerably with time. As previously stated, the high frequency fluctuations in $\dot{m}_{L,out}$ are related to the local two-phase flow structures. In slug or churn flow, liquid and gas exit the riser pipe intermittently in large discrete bursts. These high frequency fluctuations in phase-dependent flow rate are linked to the fluctuation of void fraction averaged over a cross-section (which is used to characterize the flow regime in Section 5.4). The fluctuation of the liquid flow rate from the smoothed value ($\dot{m}_{L,out} - \tilde{\tilde{\dot{m}}}_{L,\mathrm{out}}$) is qualitatively similar in both unstable and stable operation cases presented in Figure 5.3.

To examine the behaviour of the time-variation of the volume fraction in the airlift pump, the RMS of the $\langle \alpha_G \rangle_V$ time signal was calculated and normalized by the time average value ($\langle \overline{\alpha_G} \rangle_V$). The details of the transient variation of the signal are lost when the RMS is calculated, but the single value better facilitates comparison between many cases. It is not practical to compare the time-dependent signals from the 13 simulated operating points simultaneously. Figure 5.4 shows the normalized RMS of riser void fraction as a function of gas flow rate. The unstable operation point (C3m2) clearly stands out from the rest of the data. Based on the present data, the time-dependent fluctuations of riser volume fraction are roughly four times greater during unstable operation compared to stable operation. The decrease in the magnitude of the fluctuations of riser volume fraction with increase to gas flow rate are consistent with the experimentally observed findings of Tighzert *et al.* [29]. The downward trend shown by the curves of Figure 5.4 demonstrates that increasing the gas flow rate dampens the instabilities in the airlift system, even during stable operation. Excluding the unstable operating point, it appears the airlift pump configuration has a negligible effect on the magnitude of fluctuations of the riser volume fraction.

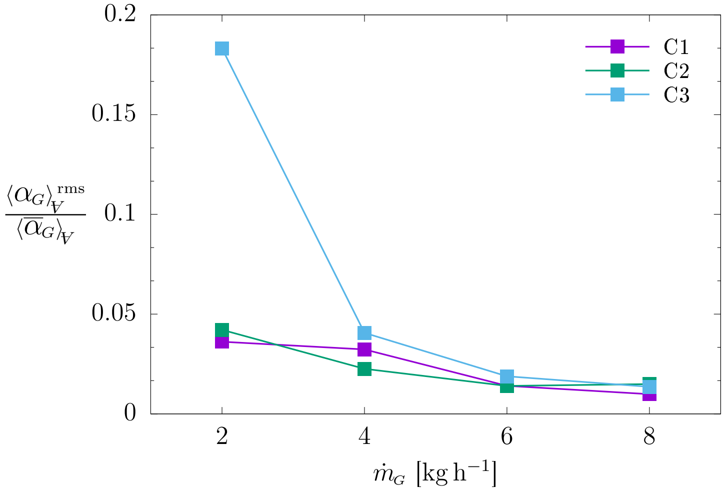

Figure 5.4: Effect of gas flow rate on RMS of the time-variation of riser volume fraction.

Understanding the dynamic behaviour of the airlift pump is important because the more the suction flow rate varies with time, the more the two-phase flow in the airlift pump can be expected to deviate from standard two-phase flow theory (which requires that both phases enter at constant flow rates). The nonlinear nature of the physics poses a problem for simplified steady-state modeling. For example, consider the hypothetical situation of single-phase liquid flowing in a pipe: Case A has a constant velocity of 2 m s^{-1} and Case B has a velocity behaving in alternating step function of 1 or 3 m s^{-1}. The average velocity and mass flow rate of Cases A and B are the same, but the frictional pressure drop is not. Because the frictional losses are proportional to U^2, Case B has a larger frictional pressure drop than Case A. The physics of the airlift pump and two-phase flow is far more complex than this simple example but the principle holds true. The time-average value of relevant forces are not necessarily well predicted by correlations based on the average flow rate. This issue, and the quantitative comparison of force balance terms, is explored further in Section 5.5.2.

In general, the fluctuation of the suction flow rate reflect the dynamic behaviour of the system as a whole (global), whereas the fluctuations of the eduction flow rate are a superposition of the global fluctuation (low frequency) and local flow structures (high frequency). The dynamic behaviour of the system depends on the airlift pump geometry and air flow rate.

5.2.1 Airlift Pump Instability

The effect of airlift pump instabilities on integral parameters has been established in the prior section, but the two-phase flow characteristic have not yet been explored. As stated in Section 5.1, C3m2 falls within the slug flow region of the Taitel *et al.* [12] flow regime map. The point on the performance curve and flow map is based on the average flow rates. The liquid flow rate, however, varies by as much as two times the average value and has reoccurring periods of negative suction flow rate. These conditions differ greatly from what the flow map was designed for, so it is unreasonable to assume the flow regime map is reliable in this situation. In the simulation, intermittent and alternating regions of slug-like flow and high void fraction churn-like flow were observed in the airlift riser. These distinct regions progress upward along the riser as demonstrated in Figure 5.5, which shows instantaneous contours of void fraction at three snapshots in time. For better visualization, the riser pipe is split into four pieces arranged from left to right, as indicated by numbers 1 to 4 on the top of the figure. The bottom of the high void fraction churn region travels upward from B2 at $t' = 5.4$ s, to D2 at $t' = 5.4$ s, and finally C3 at $t' = 5.8$ s. Discrete slug-like gas pockets can be seen at $t' = 5.8$ s split between D2 and A3.

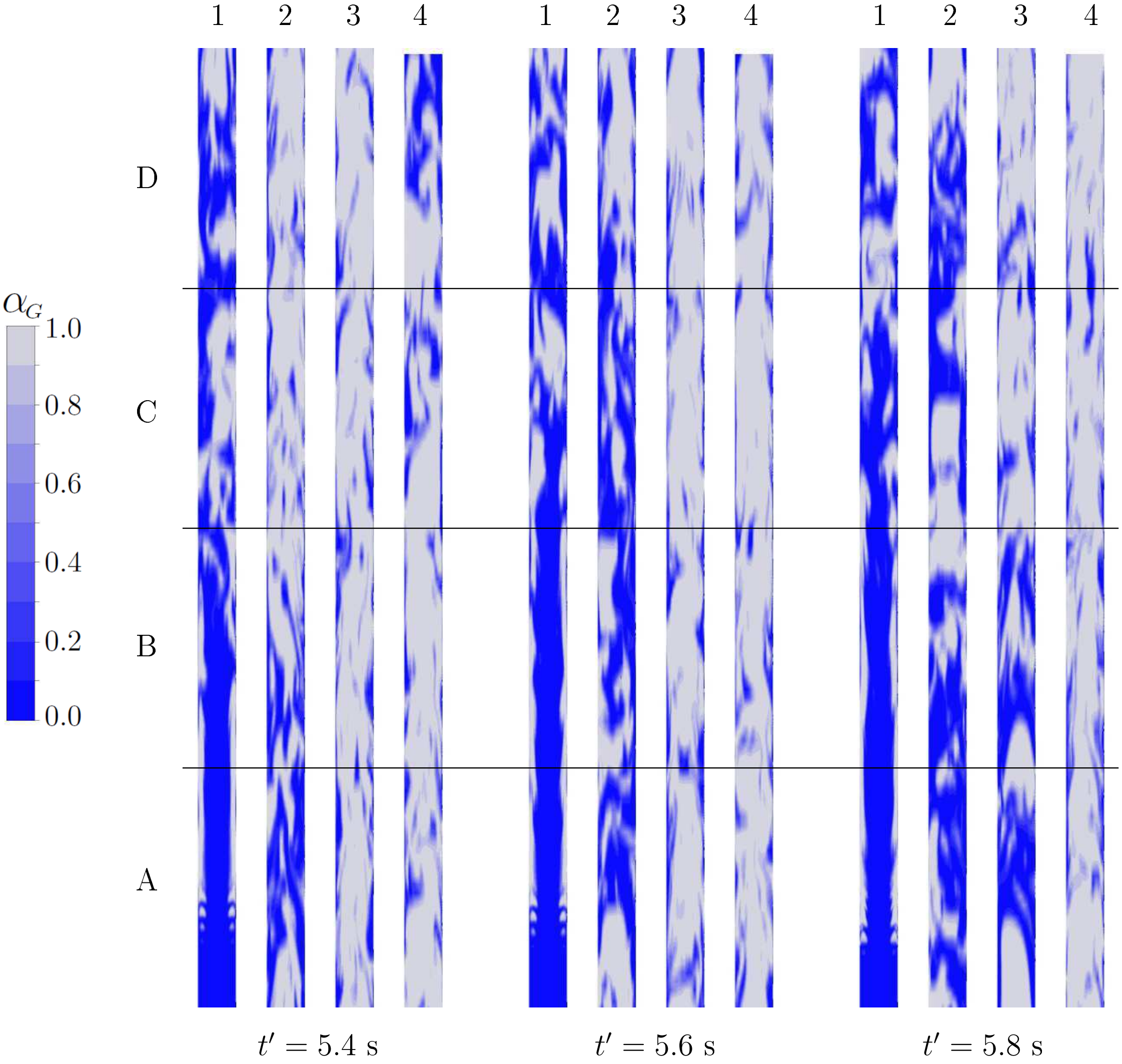

Figure 5.5: Simultaneous regions of slug-like and churn-like flow in the riser pipe of C3m2 ($L = 2.75$ m, $S_r = 0.5$, $\dot{m}_G = 2$ kg h^{-1}) operating point at three snapshots in time. The riser pipe is shown in four pieces, the flow enters A1 and exits D4.

Although the motion of the flow being discharged from the riser pipe to the surroundings is not modeled in the present simulation, it is reasonable to assume the alternating regions of slug-like and churn-like flow would produce intermittent burst of liquid exiting the riser pipe. The anticipated discharge flow behaviour from the CFD simulation of the C3m2 operating point is similar to the description of the flow given by Lawniczak *et al.* [23] for short airlift pumps operating at low submergence ratios.

In theory, large pockets of high void fraction churn-like flow are formed when the riser void fraction is too low and the suction rate enters a period of near-zero or negative flow. The details of the flow near the air injector region during one of the reverse flow periods is shown in Figure 5.6. The liquid falls downward while the gas flow remains mostly upwards due to buoyancy. As the liquid flows out of the suction pipe, the gas is pulled further down into the air injection region where it accumulates until the buoyancy force becomes large enough to drive the entire column upwards. This large pocket of high void fraction progresses upwards and forms the churn-like region seen in Figure 5.5.

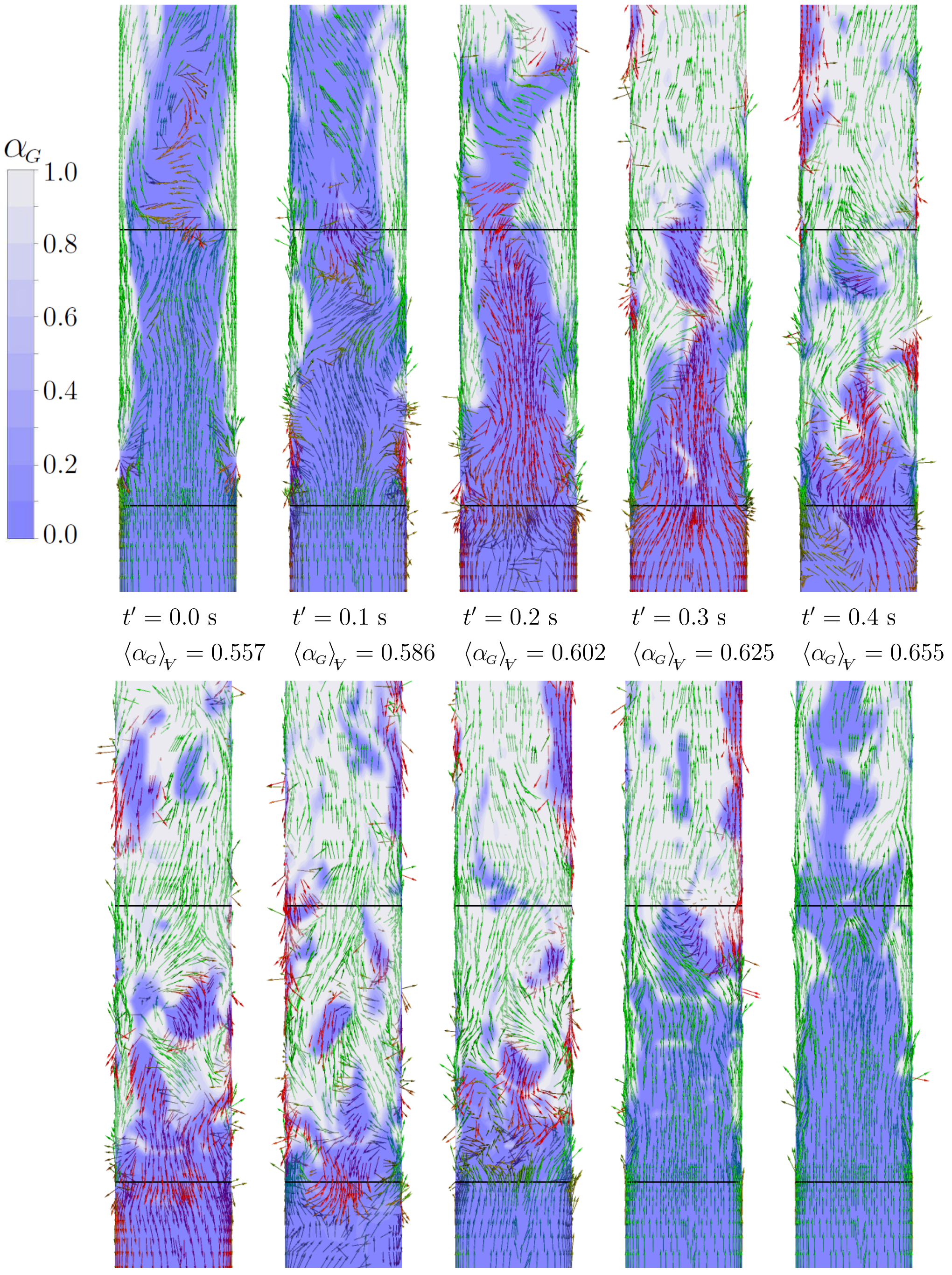

$t' = 0.0$ s $\langle\alpha_G\rangle_V = 0.557$

$t' = 0.1$ s $\langle\alpha_G\rangle_V = 0.586$

$t' = 0.2$ s $\langle\alpha_G\rangle_V = 0.602$

$t' = 0.3$ s $\langle\alpha_G\rangle_V = 0.625$

$t' = 0.4$ s $\langle\alpha_G\rangle_V = 0.655$

$t' = 0.5$ s $\langle\alpha_G\rangle_V = 0.658$

$t' = 0.6$ s $\langle\alpha_G\rangle_V = 0.669$

$t' = 0.7$ s $\langle\alpha_G\rangle_V = 0.731$

$t' = 0.8$ s $\langle\alpha_G\rangle_V = 0.748$

$t' = 0.9$ s $\langle\alpha_G\rangle_V = 0.725$

Figure 5.6: Flow in the air injector during back flow period of case C3m2. Contour of void fraction and velocity vectors are shown to indicate the motion of the as and liquid. The velocity vectors are coloured by axial direction; red for downward flow, green for upward flow.

It is important to note that during the periods of reverse flow, the gas was not drawn out the bottom of the suction pipe. This trend is important for the physical consistency of the simulation and the boundary conditions. Because of the boundary conditions applied in this simulation, if gas were to exit the suction pipe it would be lost from the system. In the experimental apparatus of Kassab *et al.* [25] the gas would eventually travel back up to the riser and exit the system through the outlet. This scenario is the reason a sufficient length of entrance pipe was a critical aspect of the computational domain.

It is recognized that the assumptions made in forming the computational domain and boundary conditions may affect the stability of the airlift system. de Cachard and Delhaye [21] observed that the liquid and gas feed systems affect the stability of the airlift pump. Unfortunately the airlift pump instability observed in the present simulations cannot be validated by the experiments of Kassab *et al.* [25] because the authors did not examine airlift stability.

5.2.2 Development Length

The developing region of the two-phase flow originating from the air injector is of interest to the study of the airlift pump and more specifically improved methods of air injection. In the present work this region typically spans 3 to 30% of the total riser length. It is reasonable to assume that the two-phase flow development in the lower portion of the riser depends on the air injector design. For example, the flow a short distance away from a nozzle would be very different from that of an air jacket. Unfortunately there are no experimental measurements by Kassab *et al.* [25] to compare the accuracy of the CFD results against, nor are there CFD results by other authors using different air injectors.

Previously in Section 5.2.1, the local flow characteristics of the air injector region were explored qualitatively with contour plots in relation to the variation of riser volume fraction and airlift pump instability. To measure the development length of the two-phase flow a more objective method is required. Assuming that either slug or churn flow is the fully developed flow regime, a common trait of either regime is large gas pockets at the core of the tube. In the air injection region, gas enters from the exterior of the tube while liquid flows upward in a central core. In the developing region of the flow the gas must penetrate the liquid column to form defined flow structures. Therefore the development length is measured as the distance between the airjacket and the first gas pocket occupying the centre of the tube. The first gas pocket is determined from the CFD results as the lowest axial location where the local void fraction at the centerline is greater than 0.97. Figure 5.7 shows what the developing region of the flow typically looks like and how it is measured.

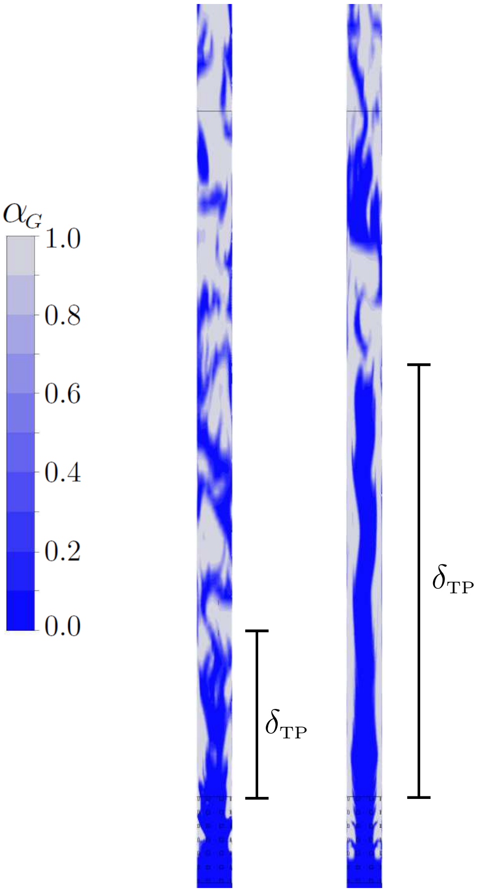

Figure 5.7: Example of two-phase flow pattern development length calculated from CFD results for two different cases.

For each simulated operating point, the development length was measured from the series of instantaneous solution fields saved at 0.2 s intervals. The average development length was then calculated as the arithmetic mean of the samples. In some cases, the development length did not fluctuate significantly with time, whereas in others (such as the unstable case of C3m2) it oscillated considerably. The reliability of these measurements was evaluated by comparing against the results from different meshes and the tests with the SST turbulence model. It was found that the value depended significantly on the mesh and or turbulence model but the overall trends remained consistent. Additionally, the number of samples available to measure the development length is limited. Thus, the results presented in Table 5.1 should only be considered as estimates.

Table 5.1: Summary of approximate average development length (in [cm]) measured from CFD results.

	$2\ \mathrm{kg\,h^{-1}}$	$4\ \mathrm{kg\,h^{-1}}$	$6\ \mathrm{kg\,h^{-1}}$	$8\ \mathrm{kg\,h^{-1}}$	$10\ \mathrm{kg\,h^{-1}}$
C1	8.8	13.1	42.5	25.3	15.7
C2	42.8	64.0	78.1	81.6	-
C3	26.3	26.7	21.2	8.4	-

In regards to the effect of $\dot{m}_G$ on the development length, the average development length first increased with $\dot{m}_G$ until a maximum was reached, then decreased with further increase to $\dot{m}_G$. The gas flow rate also had an effect on the the stability of the development length: as $\dot{m}_G$ increased the variation in the instantaneous development length decreased. The stability of the development length appears to be directly related to the stability of the suction flow rate. The sampling frequency of the development length measurements was too low to allow a quantitative study of its time variation.

The average development length increases and becomes more stable with an increase to the submergence ratio. The submergence ratio has the same effect on the suction flow rate as it does on the development length. Therefore, the behaviour of the development length and the suction flow rate are strongly coupled.

5.3 Comparison of Time-averaged Results

Plotting the axial variation of cross-sectional-averaged quantities is a useful tool for understanding the evolution of flow structures along the length of the airlift pump. The instantaneous quantities provide insight into the flow regime at a given $\dot{m}_G$ or tube geometry, whereas the time-average quantities are more suitable for comparing trends between cases of different gas flow rates and geometries.

The same general shape to the axial profiles is observed for all airlift pump configurations examined in this work. Consequently, only cases C1 and C2 are shown in Figures 5.8 and 5.9, respectively. For completeness, case C3 can be found in Appendix C.2. Regarding the the void fraction (Figures 5.8(a) and 5.9(a)), there is an abrupt increase in void at the air injector where the gas is introduced. Next, there is a rounding over of the curve as it transitions from near vertical to near horizontal. This is the region where, in the average sense, the flow regime is still developing. Lastly, the void fraction is nearly constant with further increase in length, where the two-phase flow regime is well-developed. A small increase in void fraction along the length of the well-developed region is expected due to expansion of the gas as the pressure decreases. The expansion effects, however, are minimal in shorter tubes.

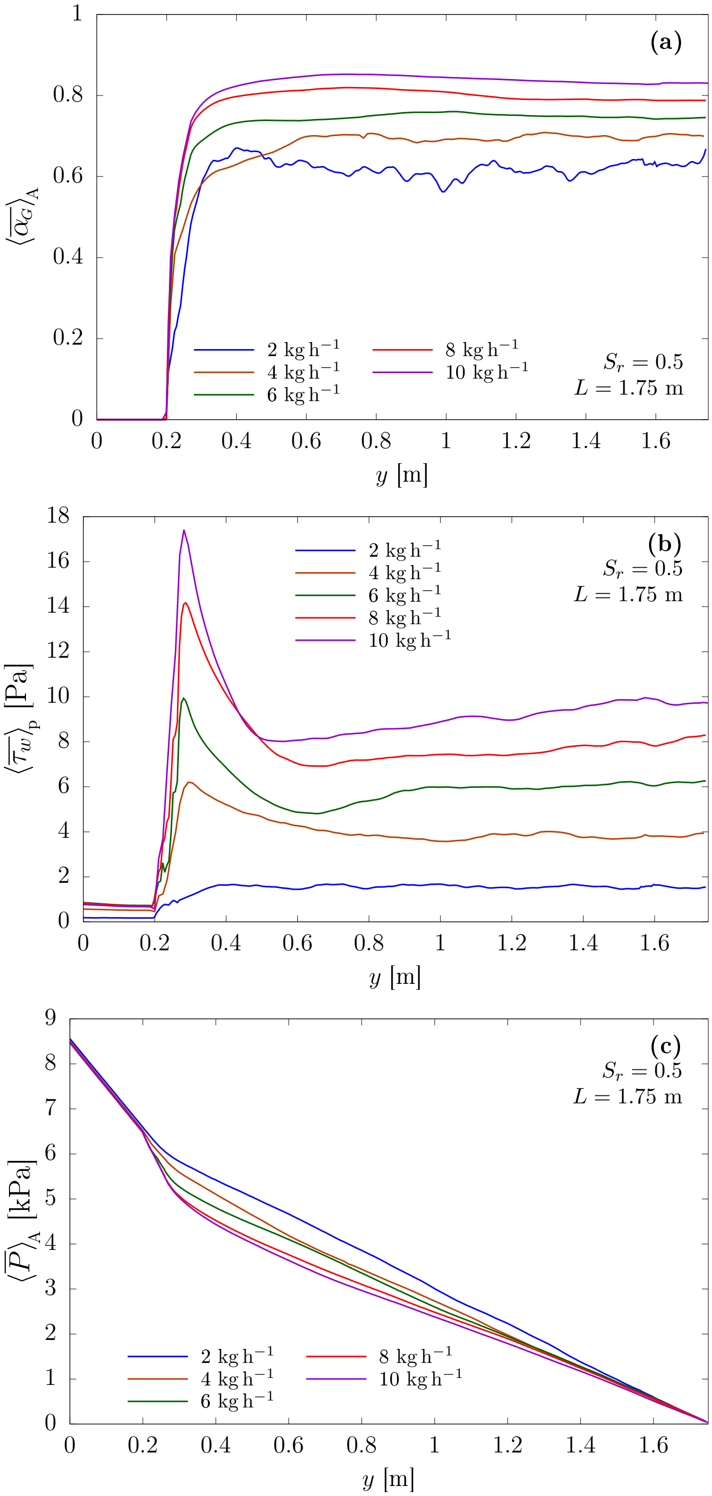

Figure 5.8: Time-average axial profiles for C1: (a) area-averaged void fraction, (b) perimeter-averaged wall shear stress, and (c) area-averaged pressure.

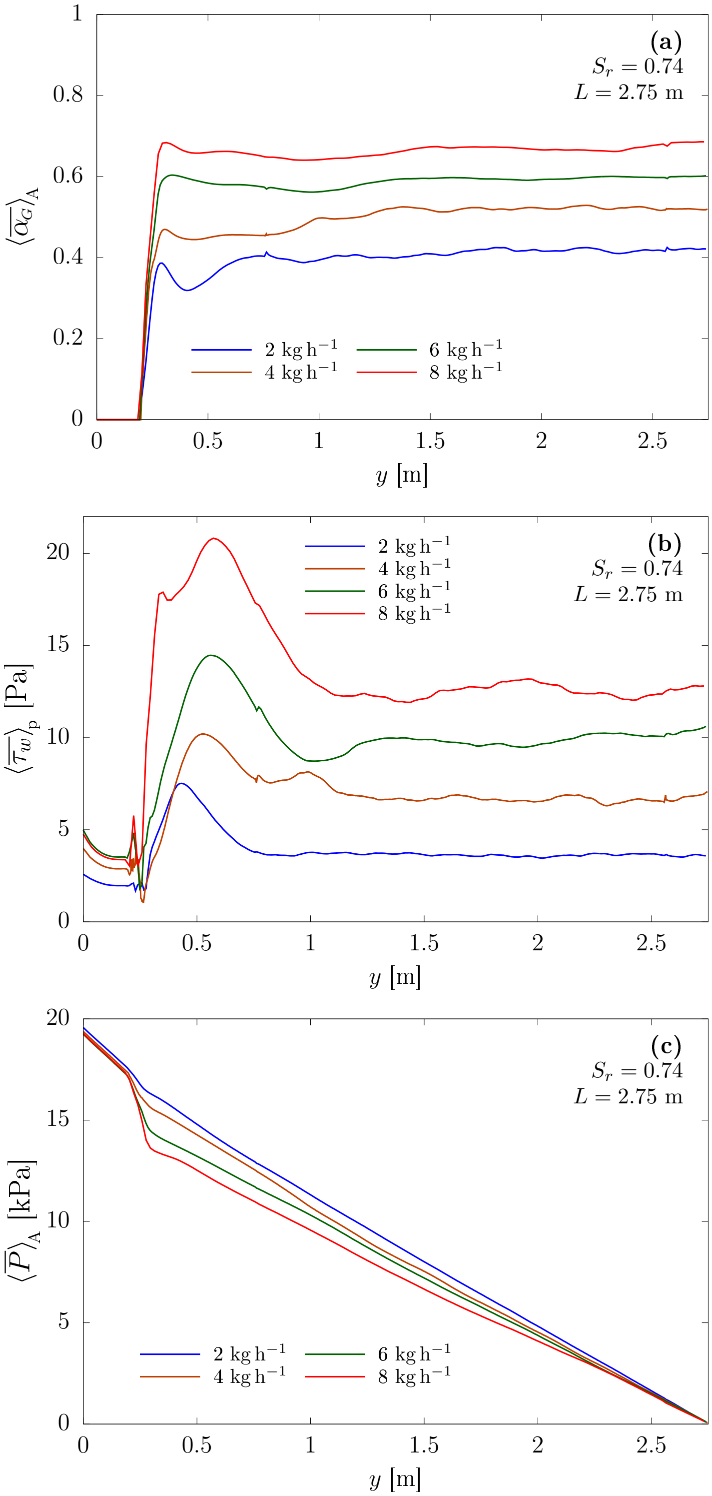

Figure 5.9: Time-average axial profiles for C2: (a) area-averaged void fraction, (b) perimeter-averaged wall shear stress, and (c) area-averaged pressure.

The wall shear stress curves (Figures 5.8(b) and 5.9(b)) have three distinct regions similar to the void fraction profile. Again, there is a sharp increase at the air injector region, a transitional region as the flow pattern develops, and a well-developed region where the curve is nearly horizontal. The recirculation occurring in the flow can lead to misleading values of time averages of wall shear stress. The peak magnitude may be greater in some locations but if negative wall shear stress occurs, the time-averaged value may be lower than a situation with no reverse flow. The observation of maximum wall shear in the region just above the air injector is consistent with the experimental findings of de Cachard and Delhaye [21].

The axial profiles of pressure (Figures 5.8(c) and 5.9(c)) highlight a unique characteristic of the airlift pump. For a constant length and submergence ratio all curves of $\dot{m}_G$ share the same start and end points because the pressure is enforced as a boundary condition. If the axial profile of pressure was plotted for two-phase flow in a vertical tube where the flow rate of both phases was specified, the pressure at the left-hand side (inlet boundary) would vary. The pressure curves begin with the same large slope in the single phase entrance region due to the hydrostatic pressure gradient of water before air is introduced. The curves of different $\dot{m}_G$ separate in a non-linear region just past the air injector. This region coincides with the spike in wall shear stress. In the well-developed region, the curves converge in an approximately linear path to the outlet pressure. As $\dot{m}_G$ increases, so does the void fraction, resulting in a lighter two-phase mixture. This is reflected by a shallower slope to the axial profile of pressure in the well-developed region. The axial profile of pressure seen in Figure 5.8(c) and 5.9(c) are consistent with the experimental findings of Moisidis and Kastrinakas [28]. They experimentally observed that as $\dot{m}_G$ increases, the pressure gradient decreases as void fraction increases. The separation between pressure profiles of different gas flow rates is the largest in the region just above the air injection where frictional pressure drop is the largest.

It is evident that the void fraction increases with an increase to $\dot{m}_G$. This trend is easily understood by considering the airlift pump performance curve. In the plateau region of the performance curve, the gas flow rate increases while the liquid flow rate remains constant, therefore the gas must occupy an increasing proportion of the volume. In the plateau region of the performance curve (region III), when the mean volume fraction increases, the airlift pump effectiveness decreases.

5.3.1 Effect of Airlift Parameters

Figures 5.10 and 5.11 show the same time-averaged axial profiles discussed above, but grouped by operation point instead of airlift configuration. Data for operating points of $\dot{m}_G = 2\ \mathrm{kg\,h^{-1}}$ and $\dot{m}_G = 8\ \mathrm{kg\,h^{-1}}$ are shown below and plots for the remaining operating points are included in Appendix C.2. The void fraction and wall shear stress are more sensitive to the submergence ratio than the riser length. This is consistent with the trend observed for the liquid discharge rate which is also more sensitive to submergence ratio than riser length.

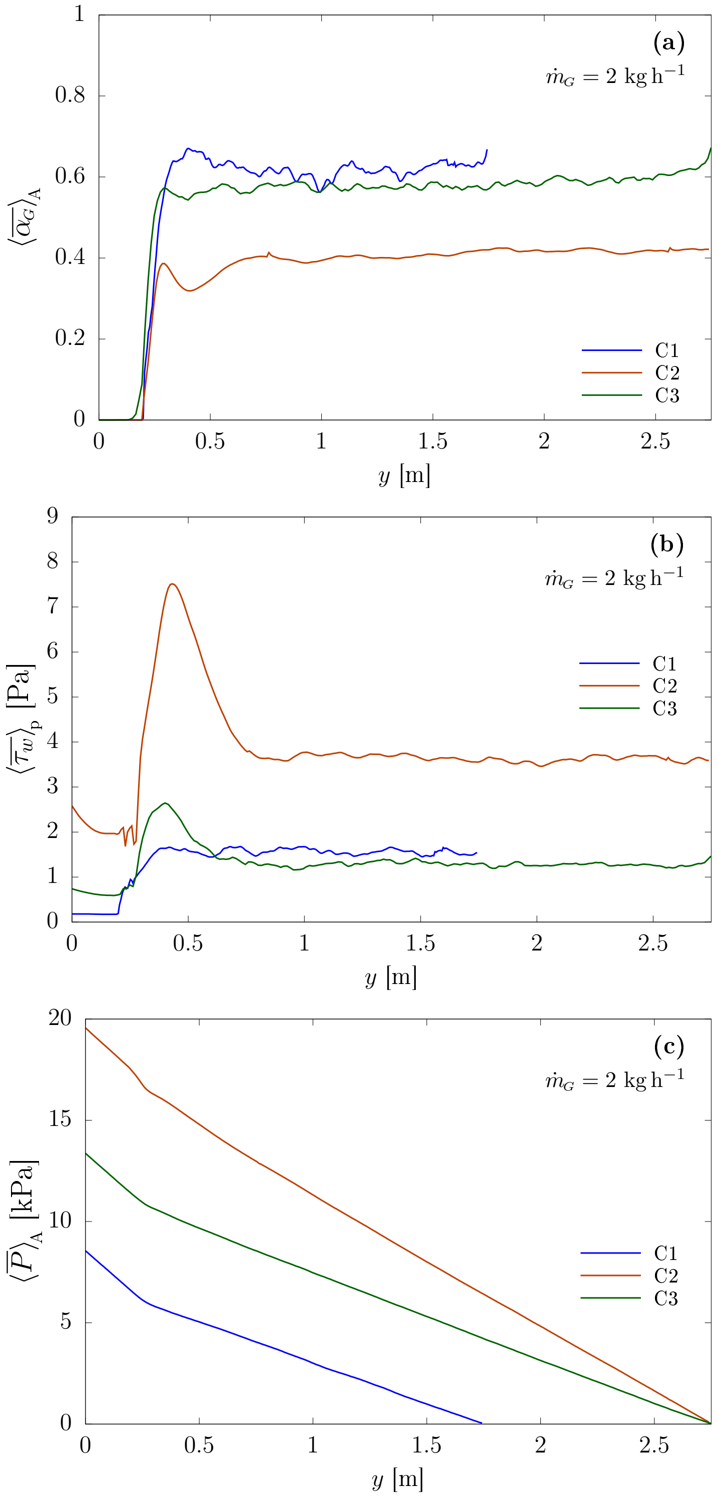

Figure 5.10: Time-average axial profiles for $\dot{m}_G = 2\ \mathrm{kg\,h^{-1}}$: (a) area-averaged void fraction, (b) perimeter-averaged wall shear stress, and (c) area-averaged pressure.

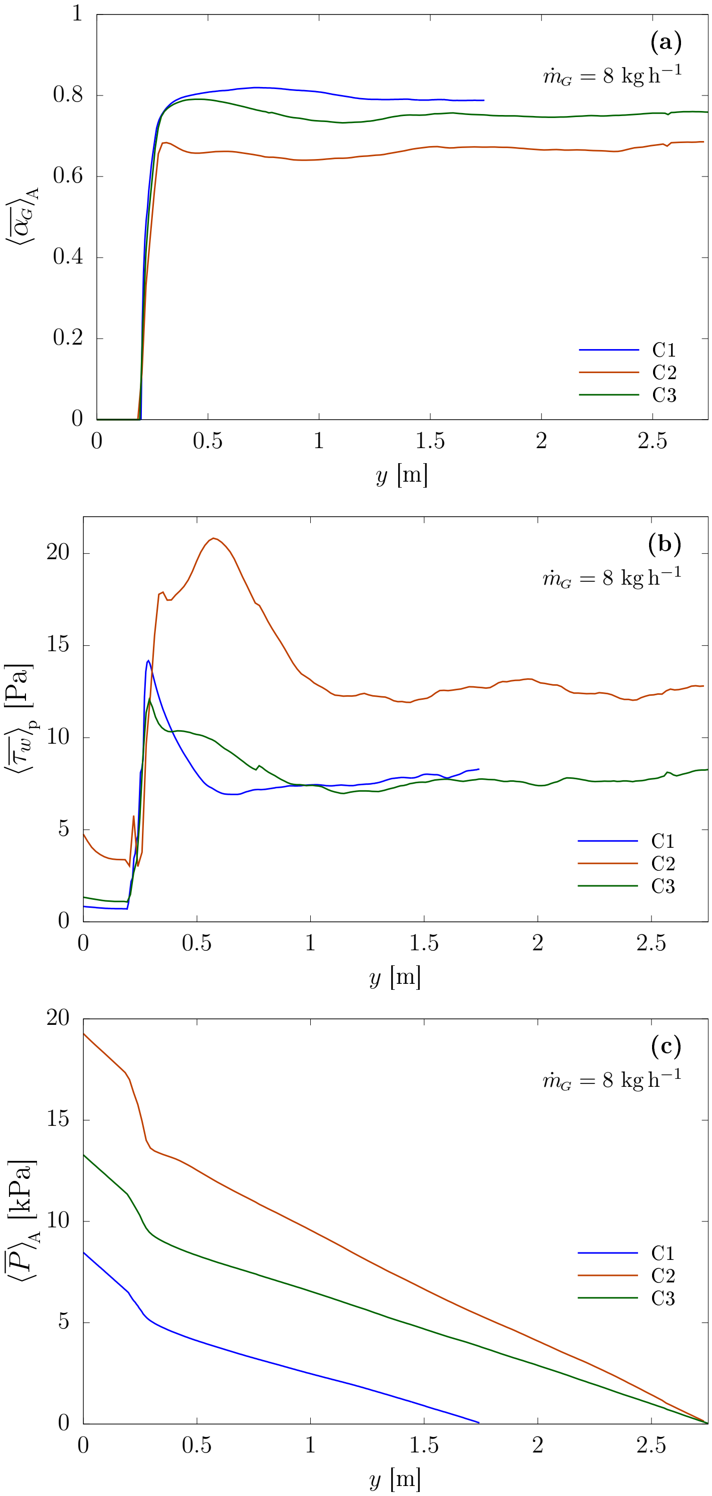

Figure 5.11: Time-average axial profiles for $\dot{m}_G = 8\ \mathrm{kg\,h^{-1}}$: (a) area-averaged void fraction, (b) perimeter-averaged wall shear stress, and (c) area-averaged pressure.

The wall shear stress increases with an increase to the submergence ratio because the total flow rate is also increasing. The void fraction decreases with an increase of the submergence ratio. The effect of submergence ratio on void fraction is consistent with the experimental findings of Tighzert *et al.* [29]. This trend is supported by considering the effect of submergence ratio on the P_{in} boundary condition. As the submergence ratio increases, the inlet pressure increases, thus the allowable static pressure gradient (inversely proportional to void fraction) increases.

The axial profiles of pressure show more separation than those of the void fraction and wall shear stress. The inlet pressure (value at left hand side of Figure 5.10(c)) is a function of L and S_r. The slopes of the pressure curves (Figures 5.10(c) and 5.11(c)) for C1 and C3 in the well-developed region are approximately equal because the void fraction is nearly equal.

5.4 Statistical Characteristics of the Flow

The PD distributions of void fraction, first described in Section 1.1.2, were used to examine the simulation results. In addition, the PD distribution of the liquid suction rate was also examined to help characterize the dynamic behaviour of the time signal.

The PDFs seen in Figure 5.12(a) all clearly indicate churn flow. The distribution of PD narrows and the peak shifts towards higher void fraction as gas flow rate increases. It is expected that the peak PD shifts to higher void fraction with increased gas flow rate because $\overline{\alpha}_G$ is increasing. The gradual narrowing of the PDF indicates a progressive transition towards annular flow. The same trend of void fraction PD narrowing and shifting to the right with increase to gas flow rate is observed for C2 and C3 shown in Figure 5.13(a) and C.5(a), respectively. Overall, the trend in the void fraction PDFs with increasing gas flow rate is consistent with the change in flow regime anticipated from the flow regime map.

There is a somewhat similar narrowing of the PD of the suction flow rate with increasing gas flow rate, as observed in Figures 5.12(b) and 5.13(b). The peak PD of the suction flow rate generally shifts to the right with increasing gas flow rate because the discharge rate usually increases. The C2m8 operating point is an exception to this rule, the liquid discharge rate decreased compared to the C2m6 operating point and the peak PD shifted to the left.

The shape of the void fraction PD distribution of the C2m2 operating point does not match either the ideal profile of slug, or churn flow; rather, it is a blend of the two. There are two peaks, but they are not well separated. The large area of PD between $\alpha_G = 0.15$ to 0.4 suggests that liquid slugs have become highly contaminated with smaller gas bubbles. The oscillation of the liquid suction rate is likely to contribute to the destabilization of slug flow. The C2m2, operating point lies near the slug-to-churn flow transition line of the Taitel *et al.* flow map.

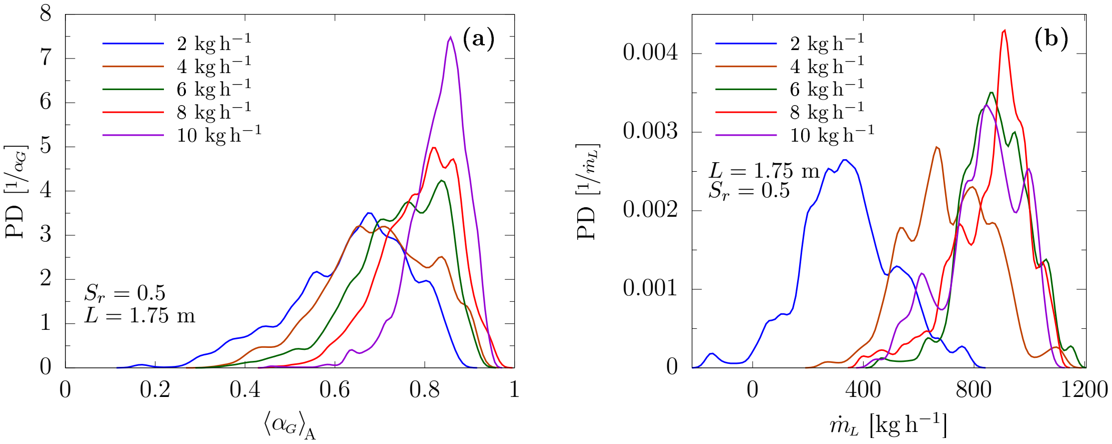

Figure 5.12: PD distributions of (a) void fraction and (b) suction flow rate for C1.

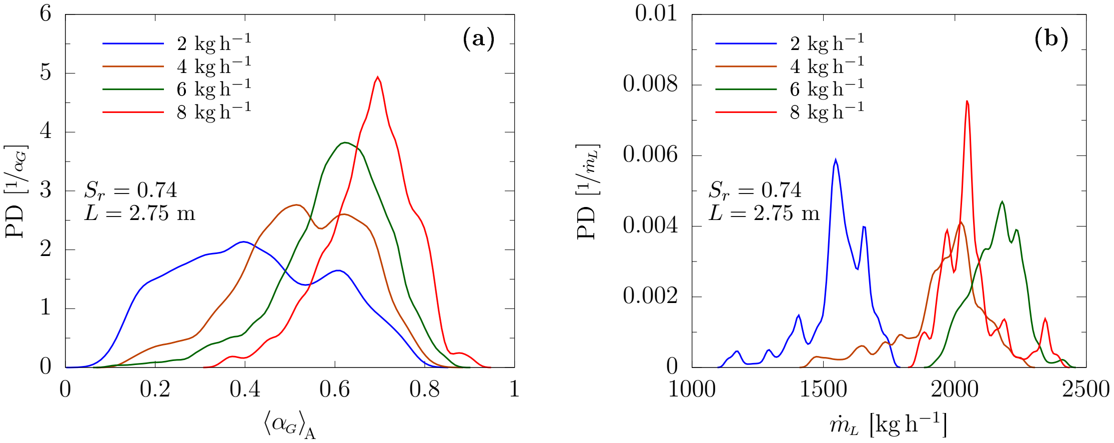

Figure 5.13: PD distributions of (a) void fraction and (b) suction flow rate for C2.

Instantaneous contour plots of the two-phase flow structures were studied to better visualize the reasons for the changes in PD distribution of void fraction discussed above. Figure 5.14 shows the three-dimensional structures of void distributions typical to low and high gas flow rates. At the low gas flow rate, the void fraction is clearly much lower than at the high gas flow rate, but how the void fraction is distributed is also different. The gas forms relatively large discrete pockets which are fairly regular and smooth in shape. The gas pockets observed in the CFD simulation do not meet the criteria to be considered Taylor bubbles which occur in slug flow. At the high gas flow rate, the gas occupies the core of the tube in a roughly continuous form. Small and irregular pockets of water travel upwards in the gas core. Large wave-like liquid structures detach from the liquid film at the wall of the tube. The interfacial structures described in Figure 5.14(b) are associated with churn flow.

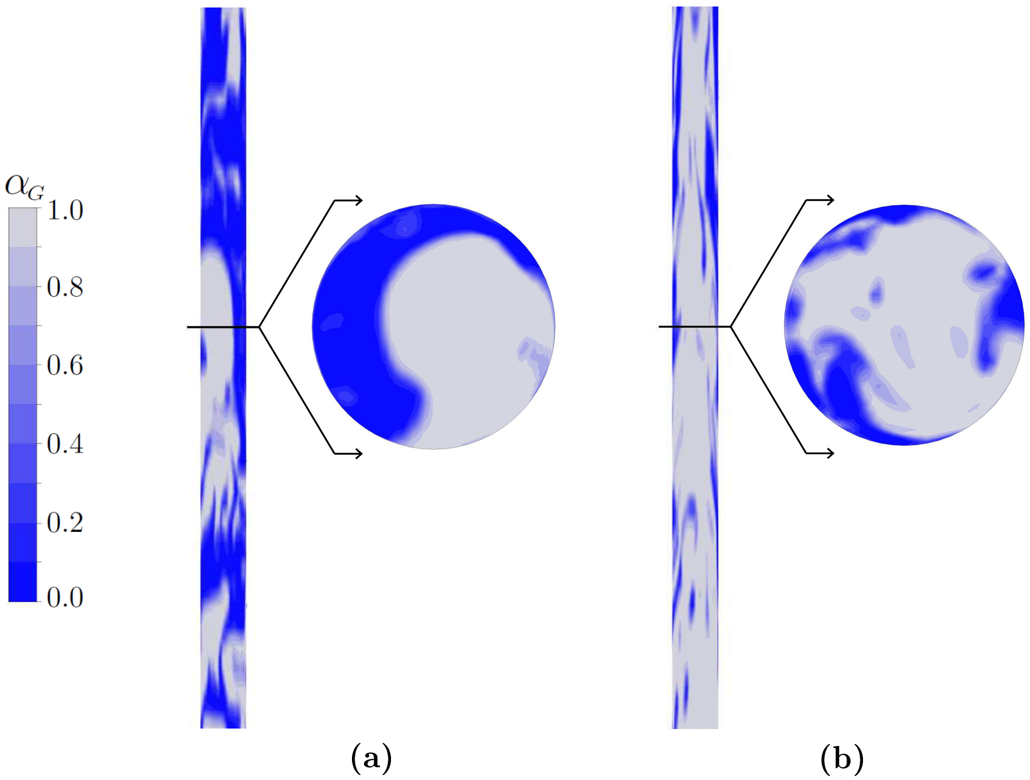

Figure 5.14: Change in typical interfacial structure size as a function of gas flow rate: (a) low: C2m2, and (b) high: C3m8.

The PD distributions of the two operating points shown in Figure 5.14 are rather intuitive. Imagine the flow is traveling upward through the measurement plane and the cross-sectional average of void fraction is reasonably approximated by the contour viewed from the side. For the C2m2 operating point, the void fraction as seen in Figure 5.14(a) is either large when a gas pocket is present, or near zero, hence the bimodal type distribution in Figure 5.13(a). For the C3m8 operating point, the void fraction as seen in Figure 5.14(b) looks roughly the same along the axial direction, which results in a narrower, single peaked distribution, as seen in Figure C.5(a). It should be emphasized, the two contour plots shown are just a snapshot in time, at another instance the flow will look different but the interfacial structures should have the same general qualities. The PDFs, however, are based on the entire simulation period and as such are a excellent indicator of the flow regime.

5.4.1 Effect of Airlift Parameters

Analogous to the examination of the axial profiles, the PDF data is regrouped to show the effect of submergence ratio and riser length for a given gas flow rate. Again, the submergence ratio has a more pronounced effect than the riser length because the mean void fraction and suction flow rate are more sensitive to the submergence ratio than the riser length. At higher gas flow rates ($\dot{m}_G \geq 6$ kg h^{-1}), the submergence ratio and riser length have a negligible affect on the shape of the PD distributions of void fraction and suction flow rate. At lower gas rates, however, greater deviation in the PD distributions is observed.

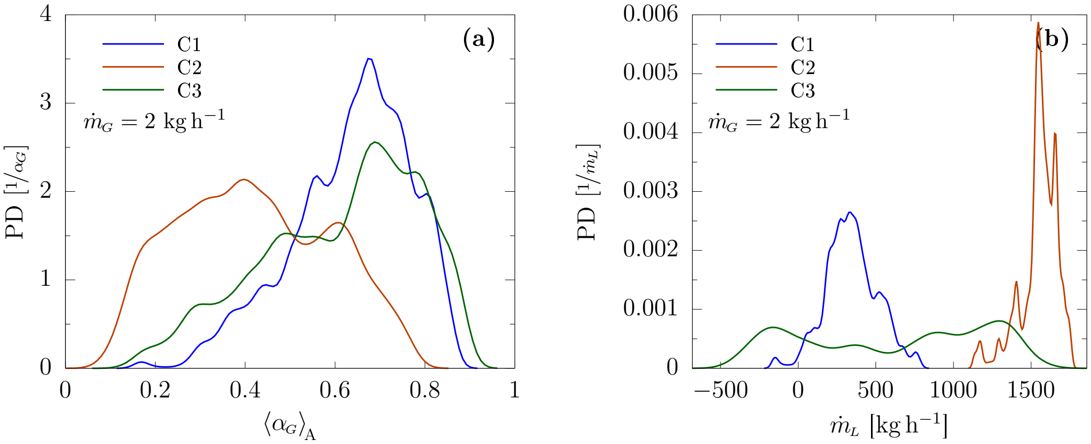

Figure 5.15: Effect of riser length and submergence ratio on PD distributions of (a) void fraction and (b) suction flow rate for $\dot{m}_G = 2$ kg h^{-1}.

The $\dot{m}_G = 2$ kg h^{-1} case is of particular interest because of the C3m2 operating point's instability. The C3m2 operating point falls within the slug flow region of the Taitel *et al.* [12] flow map, whereas the C2m2 point does not. The void fraction PDFs (Figure 5.15(a)), however, show more indications of slug flow for the C2m2 case than the C3m2 case. Figure 5.15(b) demonstrates the effect of airlift pump instability on the suction flow rate, the C2m2 case has a very narrow width of suction flow rates compared to C1m2 or C3m2. It could be argued that the wide variation in liquid flow rate impedes the development of orderly slug flow. The boundary inlet conditions of the C2m2 case are much closer to the conditions in which flow maps are developed and therefore it has better agreement. As $\dot{m}_G$ increases, the shape of the PD distribution of the C2 configuration changes to more closely resemble the C1 and C3 configurations, as demonstrated in Figures 5.16 and 5.17.

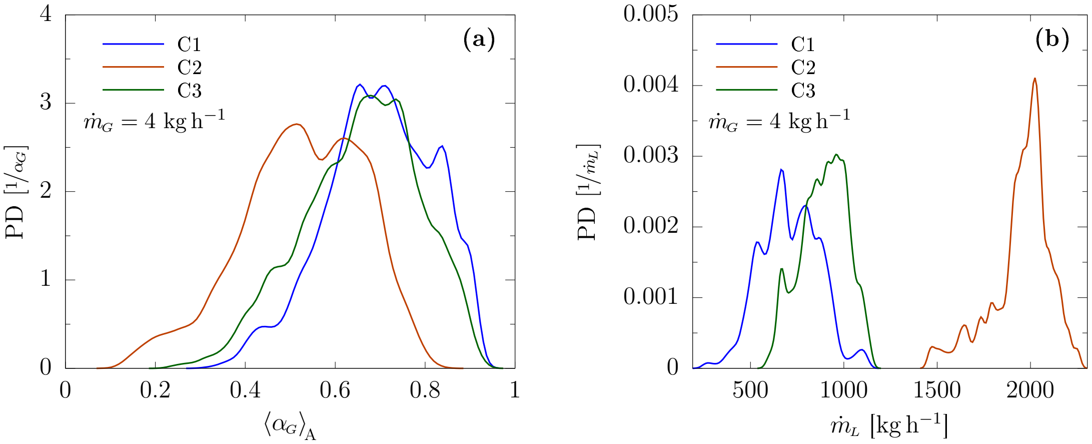

Figure 5.16: Effect of riser length and submergence ratio on PD distributions of (a) void fraction and (b) suction flow rate for $\dot{m}_G = 4 \text{ kg h}^{-1}$.

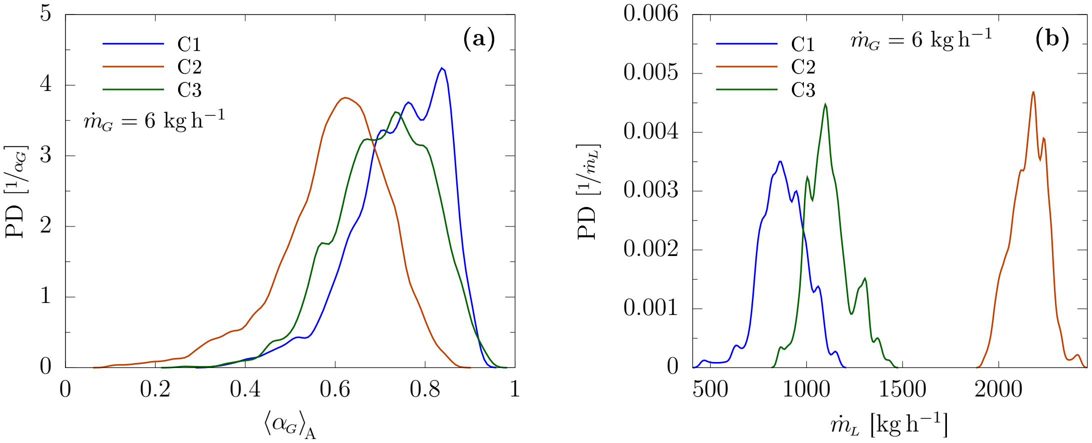

Figure 5.17: Effect of riser length and submergence ratio on PD distributions of (a) void fraction and (b) suction flow rate for $\dot{m}_G = 6 \text{ kg h}^{-1}$.

To put the variation of suction flow rate into context, a flow map is drawn showing the mean value and the range of suction flow rates observed. The widest range of suction flow rates is observed at operation points near the predicted slug churn transition line. In the case of C3m2, the range crosses the transition line occupying both slug and churn flow, as indicated in Figure 5.18. Both the wide range of suction flow rate and the crossing the regime transition line are consistent with the observation of intermittent regions of both slug and churn flow, as discussed in Section 5.2.1. The observation of local instantaneous flow structures is supported by the measurement of integral parameters, and vice versa.

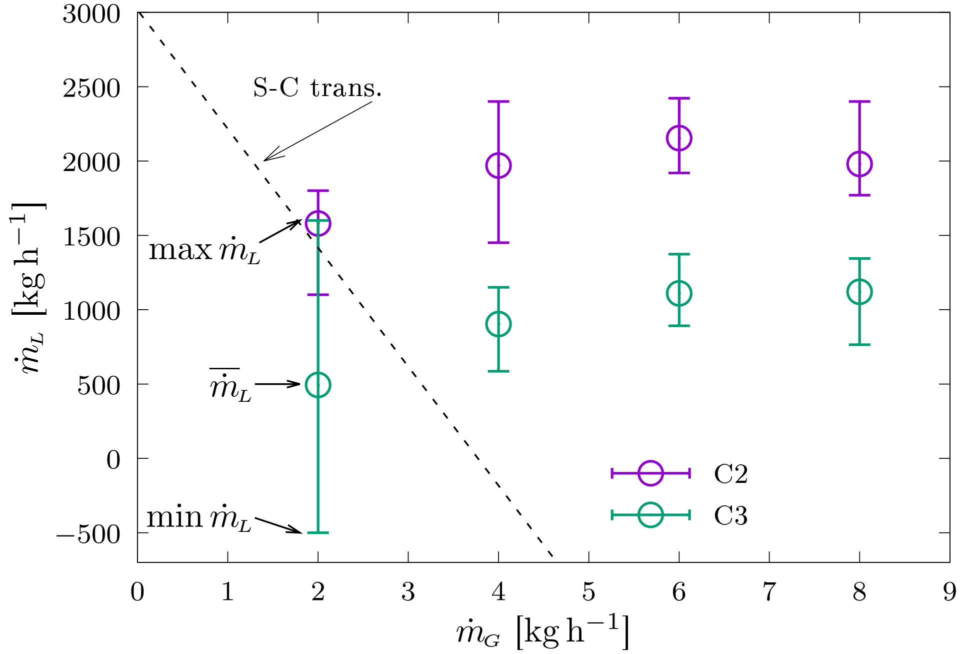

Figure 5.18: Discharge flow rate and range of suction flow rate.

5.5 Comparison of Temporal-Spatial-Averaged Results

The temporal-spatial-average of relevant quantities was calculated to facilitate comparison between the CFD model and terms in the steady-state algebraic model. The value of each one of the terms ($\Pi_{\Delta P}$, Π_{weight}, and Π_{fric}) in the force balance was extracted from the CFD results. The balance of these time-averaged forces was calculated and the imbalance was found to be $< 1\%$ with respect to ΔP. Provided the simulation is numerically well converged, the forces must balance at every instance (time step) but this includes transient storage terms.

By definition, transient storage terms are zero in a steady-state model. The fact that the steady-state force imbalance computed from the CFD simulation over the pseudo-steady operation period (same period used to calculate the liquid discharge rate) is small implies the summation transient terms have trended towards zero and the averaging period indeed represents the pseudo-steady operation.

5.5.1 Comparison of Riser Pipe Force Balance Components

It is of interest to examine the relative magnitude of the terms in the steady-state force balance. The consensus in the literature is that the gravitational loss (Π_{weight}) is the dominant force and the acceleration loss ($\Pi_{\Delta\text{mom}}$) and frictional pressure drop (Π_{fric}) are secondary. This has not been verified extensively, nor has the effects of submergence ratio, riser length, or gas flow rate on the proportion of the losses been examined. Figure 5.19 shows the relative magnitude of the losses for twelve of the simulated operating points.

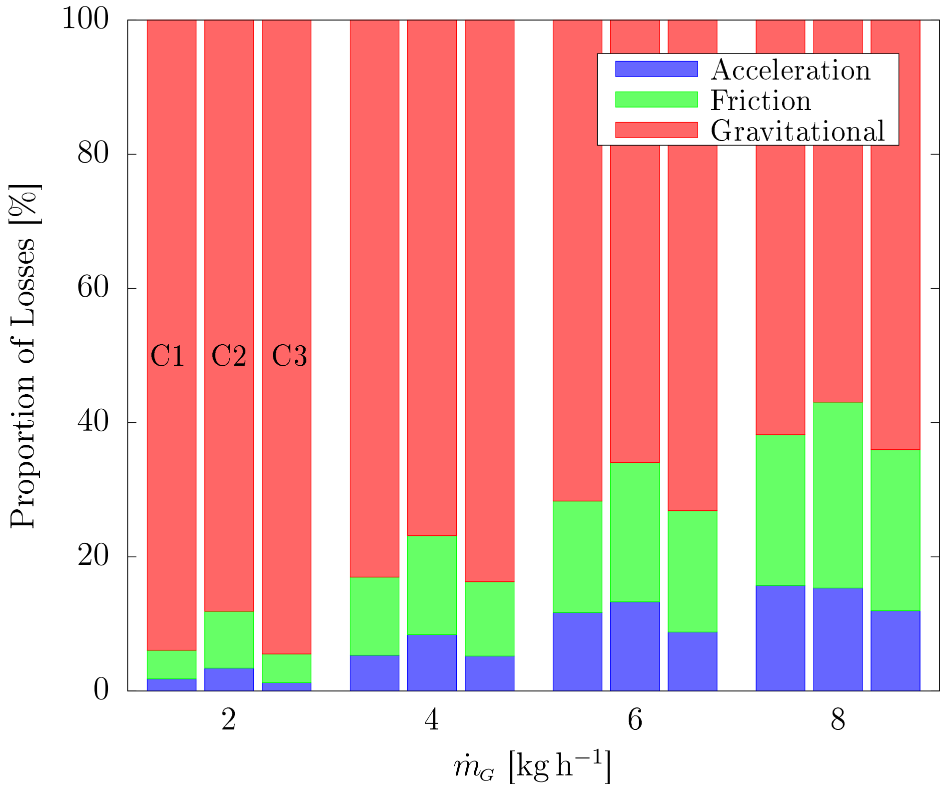

Figure 5.19: Relative magnitude of losses from CFD.

The contributions of the momentum flux and wall shear stress to the total losses increases with increasing $\dot{m}_G$. The weight is inversely related to α_G which increases with $\dot{m}_G$. These trends are consistent with the increase in total flow rate associated with the increase in $\dot{m}_G$.

The airlift configuration also has an effect on the proportion of terms. The weight represents 5 to 9% more of the total losses in C2 (larger submergence ratio) than in C1 or C3 (smaller submergence ratio). The change in submergence ratio has a larger effect on the relative magnitude of forces than the change in riser length, which is consistent with the trend observed when considering liquid discharge rate.

The relative magnitude of each of the three losses can be calculated from the SS model. The length and submergence ratio have the same affect on the proportion of losses in the steady state model (Figure C.7) as observed with the CFD data (Figure 5.19). To make a more clear comparison, the data from the CFD model and steady state model are plotted side by side for a single airlift configuration. Figure 5.20 shows the comparison for C1, and the remaining two configurations are included in appendix C.4.

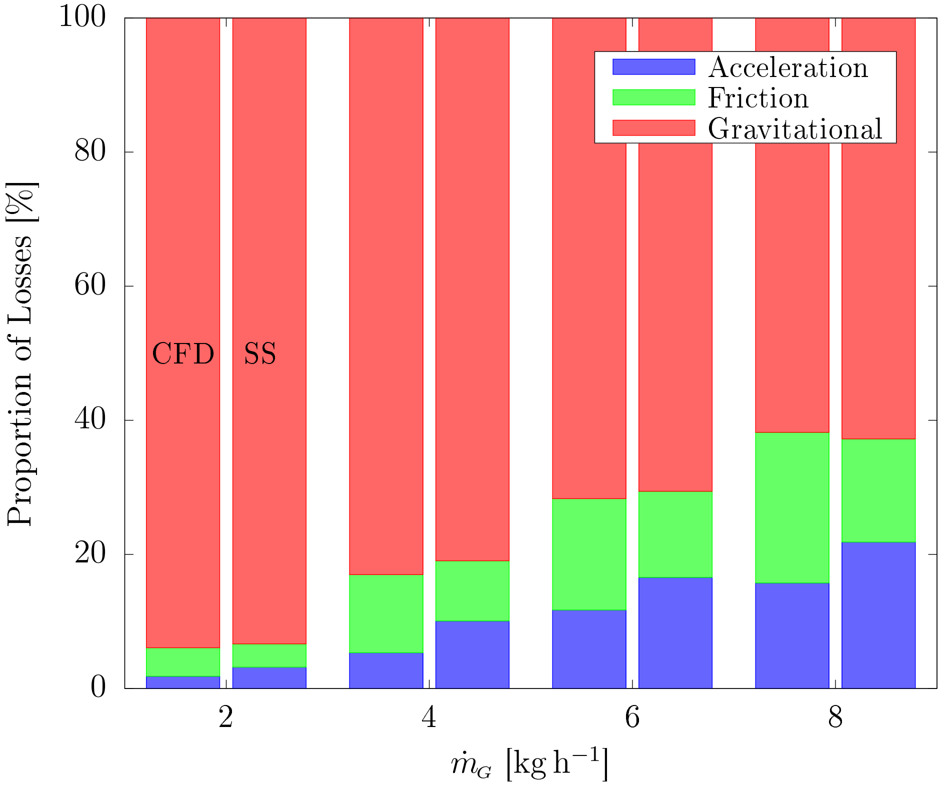

Figure 5.20: Comparison of the relative magnitude of losses between the CFD model and steady-state model of Kassab *et al.* [25] for C1.

The relative magnitude of the weight term is practically the same in the CFD model and the steady-state (SS) model. The momentum term increases and the frictional pressure drop term decrease from the CFD model to the steady-state model. The deviation between models increases with increasing gas flow rate. At its largest, the difference is approximately 7%.

It has been suggested by a number of theoretical and experimental works that the acceleration losses of the flow in an airlift pump represent $< 1\%$ of the total losses [17, 20, 21].

Clark and Dabolt [17] justified the use of a very rough approximation of the frictional losses in their steady-state model on the grounds that the frictional losses only represent 2 to 10% of the total losses. Based on the present modelling, the weight does represents the majority of the losses, but the relative magnitude of the frictional pressure drop and momentum differential are larger than the typical range found in the literature. The prediction of the momentum differential and frictional pressure drop are often seen as a lesser importance in the steady-state model; however based on the present results, they merit equal consideration to that of the void fraction.

5.5.2 Comparison Against Published Correlations

As previously stated in Section 2.1.2, accurate prediction of the liquid discharge rate in a SS model relies on accurate prediction of the void fraction and frictional pressure drop by use of correlations. Such correlations have been extensively tested against standard two-phase flow data in the literature, but they have not been compared against measurements from an airlift pump.

To make an fair comparison between the CFD and values predicted by correlation, the average void fraction and wall shear stress was computed over the riser pipe of the computational domain. The entrance pipe and injector region were excluded to prevent skewing of the average values because they are single phase and mixing regions, respectively.The conditions of the airlift pump riser still vary to some degree from the conditions the correlations were developed for. Specifically, the correlations are typically fitted to measurements taken from well-developed flow with $^{L}/_{D} > 100$ and the flow rates of both phases are controlled.

The correlations for void fraction previously described in Section 2.1.2 are used for comparison. For frictional pressure drop, popular correlations recommended from recent reviews (Xu *et al.* [97], Ghajar and Bhagwat [98], and Thome and Cioncolini [99]) were selected in addition to the methods used in the steady-state airlift pump models. Details of the specific correlations used can be found in Appendix B.

The predicted void fraction and wall shear stress was calculated using the the flow rates recorded from the CFD simulation. Where required, the air density was taken to be the average between atmospheric and the value at the air injector. For the comparison made in Figure 5.21, the predicted value was divided by the value measured from the CFD results. The data from C3 can be found in Appendix C.4 as it is similar to that of C1 and C2.

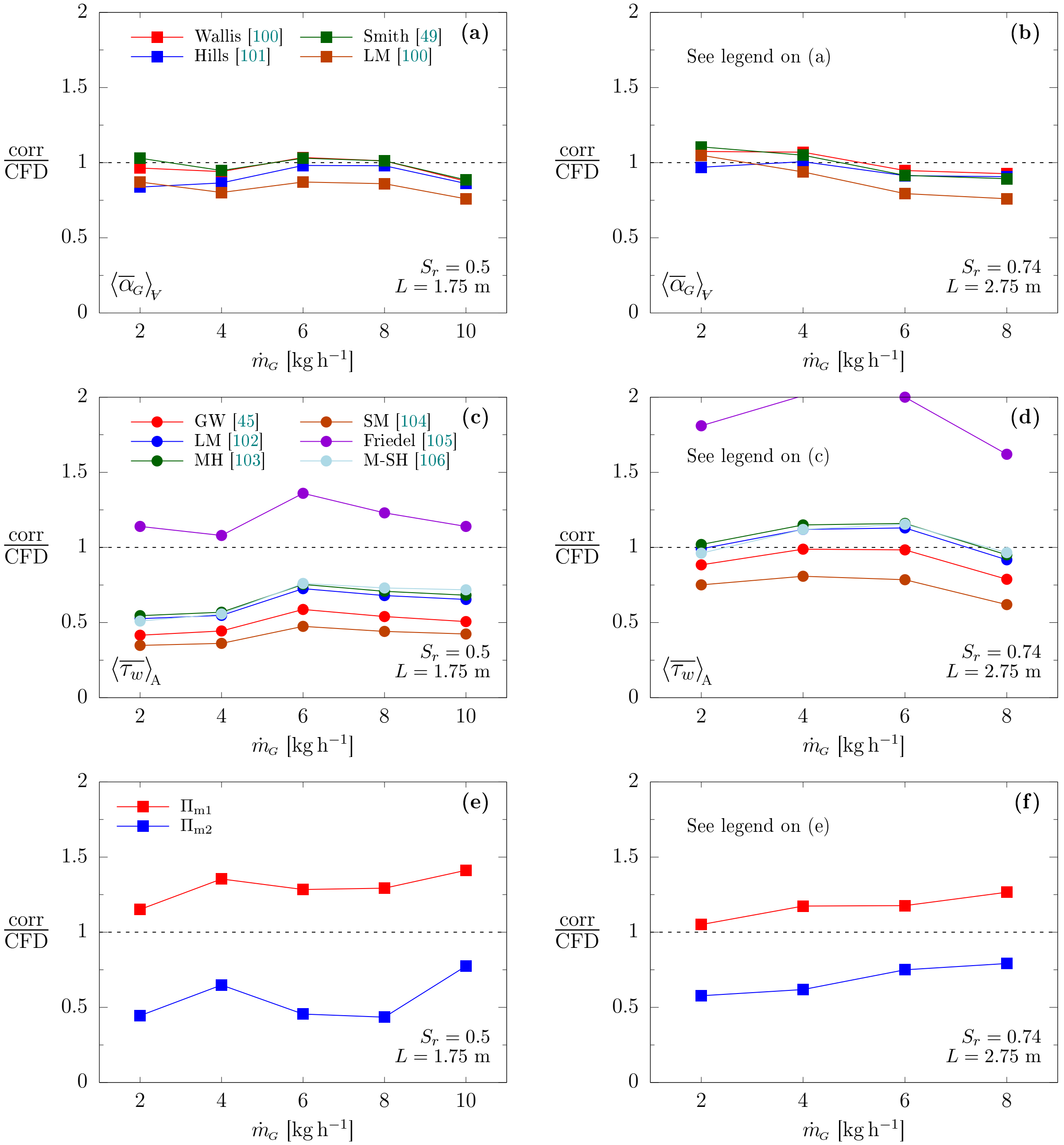

Figure 5.21: Comparison of values predicted by correlation to measurements from CFD simulation. (a) C1 void fraction, (b) C2 void fraction, (c) C1 frictional pressure drop, (d) C2 frictional pressure drop, (e) C1 momentum differential, and (f) C2 momentum differential.

The agreement between correlations and CFD results is generally much better for void fraction than wall shear stress. Regarding the void fraction, the agreement is roughly the same for all three airlift configurations and gas flow rates. Typically, the correlations error on the side of underpredicting the void fraction relative to the CFD. Overall, the Wallis [100] and Smith [49] correlations give the best prediction with a mean disagreement of approximately 6%. The drift flux model is a well established method for predicting the void fraction in a wide range of flows.

In general, the agreement of wall shear stress values is approximately 10% better for C2 and C3 than C1. This can be attributed to the longer riser length. The wall shear stress is higher in the developing region than in the well-developed region of the two-phase flow. The longer the pipe, the smaller the entrance length is relative to the total length and the less it skews the average wall shear stress in the well developed region. This argument is supported by the upward shift of all curves between Figures 5.21(c) and (d). The MH [103] and M-SH [106] correlations have the smallest disagreement with the CFD at approximately 18%. The underprediction of the wall shear stress by the Griffith and Wallace [45] correlation is consistent with the findings of Stenning and Martin [15] and Parker [18], who found that a larger value of friction factor was needed to better predict airlift pump performance with their SS models.

The two methods of approximating the momentum differential in the steady-state models (Π_{m1}, Eq. (2.9) and Π_{m2}, Eq. (2.10)) can be compared against the momentum flux calculated from the CFD solution. Because the mixture density and velocity is known in every control volume, the integral (Eq. (2.6)) can be properly evaluated to calculate the momentum flux of the CFD solution. The momentum differential from the CFD solution is calculated between the bottom of the air injector and the top of the riser. The steady-state (time-averaged) momentum flux is calculated by averaging the instantaneous momentum flux at every time step; this is not equivalent to calculating the integral from the time-averaged solution fields. The Π_{m1} formulation consistently overpredicts the momentum flux, whereas Π_{m2} underpredicts. The momentum flux is closer to the Π_{m1} approximation at low gas flow rates and gradually shifts towards Π_{m2} at higher gas flow rates. Some form of interpolation between the Π_{m1} and Π_{m1} formulations could give a more accurate prediction of the momentum flux for use in the steady-state model. This would be step towards improving the accuracy of the steady state model because momentum differential represents a significant portion of the total losses, as demonstrated in Section 5.5.1.

5.6 Recommendations for Future Work

A limitation of the homogeneous VOF based model is the model's inability to resolve interfacial structures less than several control volumes in size. These small length scales are likely to occur in the two-phase flow of the airlift pump and are omitted by the present CFD model. There are hybrid modeling approaches (discussed in Appendix A.2.3) that combine the interface capturing of VOF for large interfacial length scales with the multi-fluid modeling of small interfacial length scales. As mentioned in Appendix A.2.5, the hybrid approaches such as 'Multi-fluid VOF' in ANSYS Fluent have shown promising results in capturing a wider range of two-phase flow structures. The added versatility of the hybrid approach makes it well suited for the complex flow in the airlift pump, especially in cases where more details of the air injection system were modeled.

The modeling of turbulence is a major uncertainty in the modeling of churn flow [87]. The sensitivity study presented in Section 4.8 demonstrated that the choice between the $k-\varepsilon$ and the SST models was not particularly significant, but does not imply either is physically accurate. Improvements to the modeling of turbulence in two-phase flows is well outside the scope of this work and the study of the airlift pump.

As discussed in Section 5.1.1, the assumptions and simplifications made in developing the CFD model of the airlift pump are likely to contribute to the overprediction of the liquid discharge rate. Furthermore, the simplification of the liquid and gas supply systems affect the stability of the airlift pump system, as mentioned in Section 5.2.1. Expanding the computational domain to include more details of the gas and liquid supply could improve the accuracy of the CFD model with respect to the experiments. These modifications, however, would lead to a significant increase in computing time. Additionally, the details of the geometry of the gas and liquid supply systems are often not well documented.

Chapter 6

Summary and Conclusions

The objectives of this thesis outlined in Section 1.2 have been accomplished. To emphasizes this, the activities in the present work are first summarized, then the key finding are highlighted.

6.1 Summary

The commercial CFD code ANSYS CFX was used to simulate the two-phase flow in the riser pipe of an airlift pump. A time-dependent homogeneous volume-of-fluid model was used. It was assumed that there was no heat or mass transfer present in the flow. The working fluids were standard property water and air modeled as an ideal gas.

The computational domain consisted of a vertical pipe where liquid entered the bottom and the two-phase mixture exited the top of the pipe. The geometry of the air injection apparatus was simplified by eliminating its internal structures from the domain. The boundary conditions of the model were specified such that the liquid flow rate was an implicit result of the simulation, thus the airlift pump performance was predicted by the simulation. The assumptions made in the formation of the computational domain neglected losses in the gas and liquid feed systems meant the CFD simulations represented an idealized case of the airlift pump.

The CFD model was used to simulate select cases from the experiments of Kassab *et al.* [25]. Three airlift pump configurations consisting of two riser lengths and two submergence ratios were considered. In total 13 operating points were simulated with gas flow rates ranging from 2 to 10 $\mathrm{kg\,h^{-1}}$.

A mesh independence study was performed, which included four different grid densities and examined the potential use of axisymmetry. The sensitivity of the CFD model to the choice of turbulence model was examined using the $k-\varepsilon$ and the SST turbulence models. A methodology was established for determining the liquid discharge rate and the uncertainty in the average value.

The CFD results were compared against the experimentally measured liquid discharge rate by Kassab *et al.* [25] and the flow regime predicted by the flow map of Taitel *et al.* [12]. The behaviour of the two-phase flow was examined qualitatively using contour plots and other images from the simulation. The statistical characteristics of the two-phase flow was examined using the PD distribution of void fraction and suction flow rate. Average flow quantities were also examined; in particular, the axial profile of time-averaged values and time-volume-averages. The effects of gas flow rate, riser length, and submergence ratio on the two-phase flow structures were highlighted using the aforementioned tools of analysis.

6.2 Conclusions

Key findings of this work are:

- A complete 3-D computational domain is required for physically realistic simulation results.
- The liquid discharge rate and two-phase flow structures predicted by simulation results were insensitive to the choice of turbulence model. There is no evidence to justify the use of the SST turbulence model given the significant increase in computing time.
- The CFD simulations predicted the overall behaviour of the performance curve. The liquid discharge rate was over predicted by approximately 25 to 30%. The CFD model gives a similar prediction to the steady-state model. This behaviour is consistent with both the CFD and SS models representing an idealized airlift pump.

- Churn flow was the predominant flow regime observed in the CFD simulations. This finding is consistent with experiments.
- Airlift pump instability was observed at the C3m2 operating point. During unstable operation, a relationship was observed in the low frequency large amplitude oscillation in the suction flow rate, riser volume fraction, and eduction flow rate.
- The effects of riser length, submergence ratio, and gas flow rate on the two-phase flow in the airlift pump are summarized as follows:
  - For an increase in gas flow rate:
    - Void fraction and wall shear stress increases.
    - Time-dependent fluctuation in liquid suction flow rate decreases.
  - For an increase in riser length:
    - There is a negligible effect on void fraction.
    - Wall shear stress decreases
    - Fluctuation in liquid suction rate increases
  - For and increase in submergence ratio:
    - Void fraction decreases.
    - Wall shear stress increases.
    - Fluctuation in liquid suction flow rate decreases.
- The weight of the two-phase mixture is the dominant force but frictional and acceleration losses make a larger contribution to the system than previously suggested by others.
- Accurate prediction of wall shear is the primary shortcoming for simple SS models. This is due to the time-variation in the suction flow rate inherent to an airlift pump, and the relatively short riser pipe used in the present study.

References

[1] P. Hanafizadeh, B. Ghorbani, Review study on airlift pumping systems, Multiphase Science and Technology 24 (4) (2012) 323–362. doi:10.1615/MultScienTechn.v24.i4.30.

[2] S. Bukhari, Improving the airlift pump prediction model for aquaculture applications, Master's thesis, Guelph (2018).

[3] D. Reinemann, A Theoretical and Experimental study of Airlift Pumping and Aeration with Reference to Aquacultural Applications, Ph.D. thesis, Cornell (1987).

[4] N. Parker, M. Suttle, Design of airlift pumps for water circulation and aeration in aquaculture, Aquacultural Engineering 6 (2) (1987) 97–110. doi:10.1016/0144-8609(87)90008-2.

[5] D. Reinemann, M. Timmons, Prediction of oxygen-transfer and total dissolved-gas pressure in airlift pumping, Aquacultural Engineering 8 (1) (1989) 29–46. doi:10.1016/0144-8609(89)90019-8.

[6] Ramdhani, Indarto, Deendarlianto, I. Catrawedarma, Experimental study on the effect of submergence ratio and air flow rate on the characteristics of liquid-gas-solid three-phase airlift pump, in: THERMOFLUID X: 10th International Conference on Thermofluids 2019, AIP Publishing, 2020. doi:10.1063/5.0018740.

[7] S. Kassab, H. Kandil, H. Warda, W. Ahmed, Experimental and analytical investigations of airlift pumps operating in three-phase flow, Chemical Engineering Journal 131 (1-3) (2007) 273–281. doi:10.1016/j.cej.2006.12.009.

[8] D. J. Nicklin, The airlift pump: Theory and optimization, Transactions of Institution of Chemical Engineers (1963).

[9] M. Ishii, T. Hibiki, Thermo-Fluid Dynamics of Two-Phase Flow, Springer US, 2006. doi:10.1007/978-0-387-29187-1.

[10] S. Rouhani, M. Sohal, Two-phase flow patterns: A review of research results, Progress in Nuclear Energy 11 (3) (1983) 219–259. doi:10.1016/0149-1970(83)90012-4.

[11] B. Wu, M. Firouzi, T. E. Rufford, B. Towler, Characteristics of counter-current gas-liquid two-phase flow and its limitations in vertical annuli, Experimental Thermal and Fluid Science 109 (2019) 109899. doi:10.1016/j.expthermflusci.2019.109899.

[12] Y. Taitel, D. Bornea, A. E. Dukler, Modelling flow pattern transitions for steady upward gas-liquid flow in vertical tubes, AIChE Journal 26 (3) (1980) 345–354. doi:10.1002/aic.690260304.

[13] K. Mishima, M. Ishii, Flow regime transition criteria for upward two-phase flow in vertical tubes, International Journal of Heat and Mass Transfer 27 (5) (1984) 723–737. doi:10.1016/0017-9310(84)90142-x.

[14] G. Hewitt, D. Roberts, Studies of two-phase flow patterns by simultaneous x-ray and flash photography, Tech. rep., Atomic Energy Research Establishment, Harwell, England (United Kingdom) (1969).

[15] A. H. Stenning, C. B. Martin, An analytical and experimental study of air-lift pump performance, Journal of Engineering for Gas Turbines and Power 90 (2) (1968) 106. doi:10.1115/1.3609143.

[16] I. Todoroki, Y. Sato, T. Honda, Performance of air-lift pump, Bulletin of JSME 16 (94) (1973) 733–741. doi:10.1299/jsme1958.16.733.

[17] N. N. Clark, R. J. Dabolt, A general design equation for air lift pumps operating in slug flow, AIChE Journal 32 (1) (1986) 56–64. doi:10.1002/aic.690320107.

[18] G. Parker, The effect of footpiece design on the performance of a small air lift pump, International Journal of Heat and Fluid Flow 2 (4) (1980) 245–252. doi:10.1016/0142-727x(80)90018-1.

[19] D. Kouremenos, J. Staïcos, Performance of a small air-lift pump, International Journal of Heat and Fluid Flow 6 (3) (1985) 217–222. doi:10.1016/0142-727x(85)90016-5.

[20] D. Reinemann, J. Parlange, M. Timmons, Theory of small-diameter airlift pumps, International Journal of Multiphase Flow 16 (1) (1990) 113–122. doi:10.1016/0301-9322(90)90042-h.

[21] F. de Cachard, J. Delhaye, A slug-churn flow model for small-diameter airlift pumps, International Journal of Multiphase Flow 22 (4) (1996) 627–649. doi:10.1016/0301-9322(96)00003-1.

[22] M. Khalil, K. Elshorbagy, S. Kassab, R. Fahmy, Effect of air injection method on the performance of an air lift pump, International Journal of Heat and Fluid Flow 20 (6) (1999) 598–604. doi:10.1016/s0142-727x(99)00051-x.

[23] F. Lawniczak, P. Francois, O. Scrivener, E. G. Kastrinakis, S. G. Nychas, The efficiency of short airlift pumps operating at low submergence ratios, The Canadian Journal of Chemical Engineering 77 (1) (1999) 3–10. doi:10.1002/cjce.5450770103.

[24] W. E. Castro, P. B. Zielinski, P. A. Sandifer, Performance characteristics of air lift pumps of short length and small diameter, Proceedings of the annual meeting - World Mariculture Society 6 (1-4) (2009) 451–461. doi:10.1111/j.1749-7345.1975.tb00039.x.

[25] S. Z. Kassab, H. A. Kandil, H. A. Warda, W. H. Ahmed, Air-lift pumps characteristics under two-phase flow conditions, International Journal of Heat and Fluid Flow 30 (1) (2009) 88–98. doi:10.1016/j.ijheatfluidflow.2008.09.002.

[26] S. Kassab, H. Kandil, H. Warda, W. A. Z. Kassab, H. A. Kandil, H. A. Warda, W. H. Ahmed, Performance of an airlift pump operating in two-phase flow, 2001.

[27] C. T. Moisidis, E. G. Kastrinakis, Two-phase flow pattern transitions of short airlift pumps, Journal of Hydraulic Research 48 (5) (2010) 680–685. doi:10.1080/00221686.2010.515382.

[28] C. T. Moisidis, E. G. Kastrinakis, Pressure behaviour in riser tube of a short airlift pump, Journal of Hydraulic Research 48 (1) (2010) 65–73. doi:10.1080/00221680903568642.

[29] H. Tighzert, M. Brahimi, N. Kechroud, F. Benabbas, Effect of submergence ratio on the liquid phase velocity, efficiency and void fraction in an air-lift pump, Journal of Petroleum Science and Engineering 110 (2013) 155–161. doi:10.1016/j.petrol.2013.08.047.

[30] P. Hanafizadeh, S. Ghanbarzadeh, M. H. Saidi, Exergy analysis of airlift systems: experimental approach, International Journal of Exergy 8 (4) (2011) 407. doi:10.1504/ijex.2011.041030.

[31] P. Hanafizadeh, A. H. Raffiee, M. H. Saidi, Experimental investigation of characteristic curve for gas-lift pump, Journal of Petroleum Science and Engineering 116 (2014) 19–27. doi:10.1016/j.petrol.2014.02.011.

[32] S. H. Kim, C. H. Sohn, J. Y. Hwang, Effects of tube diameter and submergence ratio on bubble pattern and performance of air-lift pump, International Journal of Multiphase Flow 58 (2014) 195–204. doi:10.1016/j.ijmultiphaseflow.2013.09.007.

[33] W. Ahmed, A. Aman, H. Badr, A. Al-Qutub, Air injection methods: The key to a better performance of airlift pumps, Experimental Thermal and Fluid Science 70 (2016) 354–365. doi:10.1016/j.expthermflusci.2015.09.022.

[34] H. M. Badr, W. H. Ahmed (2012).

[35] F. S. Abou Taleb, J. A. Al-jarrah, Experimental study of an air lift pump, Engineering, Technology, & Applied Science Research 7 (3) (2017) 1676–1680. doi:10.48084/etasr.1207.

[36] M. Shallouf, Numerical simulation of airlift pumps operating under two-phase flow conditions for aquaculture systems, Master's thesis, Guelph (2019).

[37] Z. Wang, Y. Kang, D. Li, X. chuan Wang, D. Hu, Investigating the hydrodynamics of airlift pumps by wavelet packet transform and the recurrence plot, Experimental Thermal and Fluid Science 92 (2018) 56–68. doi:10.1016/j.expthermflusci.2017.11.006.

[38] Z. Wang, Y. Kang, X. Wang, S. Wu, X. Li, Investigation of the hydrodynamics of slug flow in airlift pumps, Chinese Journal of Chemical Engineering 26 (12) (2018) 2391–2402. doi:10.1016/j.cjche.2018.04.015.

[39] Z. Wang, Y. Kang, X. Wang, D. Li, D. Hu, Investigating the flow characteristics of air-lift pumps operating in gas–liquid two-phase flow, Chinese Journal of Chemical Engineering 26 (2) (2018) 219–227. doi:10.1016/j.cjche.2017.09.011.

[40] Z. Wang, Y. Jin, F. Huang, Investigation of the inner structure of gas–liquid flow in airlift pumps by laser-high speed visualization technology, Asia-Pacific Journal of Chemical Engineering 15 (5) (may 2020). doi:10.1002/apj.2509.

[41] J. Zuo, F. Li, N. Zhang, D. He, W. Wang, J. Zhang, Experimental study on hydraulic characteristics of pneumatic lifting pump, Water 12 (2) (2020) 388. doi:10.3390/w12020388.

[42] E. Fayyadh, N. Mahdi, A. Mohammed, The effect of air injection system on airlift pump performance, FME Transactions 48 (4) (2020) 800–807. doi:10.5937/fme2004800f.

[43] V. Samaras, D. Margaris, Two-phase flow regime maps for air-lift pump vertical upward gas–liquid flow, International Journal of Multiphase Flow 31 (6) (2005) 757–766. doi:10.1016/j.ijmultiphaseflow.2005.03.001.

[44] P. Griffith, The prediction of low-quality boiling voids, Journal of Heat Transfer 86 (3) (1964) 327–333. doi:10.1115/1.3688684.

[45] P. Griffith, G. B. Wallis, Two-phase slug flow, Journal of Heat Transfer 83 (3) (1961) 307–318. doi:10.1115/1.3682268.

[46] S. E. Haaland, Simple and explicit formulas for the friction factor in turbulent pipe flow, Journal of Fluids Engineering 105 (1) (1983) 89–90. doi:10.1115/1.3240948.

[47] T. Yoshinaga, Y. Sato, Performance of an air-lift pump for conveying coarse particles, International Journal of Multiphase Flow 22 (2) (1996) 223–238. doi:10.1016/0301-9322(95)00067-4.

[48] P. J. Pritchard, R. W. Fox, A. T. McDonald, Fox and McDonald's Introduction to Fluid Mechanics, WILEY, 2011.

[49] S. L. Smith, Void fractions in two-phase flow: A correlation based upon an equal velocity head model, Proceedings of the Institution of Mechanical Engineers 184 (1) (1969) 647–664. doi:10.1243/pime_proc_1969_184_051_02.

[50] D. Chisholm, A theoretical basis for the lockhart-martinelli correlation for two-phase flow, International Journal of Heat and Mass Transfer 10 (12) (1967) 1767–1778. doi:10.1016/0017-9310(67)90047-6.

[51] D. Chisholm, A. Laird, Two-phase flow in rough tubes, Transactions of the American Society of Mechanical Engineers 80 (1958) 276–286.

[52] X. Fang, Y. Xu, Z. Zhou, New correlations of single-phase friction factor for turbulent pipe flow and evaluation of existing single-phase friction factor correlations, Nuclear

Engineering and Design 241 (3) (2011) 897–902. doi:10.1016/j.nucengdes.2010.12.019.

[53] A. Tomiyama, N. Furutani, H. Minagawa, T. Sakaguchi, Numerical analyses of air lift pumps based on the multi-fluid model, Japanese journal of multiphase flow 6 (2) (1992) 173–188. doi:10.3811/jjmf.6.173.

[54] T. Kajishima, T. Saito, Numerical simulation of unsteady flow in air-lift pump., JSME International Journal Series B 39 (3) (1996) 525–532. doi:10.1299/jsmeb.39.525.

[55] K. Pougatch, M. Salcudean, Application of CFD methods to the analysis of the flow in air-lift pump, in: Volume 3: Pipeline and Riser Technology CFD and VIV, ASME, 2007. doi:10.1115/omae2007-29099.

[56] K. Pougatch, M. Salcudean, Numerical modelling of deep sea air-lift, Ocean Engineering 35 (11-12) (2008) 1173–1182. doi:10.1016/j.oceaneng.2008.04.006.

[57] Q. Meng, C. Wang, Y. Chen, J. Chen, A simplified CFD model for air-lift artificial upwelling, Ocean Engineering 72 (2013) 267–276. doi:10.1016/j.oceaneng.2013.07.006.

[58] P. Hanafizadeh, M. Saidi, M. Darbandi, A. Kebriaee, Numerical simulation of two-phase flow in airlift pumps using the physical influence scheme, Progress in Computational Fluid Dynamics, An International Journal 10 (3) (2010) 186. doi:10.1504/pcfd.2010.033330.

[59] P. Hanafizadeh, M. H. Saidi, A. Karimi, A. Zamiri, Effect of bubble size and angle of tapering upriser pipe on the performance of airlift pumps, Particulate Science and Technology 28 (4) (2010) 332–347. doi:10.1080/02726351.2010.496300.

[60] P. Hanafizadeh, A. Karimi, M. H. Saidi, Effect of step geometry on the performance of the airlift pump, International Journal of Fluid Mechanics Research 38 (5) (2011) 387–408. doi:10.1615/interjfluidmechres.v38.i5.10.

[61] P. Hanafizadeh, M. Moezi, M. H. Saidi, Simulation of gas-liquid two phase flow in upriser pipe of gas-lift systems, Energy Equipment and Systems (2014).

[62] X. Li, H. Jeong, H. Chung, CFD modeling of unsteady gas-liquid flow in a small scale air-lift pump, Journal of the Korea Society For Power System Engineering 16 (1) (2012) 30–37. doi:10.9726/kspse.2012.16.1.030.

[63] E. M. Wahba, M. A. Gadalla, D. Abueidda, A. Dalaq, H. Hafiz, K. Elawadi, R. Issa, On the performance of air-lift pumps: From analytical models to large eddy simulation, Journal of Fluids Engineering 136 (11) (2014) 111301. doi:10.1115/1.4027473.

[64] A. A. M. H. Alasadi, A. K. Habeeb, Experimental and numerical simulation of an airlift pump with conventional and modified air injection device, Journal of Engineering (University of Baghdad) (2017).

[65] M. Shallouf, W. H. Ahmed, S. Abdou, Engineered-airlift pumps for aquaculture applications using multiphase flow analysis, Aquacultural Engineering 87 (2019) 101998. doi:10.1016/j.aquaeng.2019.101998.

[66] S. Hjalmars, The origin of instability in airlift pumps, Journal of Applied Mechanics 40 (2) (1973) 399–404. doi:10.1115/1.3422994.

[67] N. Apazidis, Influence of bubble expansion and relative velocity on the performance and stability of an airlift pump, International Journal of Multiphase Flow 11 (4) (1985) 459–479. doi:10.1016/0301-9322(85)90070-9.

[68] F. D. Cachard, J. Delhaye, Stability of small diameter airlift pumps, International Journal of Multiphase Flow 24 (1) (1998) 17–34. doi:10.1016/s0301-9322(97)00041-4.

[69] A.-F. Mahrous, Performance study of an airlift pump with bent riser tube, WSEAS Transactions on Applied and Theoretical Mechanics (2013).

[70] H. E. Zaraki, M. Majidniya, M. H. Abadshapoori, M. H. Saidi, Experimental investigation of flowregime and efficiency of airliftpumps with tapered upriser pipe, Multiphase Science and Technology 28 (2) (2016).

[71] G. Ligus, D. Zając, M. Masiukiewicz, S. Anweiler, A new method of selecting the airlift pump optimum efficiency at low submergence ratios with the use of image analysis, Energies 12 (4) (2019) 735. doi:10.3390/en12040735.

[72] I. I. Esen, Experimental investigation of a rectangular airlift pump, Advances in Civil Engineering 2010 (2010) 1–5. doi:10.1155/2010/789547.

[73] A. Tramba, A. Topalidou, E. G. Kastrinakis, S. G. Nychas, P. Francois, O. Scrivener, Visual study of an airlift pump operating at low submergence ratios, The Canadian Journal of Chemical Engineering 73 (5) (1995) 755–764. doi:10.1002/cjce.5450730519.

[74] C. H. Sohn, S. H. Kim, J. Y. Hwang, Effects of insertion of blunt body on bubble pattern and pumping performance in air-lift pump, Journal of Mechanical Science and Technology 32 (2) (2018) 969–976. doi:10.1007/s12206-018-0147-8.

[75] A. Oueslati, A. Megriche, The effect of liquid temperature on the performance of an airlift pump, Energy Procedia 119 (2017) 693–701. doi:10.1016/j.egypro.2017.07.096.

[76] A. Dare, O. Oturuhoyi, Experimental investigation of air lift pump, Afr. J. Sci. Technol.: Sci. Eng. Ser., 8 (1) (2007), pp. 56-62 (2007).

[77] I. Catrawedarma, Deendarlianto, Indarto, Statistical characterization of flow structure of air–water two-phase flow in airlift pump–bubble generator system, International

Journal of Multiphase Flow 138 (2021) 103596. doi:10.1016/j.ijmultiphaseflow.2021.103596.

[78] D. Hu, C.-L. Tang, S.-P. Cai, F.-H. Zhang, The effect of air injection method on the airlift pump performance, Journal of Fluids Engineering 134 (11) (oct 2012). doi:10.1115/1.4007592.

[79] D. Zheng, X. He, D. Che, CFD simulations of hydrodynamic characteristics in a gas–liquid vertical upward slug flow, International Journal of Heat and Mass Transfer 50 (21-22) (2007) 4151–4165. doi:10.1016/j.ijheatmasstransfer.2007.02.041.

[80] F. H. J. Imada, F. Saltara, J. L. Baliño, Numerical study of the churn-slug transition dynamics in vertical upward air-water flows, in: Computational Methods in Multiphase Flow VII, WIT Press, 2013. doi:10.2495/mpf130091.

[81] P. Horgue, F. Augier, M. Quintard, M. Prat, A suitable parametrization to simulate slug flows with the volume-of-fluid method, Comptes Rendus Mécanique 340 (6) (2012) 411–419. doi:10.1016/j.crme.2012.01.003.

[82] N. Ratkovich, S. Majumder, T. Bentzen, Empirical correlations and CFD simulations of vertical two-phase gas–liquid (newtonian and non-newtonian) slug flow compared against experimental data of void fraction, Chemical Engineering Research and Design 91 (6) (2013) 988–998. doi:10.1016/j.cherd.2012.11.002.

[83] T. Taha, Z. Cui, CFD modelling of slug flow in vertical tubes, Chemical Engineering Science 61 (2) (2006) 676–687. doi:10.1016/j.ces.2005.07.022.

[84] M. Abdulkadir, V. Hernandez-Perez, S. Lo, I. Lowndes, B. Azzopardi, Comparison of experimental and computational fluid dynamics (CFD) studies of slug flow in a vertical riser, Experimental Thermal and Fluid Science 68 (2015) 468–483. doi:10.1016/j.expthermflusci.2015.06.004.

[85] J. Jaeger, C. Santos, L. Rosa, H. Meier, D. Noriler, Experimental and numerical evaluation of slugs in a vertical air–water flow, International Journal of Multiphase Flow 101 (2018) 152–166. doi:10.1016/j.ijmultiphaseflow.2018.01.009.

[86] G. Montoya, D. Lucas, E. Baglietto, Y. Liao, A review on mechanisms and models for the churn-turbulent flow regime, Chemical Engineering Science 141 (2016) 86–103. doi:10.1016/j.ces.2015.09.011.

[87] E. Da Riva, D. Del Col, Numerical simulation of churn flow in a vertical pipe, Chemical Engineering Science 64 (17) (2009) 3753–3765. doi:10.1016/j.ces.2009.04.049.

[88] M. Parsi, M. Agrawal, V. Srinivasan, R. E. Vieira, C. F. Torres, B. S. McLaury, S. A. Shirazi, E. Schleicher, U. Hampel, Assessment of a hybrid CFD model for simulation of complex vertical upward gas–liquid churn flow, Chemical Engineering Research and Design 105 (2016) 71–84. doi:10.1016/j.cherd.2015.10.044.

[89] V. Hernandez-Perez, M. Abdulkadir, B. Azzopardi, Grid generation issues in the CFD modelling of two-phase flow in a pipe, The Journal of Computational Multiphase Flows 3 (1) (2011) 13–26. doi:10.1260/1757-482x.3.1.13.

[90] M. Tekavčič, B. Končar, I. Kljenak, Analysis of vertical co-current air-water flow with the neptune_CFD, Nuclear Engineering and Design 321 (2017) 144–155. doi:10.1016/j.nucengdes.2016.12.006.

[91] E. Guerrero, F. Muñoz, N. Ratkovich, Comparison between eulerian and vof models for two-phase flow assessment in vertical pipes, CT&F - Ciencia, Tecnología y Futuro 7 (1) (2017) 73–84. doi:10.29047/01225383.66.

[92] G. H. Yeoh, T. Barber, Assessment of interface capturing methods in computational fluid dynamics (CFD) codes — a case study, The Journal of Computational Multiphase Flows 1 (2) (2009) 201–215. doi:10.1260/175748209789563946.

[93] ANSYS, ANSYS CFX-Solver Theory Guide Release 19.2 (2019).

[94] J. Brackbill, D. Kothe, C. Zemach, A continuum method for modeling surface tension, Journal of Computational Physics 100 (2) (1992) 335–354. doi:10.1016/0021-9991(92)90240-y.

[95] P. J. Zwart, M. Scheuerer, M. Bogner, Free surface flow modelling of an impinging jet, in: ASTAR International Workshop on Advanced Numerical Methods for Multidimensional Simulation of Two-Phase Flow, 2003.

[96] A. Wael, Personal Communication, March 13, 2020.

[97] Y. Xu, X. Fang, X. Su, Z. Zhou, W. Chen, Evaluation of frictional pressure drop correlations for two-phase flow in pipes, Nuclear Engineering and Design 253 (2012) 86–97. doi:10.1016/j.nucengdes.2012.08.007.

[98] A. J. Ghajar, S. M. Bhagwat, Flow patterns, void fraction and pressure drop in gas-liquid two phase flow at different pipe orientations, in: L. Cheng (Ed.), Frontiers and Progress in Multiphase Flow I, Springer International Publishing, 2014. doi:10.1007/978-3-319-04358-6_4.

[99] J. R. Thome, A. Cioncolini, Two-phase pressure drop, in: Encyclopedia of Two-Phase Heat Transfer and Flow I, WORLD SCIENTIFIC, 2015, pp. 143–176. doi:10.1142/9789814623216_0023.

[100] G. Wallis, One-Dimensional Two-phase flow, McGraw-Hill, New York, 1969.

[101] J. Hills, The operation of a bubble column at high throughputs 12 (2) (1976) 89–99. doi:10.1016/0300-9467(76)87002-5.

[102] R. W. Lockhart, R. C. Martinelli, Proposed correlation of data for isothermal two-phase, two-component flow in pipes, Chemical Engineering Progress 45 (1) (1949) 39–48.

[103] K. Mishima, T. Hibiki, Some characteristics of air-water two-phase flow in small diameter vertical tubes, International Journal of Multiphase Flow 22 (4) (1996) 703–712. doi:10.1016/0301-9322(96)00010-9.

[104] L. Sun, K. Mishima, Evaluation analysis of prediction methods for two-phase flow pressure drop in mini-channels, International Journal of Multiphase Flow 35 (1) (2009) 47–54. doi:10.1016/j.ijmultiphaseflow.2008.08.003.

[105] L. Friedel, Improved friction pressure drop correlations for horizontal and vertical two-phase pipe flow, in: European Two-Phase Flow Group Meeting, 1979.

[106] H. Müller-Steinhagen, K. Heck, A simple friction pressure drop correlation for two-phase flow in pipes, Chemical Engineering and Processing: Process Intensification 20 (6) (1986) 297–308. doi:10.1016/0255-2701(86)80008-3.

[107] B. Wu, M. Firouzi, T. Mitchell, T. E. Rufford, C. Leonardi, B. Towler, A critical review of flow maps for gas-liquid flows in vertical pipes and annuli, Chemical Engineering Journal 326 (2017) 350–377.

[108] C. E. Brennen, Fundamentals of Multiphase Flows, Cambridge University Press, 2005.

[109] I. Kataoka, I. Mamoru, Drift flux model for large diameter pipe and new correlation for pool void fraction, International Journal of Heat and Mass Transfer 30 (9) (1987) 1927–1939. doi:10.1016/0017-9310(87)90251-1.

[110] H. Anglart, Progress in understanding and modelling of annular two-phase flows with heat transfer, Nuclear Engineering and Design 345 (2019) 166–182. doi:10.1016/j.nucengdes.2019.02.007.

[111] L. Cheng, G. Ribatski, J. R. Thome, Two-phase flow patterns and flow-pattern maps: Fundamentals and applications, Applied Mechanics Reviews 61 (5) (jul 2008). doi:10.1115/1.2955990.

[112] P. Wiedemann, A. Döß, E. Schleicher, U. Hampel, Fuzzy flow pattern identification in horizontal air-water two-phase flow based on wire-mesh sensor data, International Journal of Multiphase Flow 117 (2019) 153–162. doi:10.1016/j.ijmultiphaseflow.2019.05.004.

[113] G. Montoya, Developement and validation of advanced theoretical modeling for churn-turbulent flows and subsequent transitions, Ph.D. thesis, Helmholtz-Zentrum Dresden - Rossendorf (2015).

[114] P. Coste, A large interface model for two-phase CFD, Nuclear Engineering and Design 255 (2013) 38–50. doi:10.1016/j.nucengdes.2012.10.008.

[115] G. Černe, S. Petelin, I. Tiselj, Coupling of the interface tracking and the two-fluid models for the simulation of incompressible two-phase flow, Journal of Computational Physics 171 (2) (2001) 776–804. doi:10.1006/jcph.2001.6810.

[116] S. Hänsch, D. Lucas, E. Krepper, T. Höhne, A multi-field two-fluid concept for transitions between different scales of interfacial structures, International Journal of Multiphase Flow 47 (2012) 171–182. doi:10.1016/j.ijmultiphaseflow.2012.07.007.

[117] S. L. Sharma, M. Ishii, T. Hibiki, J. P. Schlegel, Y. Liu, J. R. Buchanan, Beyond bubbly two-phase flow investigation using a CFD three-field two-fluid model, International Journal of Multiphase Flow 113 (2019) 1–15. doi:10.1016/j.ijmultiphaseflow.2018.12.010.

[118] E. Adaze, A. Al-Sarkhi, H. M. Badr, E. Elsaadawy, Current status of CFD modeling of liquid loading phenomena in gas wells: a literature review, Journal of Petroleum Exploration and Production Technology 9 (2) (2018) 1397–1411. doi:10.1007/s13202-018-0534-4.

[119] Y. Liu, J. Cui, W. Li, A two-phase, two-component model for vertical upward gas–liquid annular flow, International Journal of Heat and Fluid Flow 32 (4) (2011) 796–804. doi:10.1016/j.ijheatfluidflow.2011.05.003.

[120] D. Alaita, M. Hossain, S. Z. Islam, Modelling multiphase flow in vertical pipe using CFD method, in: Proceedings of the 1st International Conference on Numerical Modelling in Engineering, Springer Singapore, 2018, pp. 300–319. doi:10.1007/978-981-13-2273-0_24.

Appendix A

Supplementary Two-Phase Flow Theory

This appendix provides background information on gas-liquid flows and the numerical modelling of such flows. The scope of the subsequent discussion is broader than what is minimally necessary to understand the airlift pump, but it provides context to the decisions made in this work.

A.1 Discussion of Upward Vertical Flow Regimes

Upward vertical gas-liquid flows are typically classified as bubbly, slug, churn, or annular. Further distinctions are often made within a given flow pattern as the focus of research narrows. Very small tubes (under 10 mm in diameter), are known as capillary tubes and have different flow regimes than standard sized vertical pipes [107]. In capillary tubes the capillary forces replace the effects of gravity, requiring special treatment. For example, bubbly flow is not present in capillary tubes.

Bubbly Bubble flow, sometimes broken into dispersed bubbly and bubbly flow, occurs at low gas superficial velocities. The volume fraction of gas is the lowest of the four standard flow patterns. Different bubble shapes (spherical, ellipsoid, cap) occur depending on the bubble Reynolds, Eötvös, and Morton numbers [108]. The bubble morphology strongly influences the bubble dynamics, in turn impacting the global flow. Studying the coalescence, breakup, deformation, and dynamics of bubbles is an important aspect of bubbly flow.

Slug With increasing gas superficial velocity and void fraction, the gas phase forms large bullet-shaped bubbles known as slugs, or Taylor bubbles. The gas slugs travel up the pipe at a steady rate and regular frequency. The liquid experiences local recirculation where a thin film of liquid flows down around the slug next to the wall, liquid then flows up in the wake of the slug before being pulled down by the next slug. The pipe diameter influences the transition and presence of slug flow. The larger the pipe diameter the larger the Taylor bubble must be to span the width of the pipe, increasing the probability of interface instabilities. Isao and Ishii [109] theoretically determined maximum pipe diameter allowing slug flow to be approximately 110 mm for air-water systems. The frequency, length, and velocity of slugs can be determined by cross-correlation of void fraction time signals recorded at two planes separated by a small axial distance [80].

Churn The physics of churn flow is poorly understood compared to other flow regimes, leading to inconsistent definitions of the regime [86]. The term churn flow or some derivative has been used to refer to the transition from bubbly to slug flow, transition from slug flow to annular, or the transition from bubbly to annular flow when slug flow is not present. The physical mechanism responsible for transporting liquid are still debated [87]. In any of the above definitions, churn flow is a highly turbulent and irregular, with a wide range of interfacial length scales and structures.

Annular In the annular flow regime liquid flows up the pipe walls, the thickness of the film decreases with increasing gas superficial velocity. The core region consists primarily of the gas phase, with a small proportion of liquid droplets. There is a continuous entrainment and deposition of liquid droplets occurring at the interface between the core and liquid film. The liquid film interface is not flat and steady, rather liquid is transported up through large scale wave in the film know as ‘roll waves’. The roll waves strongly influence the entrainment and deposition of liquid droplets. The presence of smaller amplitude and higher frequency secondary waves has been observed, but they do not contribute significantly to liquid transport [110].

A.1.1 Identification of Flow Regimes

Identifying flow regimes is not an exact science; it often involves a subjective component [107]. Visual observation is the most common method for determining flow patterns but it is not the most reliable. Flow regime transition is particularly difficult to classify by visual inspection. Advanced imaging techniques have been developed to take snapshots of the flow but still they require a researcher to look at images and qualitatively determine the flow pattern. Examining still images of a transient phenomena can be misleading. Visual identification of flow regimes is a major source of the discrepancy that exists in the literature [111].

Similar to the statistical study of turbulence in single-phase flows, the temporal fluctuations of the flow can be better interpreted and quantified by stochastic methods. Another advantage of statistical analysis over direct visual identification of flow regimes is the PDF shows the gradual transition from one flow regime to the next. Statistical methods are the basis of state-of-the-art flow regime identification algorithms being developed for industrial applications [112].

A.2 Numerical Modeling Approaches

The necessary theory behind the homogeneous VOF model used in the present work has been described in Sections 2.2 & 3.2, however, their are many other modeling techniques for two-phase flows. This Appendix provides general information on the different modeling techniques from a broader perspective. Better understanding of the strengths and weaknesses of different modeling approaches helps put the challenges of modeling the gas-liquid flow occurring in the airlift pump into context.

A.2.1 Homogeneous Multiphase Model

The flow is modeled with a single Eulerian field with mixture properties, determined by a volume fraction weighted average. An interface tracking technique is required to track the interface between discrete phasic regions and produce physically realistic interfacial shape. Volume of fluid (VOF) is the most commonly used interface tracking technique in commercial CFD codes. Other interface techniques, such as level-set method can also be used with a homogeneous model. Furthermore, the VOF method can be extended to an inhomogeneous model.

When using the VOF approach, a volume fraction transport equation is solved to track the phasic interface through the domain. Various advection schemes (referred to as interface sharpening) are used to solve the volume fraction equation, with the aim of preventing diffusion or 'smearing' of the phasic interface. Whereas, interface reconstruction techniques approximate an interface shape within each control volume. In general, interface reconstruction is more computationally expensive and less robust than interface sharpening, but it can produce a clearer interface, especially on a coarser mesh. Regardless of whether interface sharpening or reconstruction is used, a clearly resolved phasic interface is critical for the accuracy of the homogeneous model because of the assumption of a shared velocity field.

Surface tension is an important phenomena affecting the interface shape and flow dynamics [113]. The continuum surface force (CSF) model by Brackbill *et al.* [94] is frequently used to account for the surface tension force. The surface tension force must be applied only at the interface between phases, thus the clear resolution of the phasic interface is directly related to the accuracy of the interface dynamics.

A.2.2 Multi-Fluid Multiphase Model

The multi-fluid model treats each phase as its own Eulerian field (inhomogeneous approach), making it suitable to dispersed flows. The separate velocity fields introduce the need for closure relationships for the momentum transfer between phases. The interfacial momentum transfer is the product of two components: interfacial area, and interfacial force. The multiphase model is more commonly refereed to as the two-fluid model when working with gas-liquid flows.

The inhomogeneous approach is often more computationally expensive than the homogeneous model because more PDE's are solved. The increased computational cost of the multi-fluid model can be counteracted by lower mesh resolution requirements [91]. When the particle model is used, minimum mesh size is limited by the particle diameter and convergence performance improves with smaller particle size relative to mesh size.

A.2.3 Large Interface Capturing

In complex real world flows a wide range of interfacial scales coexist, making it difficult to apply either the homogeneous VOF or multi-fluid particle models. Several techniques have been proposed to merge the homogeneous VOF and inhomogeneous particle models, gaining the benefits of each. Some examples are, large interface modeling LIM [114], multi-fluid VOF [115], and GENTOP [116].

The concept is simple in principle: resolve large interfacial scales and model the smaller scales. Analogous to LES turbulence modeling, the switch between resolved and modeled depends on the mesh size. In application, large interface capturing techniques become complex and vary between codes. The selection of interfacial area model is based on volume fraction or volume fraction gradients in nearby cells. Particle closure models are used in dispersed regions (low volume fraction gradient). Free surface regions are identified by high volume fraction gradients and interface sharpening is applied. The combined approach of large interface capturing make the model less sensitive to input parameters and less a priori knowledge of the flow is required.

A.2.4 Model Selection Based on Flow Regime

There is no general purpose multiphase CFD model that is suitable to all gas-liquid flows because the interfacial scales and flow characteristics vary greatly between regime and application. Instead, the appropriate model must be selected based on the flow regime expected, and phenomena of interest.

Bubbly Flow

The two-fluid model is the predominant choice for RANS simulations. The interfacial length scale of the small bubble sizes are too small to be practically resolved by the mesh. The homogeneous approach can be taken when performing DNS with the mesh small enough to resolve the bubbles, but this is limited to the study of a single bubble or a small group of bubbles.

Slug Flow

The size of Taylor bubbles are generally large enough to be resolved by the mesh making the homogeneous model a viable approach. The different interface capturing techniques discussed in Section A.2.1 influence the accuracy and mesh requirements of the simulation. No matter the interface-capturing technique, a fine mesh is needed at the wall to properly resolve the thin liquid film between the gas slug and the wall.

Surface tension is an important force in slug flow, and the CSF model is used most frequently. The surface tension body force requires a small timestep size for numerical stability, generally on the order of 1×10^{-4} s. Even though the frequency and motion of slugs is steady, a transient solution is needed because the velocity field at a given location will always fluctuate with the passage of a slug.

Two-fluid models are generally not used for slug flow, unless it is a polydispersed model focused on the development of smaller bubbles coalescing into large bubbles forming slugs [117]. Two-fluid models may predict reasonable average quantities, but will not resolve distinct slugs and accurate local instantaneous flow patterns.

Churn Flow

Churn flow is an especially difficult flow regime to accurately capture due to the wide range of interacting length scales and highly turbulent nature [86]. The homogeneous VOF model has been applied with limited success. The two primary shortcomings of the homogeneous approach are the effects of small bubbles and droplets are lost and uncertainty in the accuracy of the turbulence modeling [87]. Large interface capturing approaches have shown promise in modeling churn flow because they can better capture the effects of small interfacial scales lost in the homogeneous model [88].

Regardless of the modeling approach taken, the use of a 3D domain is recommended, 2D axisymmetric simplification produces a physically unrealistic pocket of water in the center of the pipe [90]. Like with slug flow, a fine mesh is required at the wall to capture the thin liquid film. A transient simulation is required with relatively long measurement window (5 to 20 s) to record average flow measurements. All factors combine to make churn flow modeling extremely computationally expensive.

Annular Flow

The VOF interface tracking method is suitable for resolving the interface between the gas core and liquid film of annular flow. At very high superficial velocities, difficulties arise when the liquid film becomes very thin. Either an extremely fine mesh is required near the wall to resolve the liquid film, or a wall wetting model is used to prescribe the film thickness by setting the volume fraction in the first few wall adjacent cells [118]. The entrainment and deposition of liquid droplets between the gas core and liquid film is a weak point of the modeling, regardless of whether a homogeneous VOF or large interface capturing model is used [119].

A.2.5 Summary of CFD Modeling for Gas-Liquid Flow

The application of Euler-field-based CFD models to gas-liquid vertical pipe flow regimes has been discussed in previous sections. The following summary and guiding principles are applicable to any gas-liquid flow.

The two-fluid model is suited to modeling dispersed phases where the interfacial length scales are small. When the phasic interface is modeled using the particle approach steady-state simulations can be used, provided there are no global flow instabilities that dictate a transient simulation. The accuracy of the two-fluid model is largely dependent on the closure relations required for interfacial momentum transfer.

As superficial velocities increase and discrete phasic regions appear, the need to resolve and track the interface necessitates the use of the homogeneous VOF model. Interface tracking means the phasic interface is resolved by the mesh, which dictates the need for a fine mesh and transient simulation. The surface tension force becomes an important mechanism affecting the interface shape.

The homogeneous VOF model inevitably fails to capture the effects of small interfacial length scale due to practical mesh and computing limitations. The importance of the small interfacial length scales depends on the nature of the flow. Large interface capturing models are a hybrid of the two-fluid particle model and the homogeneous VOF that aim to capture the full range of interfacial length scales. The hybrid approach is theoretically the most universal of the three multiphase models, but it still relies on accurate closure relations. The method and technical implementation of coupling the VOF interface capturing with the two-fluid particle model is still an ongoing effort [116]. Promising results have been reported in literature, the ‘Multi-fluid VOF’ model in ANSYS Fluent was able to capture all vertical flow regimes from bubbly to annular [120].

Appendix B

Two-phase Flow Correlations

This appendix gives the details of the various correlations referenced in this work. Correlations were required for the prediction of void fraction and frictional pressure drop.

B.1 Void Fraction

The correlations used for the prediction of the void fraction are categorized by either drift-flux based models or other forms.

B.1.1 Drift Flux Coefficients

The drift-flux model is used to predict the void fraction with the general equation.

$$\frac{J_G}{\langle \alpha_G \rangle_{\mathrm{A}}} = C_0 J_{\mathrm{tot}} + v_d \tag{B.1}$$

The correlations for the distribution coefficient and drift velocity are presented below.

White and Beardmore

Two versions are used:

1. Reported by de Cachard and Delhaye [21].

$$C_0 = 1.2 \tag{B.2}$$

$$v_d = \Gamma \sqrt{gd} \tag{B.3}$$

$$\Gamma = 0.345 \left(1 - e^{\frac{-0.01 N_f}{0.345}}\right) (1 - e^{\frac{3.37 - \mathrm{Eo}^{-1}}{m}}) \tag{B.4}$$

$$m = \begin{cases} 25 & N_f \leq 18 \\ 69(N_f)^{-0.35} & 18 < N_f < 250 \\ 10 & N_f \geq 250 \end{cases} \tag{B.5}$$

where

$$(N_f)^2 = \frac{\rho_L(\rho_L - \rho_G)gd^3}{\mu_L^2} \tag{B.6}$$

valid for $(N_f)^2 < 3\times10^5$

2. The simplified version reported by Reinemann *et al.* [20].

$$\Gamma = 0.352\left(1 - 3.18\mathrm{Eo}^{-1} - 14.77\mathrm{Eo}^{-2}\right) \tag{B.7}$$

Hills

Hills [101] suggested a modified form on the drift-flux correlation based on experiments using a bubble column.

$$\frac{J_G}{\langle\alpha_G\rangle_\mathrm{A}} = 1.35(J_\mathrm{tot})^{0.93} + 0.24 \tag{B.8}$$

B.1.2 Other Void Fraction Correlations

Void fraction correlations not following the general drift-flux model framework are presented in the following sections.

Lockhart-Martinelli Parameter Correlation (LM)

Lockhart and Martinelli [102] proposed a correlation for the void fraction using the Lockhart-Martinelli parameter which is also used in the prediction of the two-phase frictional pressure drop. The correlation as reported by Wallis [100] is as follows:

$$\alpha_G = (1 + X^{0.8})^{-0.378} \tag{B.9}$$

and X is the Lockhart-Martinelli parameter

$$X = \left(\frac{1-\chi}{\chi}\right)^{0.9} \left(\frac{\rho_G}{\rho_L}\right)^{0.5} \left(\frac{\mu_L}{\mu_G}\right)^{0.1} \tag{B.10}$$

and χ is the quality.

Smith correlation

The correlation for void fraction proposed by Smith [49]:

$$\alpha_G = \left(1 + A_1 \frac{\rho_G}{\rho_L} \left(0.4 + 0.6\sqrt{A_2}\right)\right)^{-1} \tag{B.11}$$

where

$$A_1 = \frac{1}{\chi} - 1 \tag{B.12}$$

and

$$A_2 = \frac{\frac{\rho_L}{\rho_G} + 0.4A_1}{1 + 0.4A_1} \tag{B.13}$$

B.2 Frictional Pressure Drop

The prediction of two-phase frictional pressure drop consists of two parts: a two-phase multiplier, and a fictitious single phase frictional pressure drop predicted by the conventional means of friction factor. Various correlations specify the single phase frictional pressure drop different but the correlation for friction factor is selected at the authors discretion

B.2.1 Two-phase Multipliers

The two-phase multiplier and their respective means of determining the fictitious single phase frictional pressure drop are given in the following sections.

Griffith and Wallace [45]

The pressure drop for a hypothetical single-phase liquid flowing at the total velocity J_{tot} is multiplied by a correction factor $\frac{J_L}{J_L+J_G}$ to give the two-phase frictional pressure drop.

$$\left(\frac{dP}{dx}\right)_{TP} = \frac{J_L}{J_G + J_L}\left(\frac{dP}{dx}\right)_{(G+L)} \tag{B.14}$$

$$\text{Re} = \frac{\rho_L D J_{\text{tot}}}{\mu_L} \tag{B.15}$$

Lockhart-Martinelli [102]

$$\left(\frac{dP}{dx}\right)_{TP} = \phi_\ell^2 \left(\frac{dP}{dx}\right)_{\ell} \tag{B.16}$$

where ϕ_ℓ^2 is the two-phase multiplier defined as

$$\phi_\ell^2 = 1 + \frac{C}{X} + \frac{1}{X^2} \tag{B.17}$$

and $C = 20$ for turbulent flows, X is defined in Eq. (B.10). $\left(\frac{dP}{dx}\right)_\ell$ is the pressure drop if liquid were to flow at the total mass flow rate $(\dot{m}_G + \dot{m}_L)$.

Friedel correlation

The Friedel [105] correlation as reported by Thome and Cioncolini [99].

$$\phi_\ell^2 = A_1 + \frac{3.24 A_2 A_3}{\text{Fr}^{0.045}\text{We}^{0.035}} \tag{B.18}$$

where

$$A_1 = (1-\chi)^2 + \chi^2 \frac{\rho_L f_g}{\rho_G f_\ell} \tag{B.19}$$

$$A_2 = \chi^{0.78}(1-\chi)^{0.224} \tag{B.20}$$

$$A_2 = \left(\frac{\rho_L}{\rho_G}\right)^{0.91} \left(\frac{\mu_G}{\mu_L}\right)^{0.19} \left(1 - \frac{\mu_G}{\mu_L}\right)^{0.7} \tag{B.21}$$

Fr and We are the Froude and Weber number, respectively.

$$\mathrm{Fr} = \frac{G^2}{g d \rho_{TP}^2} \tag{B.22}$$

$$\mathrm{We} = \frac{G^2 d}{\sigma \rho_{TP}} \tag{B.23}$$

Based on the mixture density defined as:

$$\rho_{TP} = \left(\frac{\chi}{\rho_G} + \frac{1-\chi}{\rho_L}\right)^{-1} \tag{B.24}$$

Müller-Steinhagen and Heck correlation [106]

$$\left(\frac{dP}{dx}\right)_{TP} = A_1(1-\chi)^{1/3} + \left(\frac{dP}{dx}\right)_\ell \chi^3 \tag{B.25}$$

where

$$A_1 = \left(\frac{dP}{dx}\right)_\ell + 2\left(\left(\frac{dP}{dx}\right)_g - \left(\frac{dP}{dx}\right)_\ell\right)\chi \tag{B.26}$$

Mishima and Hibiki correlation [103]

Following the Lockhart am Martinelli approach with C in Eq. (B.17) defined as

$$C = 21(1 - e^{-319d}) \tag{B.27}$$

where d is the pipe diameter in [mm]

Sun and Mishima correlation [104]

The correlation is a modification of the Lockhart am Martinelli approach where C in Eq. (B.17) is defined as

$$C = 1.79 \left(\frac{\mathrm{Re}_g}{\mathrm{Re}_\ell}\right)^{0.4} \left(\frac{1-\chi}{\chi}\right)^{0.5} \tag{B.28}$$

B.2.2 Friction Factor

As previously stated, standard single phase correlations are used to predict the friction factor; however, alternate definitions of the fluid properties and velocity may be used. All friction factor correlations used in the present work are for the Darcy-Weisbach friction factor. The frictional pressure drop is calculated as

$$\frac{dP}{dx} = \frac{f\rho V^2}{2d} \tag{B.29}$$

or the wall shear stress is given by

$$\tau_w = \frac{1}{8} f\rho V^2 \tag{B.30}$$

Blasius correlation

The Blasius equation as reported by [48]

$$f = \frac{0.316}{\mathrm{Re}^{1/4}} \tag{B.31}$$

valid for $\mathrm{Re} \leq 10^5$

Colebrook Equation

As reported by Haaland [46]

$$\frac{1}{\sqrt{f}} = -2\log\left(\frac{e/d}{3.7} + \frac{2.51}{\mathrm{Re}\sqrt{f}}\right) \tag{B.32}$$

where e is the surface roughness.

Fang *et al.* [52]

For smooth pipes and $3000 \leq \mathrm{Re} \leq 10^8$

$$f = 0.25\left(\log\left(\frac{150.39}{\mathrm{Re}^{0.98865}} - \frac{152.66}{\mathrm{Re}}\right)\right)^{-2} \tag{B.33}$$

Appendix C

Supplementary Results

For completeness, this appendix contains additional figures similar to those seen in Section 5. The plots are given in the order they occur in the body of this work.

C.1 Contour Plots

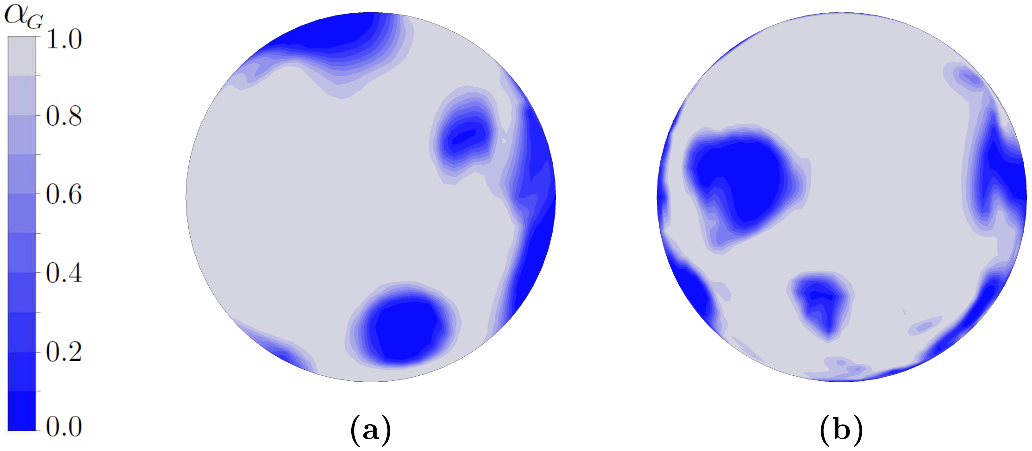

Figure C.1: Effect of mesh density on the sharpness of phasic interface: (a) coarser mesh from $k-\varepsilon$ simulation, and (b) finer mesh from SST simulation.

C.2 Axial Profiles

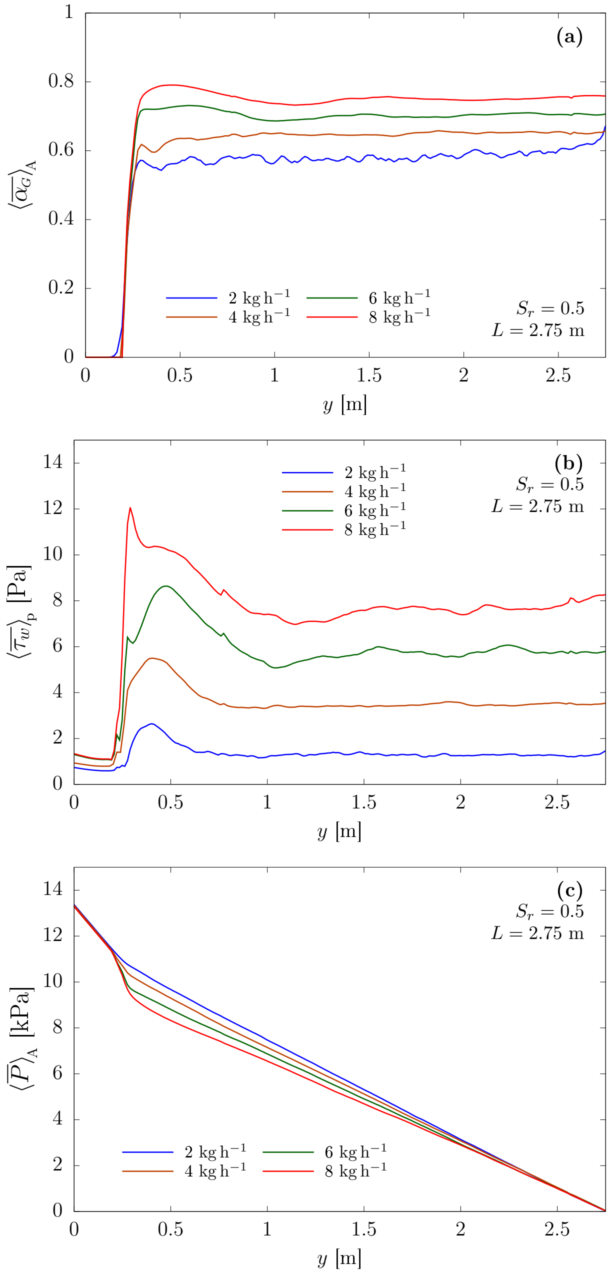

Figure C.2: Time-average axial profiles for C3: (a) area-averaged void fraction, (b) perimeter-averaged wall shear stress, and (c) area-averaged pressure.

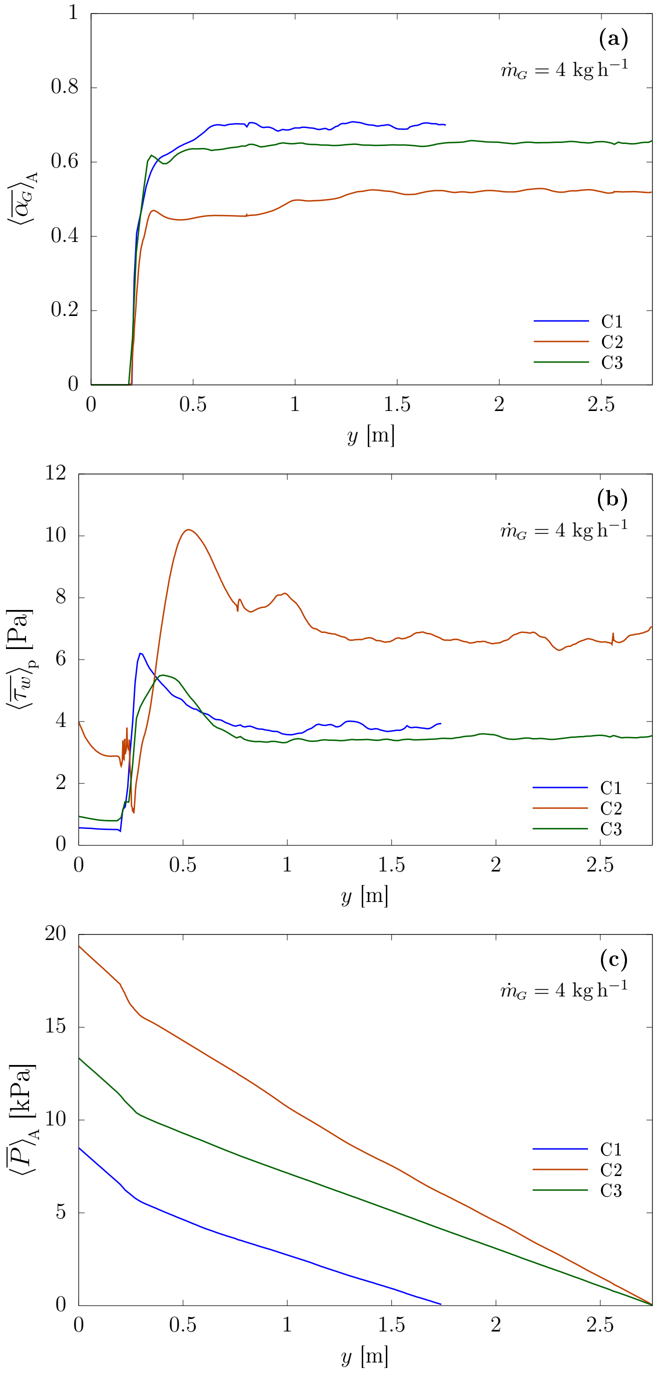

Figure C.3: Time-average axial profiles for $\dot{m}_G = 4$ kg h^{-1}: (a) area-averaged void fraction, (b) perimeter-averaged wall shear stress, and (c) area-averaged pressure.

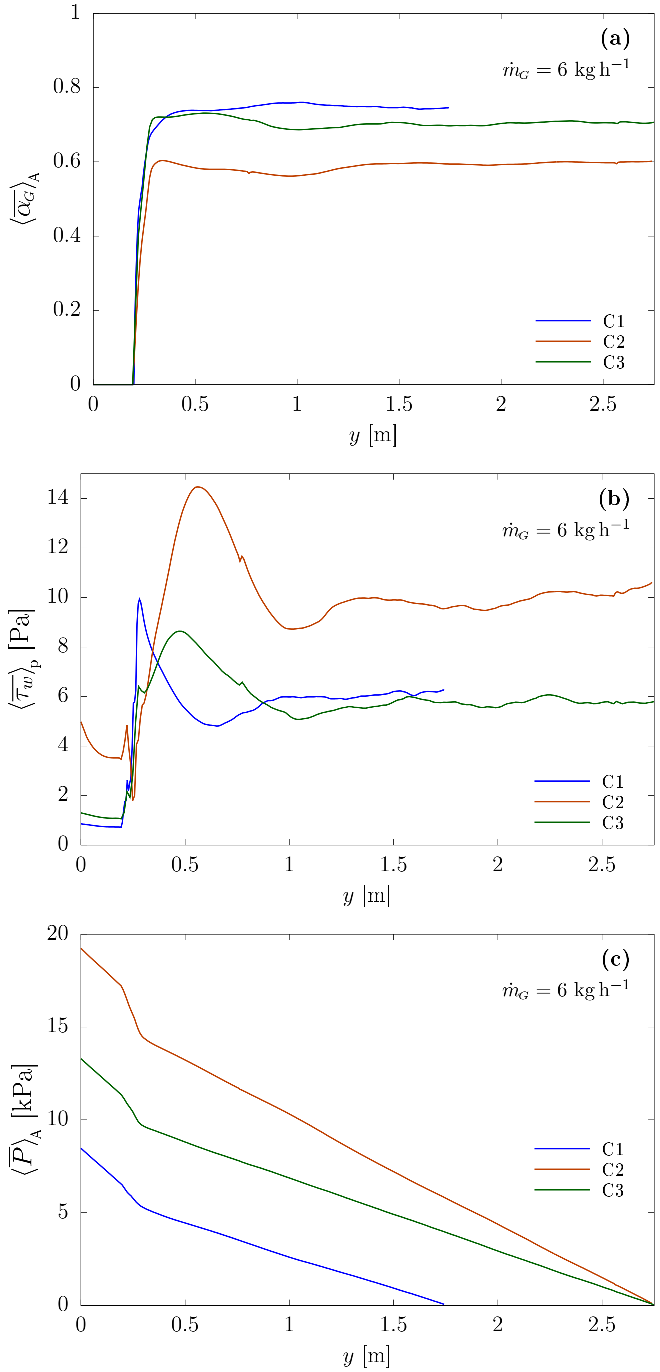

Figure C.4: Time-average axial profiles for $\dot{m}_G = 6$ kg h^{-1}: (a) area-averaged void fraction, (b) perimeter-averaged wall shear stress, and (c) area-averaged pressure.

C.3 PD Distribution

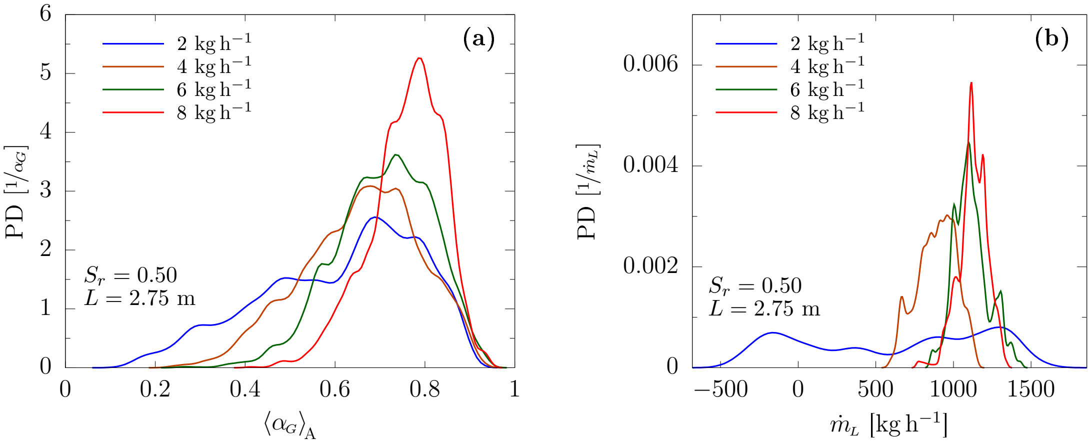

Figure C.5: PD distributions of (a) void fraction and (b) suction flow rate for C3.

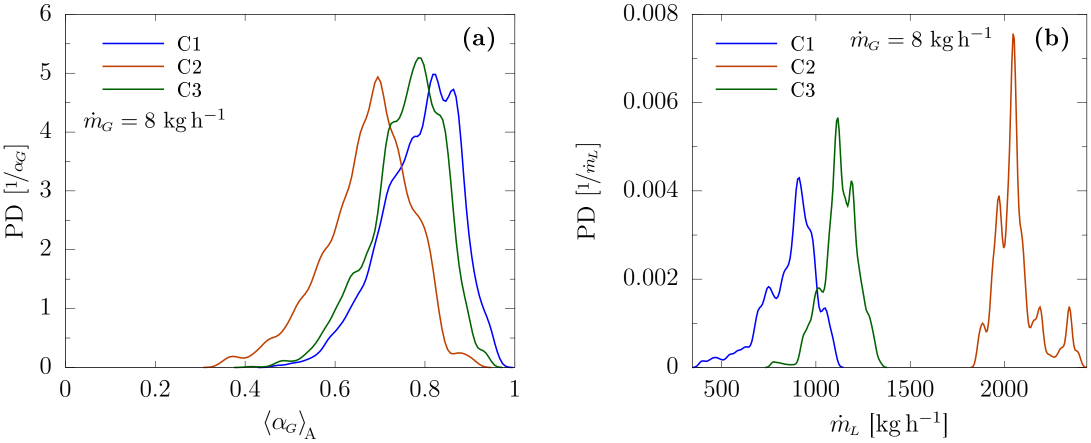

Figure C.6: Effect of riser length and submergence ratio on PD distributions of (a) void fraction and (b) suction flow rate for $\dot{m}_G = 8$ kg h^{-1}.

C.4 Relative Magnitude of Losses

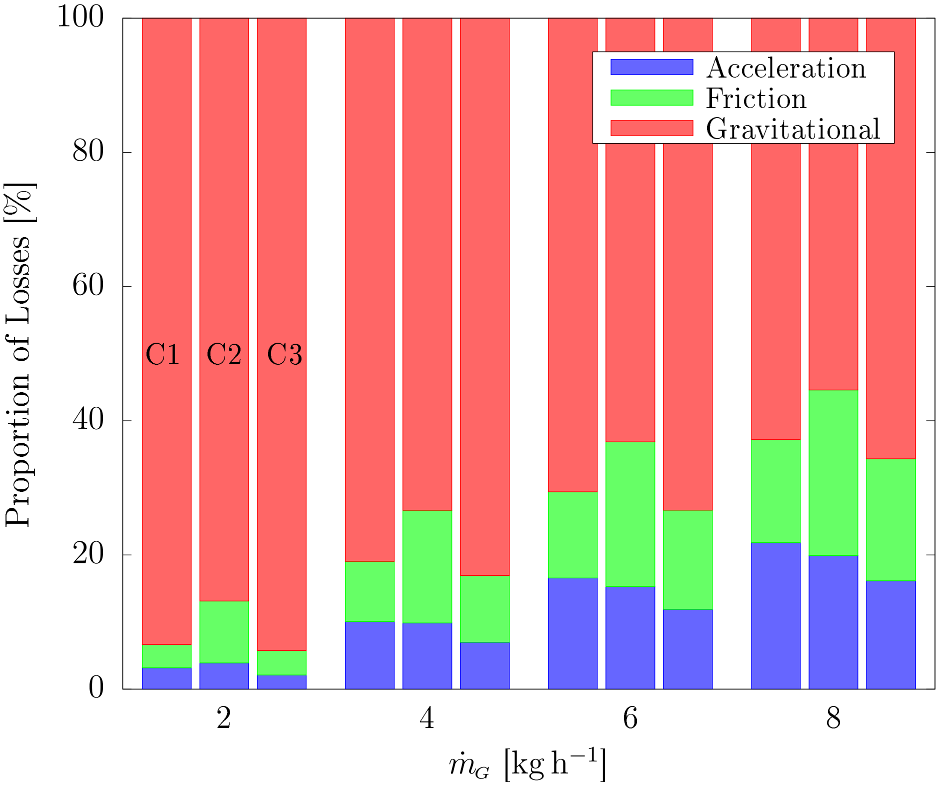

Figure C.7: Comparison of the relative magnitude of losses from the steady-state model of Kassab *et al.* [25].

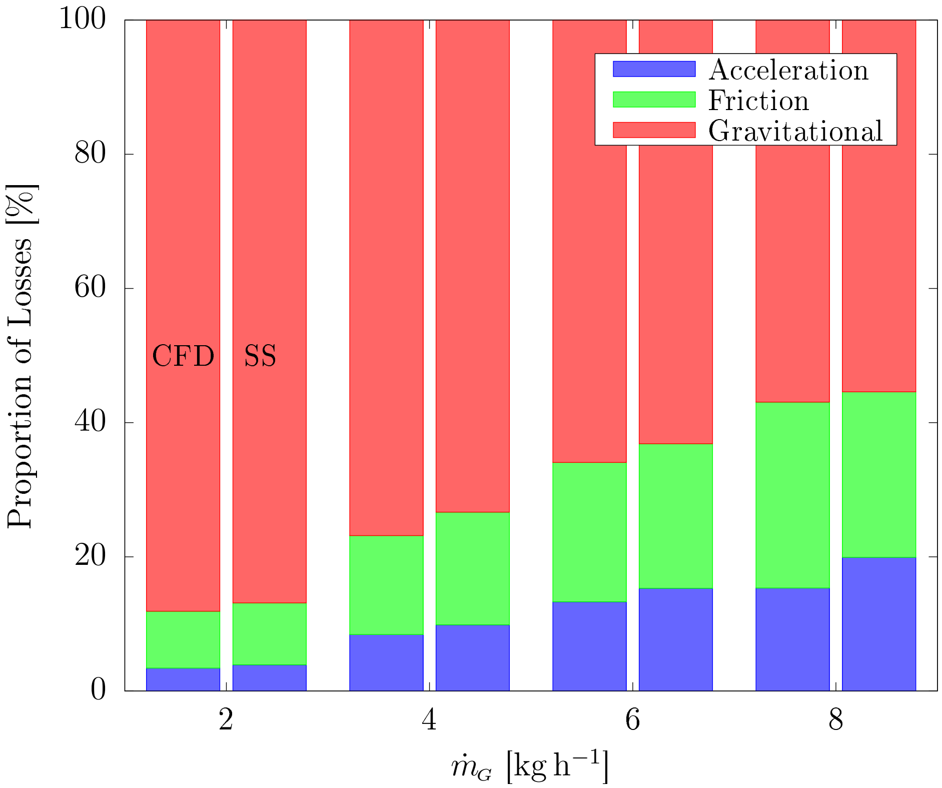

Figure C.8: Comparison of the relative magnitude of losses between the CFD model and steady-state model of Kassab *et al.* [25] for C2.

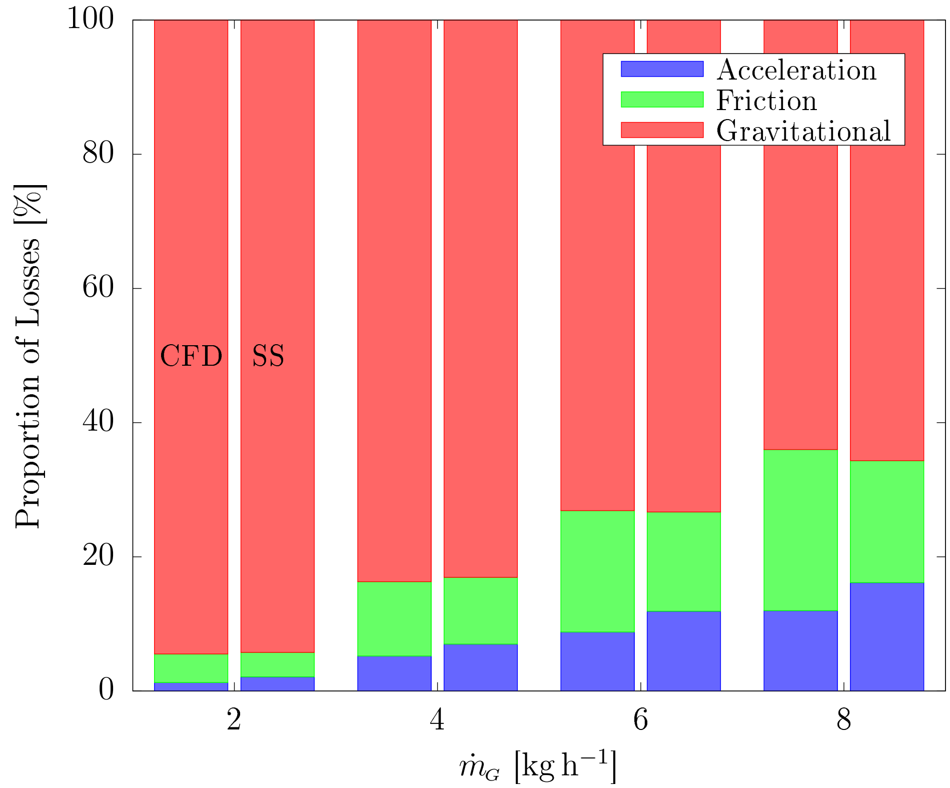

Figure C.9: Comparison of the relative magnitude of losses between the CFD model and steady-state model of Kassab *et al.* [25] for C3.

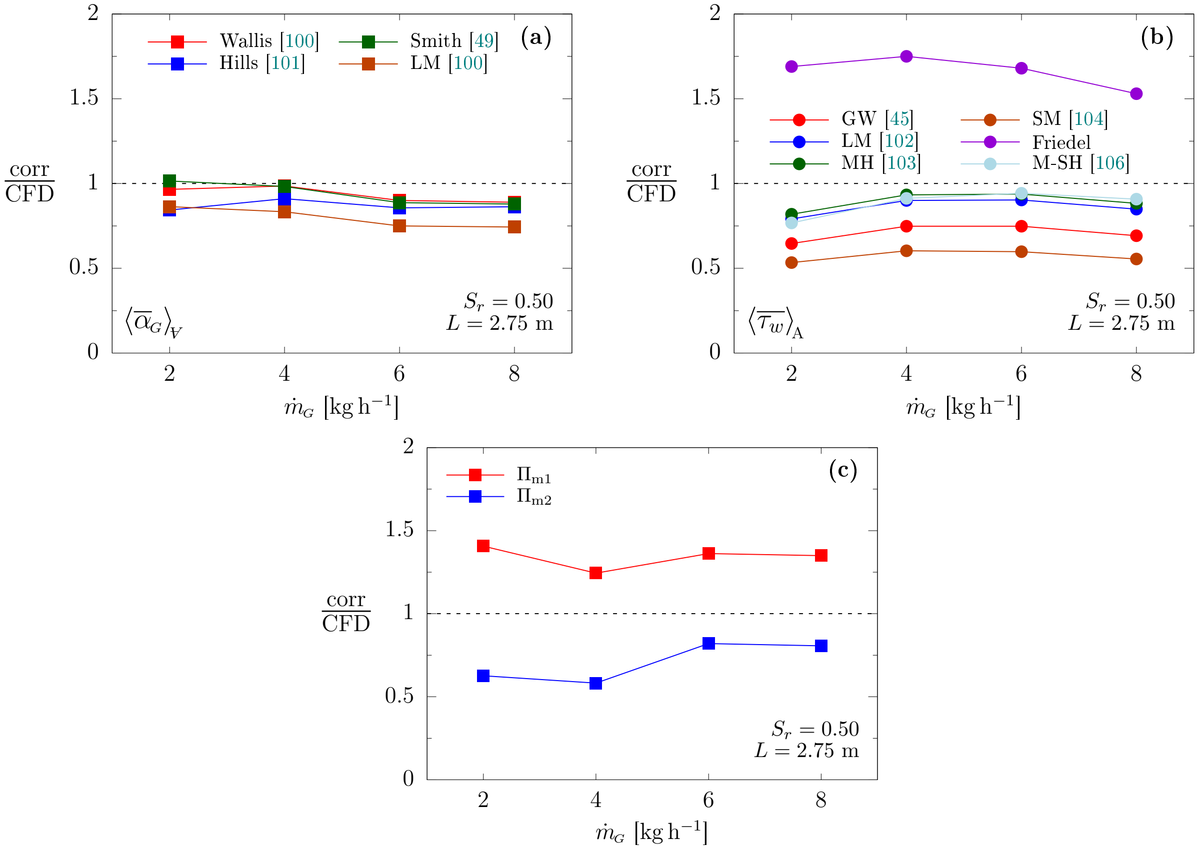

Figure C.10: Comparison of values predicted by correlation to measurements from CFD simulation.

Appendix D

Code Listing

This appendix contains code segments from the selected programs used in this work.

D.1 CFX

Due to the length of the file, CFX files for the model setup and solution monitor points will be provided upon request. User-written macro codes used for post-processing of the simulation results are included below.

D.1.1 Axial profile Export

```
#  Written in Perl
#
#---------------------------------------------------------------#
# Input parameters are entered through the GUI that appears when
# this file is loaded in the "Macro Calculator" in CFD Post.
#
# Results are output to a text file.
#---------------------------------------------------------------#
#
#---------------------------------------------------------------#
# Set up  a GUI to enter various input parameters
#---------------------------------------------------------------#
# Macro GUI begin
#
# macro name = Twophase Value distributions: Y
# macro subroutine = HYDY
# macro output file = HYD_y.out
#
# macro parameter = separator
#  type = Separator
#
# macro parameter = comment
#  type = Comment
#  default = void, Sup. Vel, along Y
#
```

```
# macro parameter = Domain Name
#  type = Location
#  location type = Domain
#
# macro parameter = OS 0(Win), 1(Lin)
#  type = Int
#  range = 0,1
#  default = 0
#
# macro parameter = Begin Location [m]
#  type = Float
#  quantity type = length
#  range = -3 [m], 3 [m]
#  default = 0.0 [m]
#
# macro parameter = End Location [m]
#  type = Float
#  quantity type = length
#  range = -10 [m], 10 [m]
#  default = 1.749 [m]
#
# macro parameter = Y ref length [m]
#  type = Float
#  quantity type = length
#  range = 0 [m], 10 [m]
#  default = 1.750 [m]
#
# macro parameter = Nslices
#  type = Int
#  range = 2, 5000
#  default = 7
#
# macro parameter = x mid location (xmid) [m]
#  type = Float
#  quantity type = length
#  range = -1 [m], 1 [m]
#  default = 0.00 [m]
#
# macro parameter = z mid location (zmid) [m]
#  type = Float
#  quantity type = length
#  range = -1 [m], 1 [m]
#  default = 0.00 [m]
#
# macro parameter = CSV Format Flag
#  type = Int
#  range = 0,1
#  default = 0
#
```

```
# Macro GUI end
#-----------------------------------------------------------------#
#
#*******************************************************
#  NOTE: Do NOT use the true Y bound as "End Location".
#        Otherwise, the macro will fail.
#        i.e.: if y is defined from [0-2]
#        set "End Location" as 1.99999 instead of 2
#*******************************************************
! no warnings 'redefine';
#-----------------------------------------------------------------#
# Set up subroutine to calculate and output values along y
#-----------------------------------------------------------------#
!sub HYDY  {
!  ($DomainName, $OSFlag,\
    $yBegin, $yEnd, $y_Lref, $Nslices, $x_mid, $z_mid,\
    $csvFlag) = @_;
#
## If necessary Hard-coded values specified here
#

#use this for debug printing if needed
#(uncomment these two lines and comment the open(OUT_H line later)
##! $outFile = "HYD_y_tmp.out";
##!  open(OUT_H,">$outFile");

! $datetime= scalar(localtime);  # get date and time
#-----------------------------------------------------------------#
# Create string to be used for the output file name.
#
# Get the full path and name of the results file
! $fullresfname = getValue("DATA READER", "Current Results File");

# Create a vector of substrings that come from splitting the full results
# file name into the strings separated by the path character.
# This character is "\" on Windows and "\" on Linux. Use the OS flag
# to tell the macro which one to use.
#
!  if( $OSFlag == 0 ) {
# Windows
!   @subStrings = split (/\\/, $fullresfname);
!  }
!  else {
# Linux
!  @subStrings = split ('/', $fullresfname);
!  }
# get the number of elements in the substrings vector
! $size = @subStrings;
```

```
# collect the last part of the full file name into a string
# the vector first element is zero, so if, for example,
# the size is 4 elements, the last element has index 3 (size - 1).
#
! $shortresfname = $subStrings[$size -1];
! $simTstep = getValue("/LIBRARY/CEL/EXPRESSIONS", "Current Time Step");
# Copy the res fname into another string,
# then replace the .res extension with a more meaningful string
# and extension for the data produced here.
#
! $H_outputfile = $shortresfname;
! $H_outputfile =~ s/\.res/\_axial_profiles-Trnavg\.dat/g;
#-----------------------------------------------------------------#

# Open a text file to store the hydrodynamic results
!  open(OUT_H,">$H_outputfile");

!  printf(OUT_H "%1s %s\n", "#"," ============ General Info ==========");
!    printf(OUT_H "%1s %s %s\n", "#", "date and time:", $datetime);
!    printf(OUT_H "%1s %s %s\n", "#", "fullresfname:", $fullresfname);
##!    printf(OUT_H "%1s %s %d\n", "#", "size:", $size);
##!    printf(OUT_H "%1s %s %s\n", "#", "shortresfname:", $shortresfname);
!    printf(OUT_H "%1s %s %s\n", "#",\
    "Hydrodynamic output file name:", $H_outputfile);
!  printf(OUT_H "%1s %s\n", "#"," ====================================");
#! $simT = evaluate("Time");
! $simT = getValue("/LIBRARY/CEL/EXPRESSIONS", "Time");
# Echo input parameters to HYD file
!  printf(OUT_H "%1s %s\n", "#"," ************ Input values **********");
!  printf(OUT_H "%1s %s %s \n",   "#", "Domain: ",          $DomainName);
!  printf(OUT_H "%1s %s %d \n",   "#", "OS Flag (0=Win,1=Lin):", $OSFlag);
!  printf(OUT_H "%1s %s %g %s\n", "#", "Y Begin: ",         $yBegin,"[m]");
!  printf(OUT_H "%1s %s %g %s\n", "#", "Y End: ",           $yEnd,"[m]");
!  printf(OUT_H "%1s %s %g %s\n", "#", "Y Ref Length: ",    $y_Lref,"[m]");
!  printf(OUT_H "%1s %s %d \n",   "#", "Number of Slices: ",$Nslices);
!  printf(OUT_H "%1s %s %g %s\n", "#", "X mid location:",   $x_mid,"[m]");
!  printf(OUT_H "%1s %s %g %s\n", "#", "Z mid location:",   $z_mid,"[m]");
!  printf(OUT_H "%1s %s %g %s\n", "#", "Simulation time:",  $simT,"[s]");
!  printf(OUT_H "%1s %s\n", "#"," ************************************");

########################################################################
# Define some local variables for the length of the domain
#!  $minY = 0.99999*minVal("Y",$DomainName);
#!  $maxY = 0.999999*maxVal("Y",$DomainName);

# Fix yEnd if it is too close to yBegin
#!  $minrange = 0.001*($maxY - $minY);
#!  if( abs( $yEnd - $yBegin ) < $minrange ) {
#!    $yEnd = $yBegin + $minrange;
```

```
#!    printf(OUT_H "%1s %s\n", "#"," *** Fixed the value of yEnd **");
#!    printf(OUT_H "%1s %s %s \n", "#", "yEnd [m]: ", $yEnd);
#!  }

# Calculate step size along y-axis
!  $Ystep = ($yEnd-$yBegin)/($Nslices - 1);

!  printf(OUT_H "%1s %s %g \n", "#", "Ystep [m]: ", $Ystep);

!  $varName = "Pressure";

# Create a slice plane at the beginning of the y range
   PLANE:calcSlice
     Option = Point and Normal
     Normal = 0,1,0
     Point = $x_mid,$yBegin,$z_mid
     Domain List = $DomainName
     Colour Mode = Variable
     Colour Variable = $varName
     Colour Variable Boundary Values = Conservative
     Range = Local
     Visibility = Off
   END
# Create line for wall shear
   POLYLINE:Polyline 1
 Boundary List = wall A,wall B,wall C,wall ent,wall inj
 Colour = 0, 1, 0
 Colour Map = Default Colour Map
 Colour Mode = Constant
 Colour Scale = Linear
 Option = Boundary Intersection
 Location = /PLANE:calcSlice
    END
# Print a header line for the results to the HYD output file
!  if ( $csvFlag == 0 ) {
!    printf(OUT_H "%1s %7s %14s %14s %14s %14s %14s %14s %13s\n",\
           '#', '"Local Y"', "P CFX,", "P static,", "Velocity", "Void", 'Wall shear', '"Global Y"');
!  }
!  else {
!    printf(OUT_H "%s%s%s%s%s%s\n",\
           "Local Y,", "P CFX,", "P static,", "Velocity", "Void", "Global Y");
!  }


#######################################################################
# Start a loop from the beginning to the end value along the y-axis
!  for ($Y = $yBegin; $Y <= $yEnd; $Y += $Ystep) {

# Update slice plane location
```

```
     PLANE:calcSlice
       Domain List = $DomainName
       Option = Point and Normal
       Normal = 0,1,0
       Point = $x_mid,$Y,$z_mid
       Colour Mode = Variable
       Colour Variable = $varName
       Range = Local
       Visibility = On
       Colour Variable Boundary Values = Conservative
     END
 POLYLINE:Polyline 1
   Boundary List = wall A,wall B,wall C,wall ent,wall inj
   Colour = 0, 1, 0
   Colour Map = Default Colour Map
   Colour Mode = Constant
   Colour Scale = Linear
   Option = Boundary Intersection
   Location = /PLANE:calcSlice
    END

#---HYD results ----------------------------------#
# Compute the local average pressure and axial velocity number
#
#--Use conservative values for Uavg
   SCALAR VARIABLE:Velocity u
     Boundary Values = Conservative
   END
#
#! $Pavg     = areaAve("Pressure","calcSlice");
! $Pavg  = 1;
! $P_static     = areaAve("Absolute Pressure.Trnavg","calcSlice") - 101300.0;
! $Vavg_mix   = areaAve("water.Velocity v.Trnavg","calcSlice");
! $void     = 1- areaAve("water.Volume Fraction.Trnavg","calcSlice");
! $wall_shear   = lengthAve("water.Wall Shear Y.Trnavg","Polyline 1")
                +lengthAve("air.Wall Shear Y.Trnavg","Polyline 1");
#
! $ylocal = ($Y - $yBegin)/$y_Lref;

# Print the HYD results for the present location to the output file
! if ( $csvFlag == 0 ) {
!   printf(OUT_H "%10.7f %14.6g %14.6g %14.6g %14.6g %14.6g %13.7f\n",\
    $ylocal, $Pavg, $P_static, $Vavg_mix, $void, $wall_shear, $Y);
! }
! else {
!   printf(OUT_H "%g,%g,%g,%g,%g,%g,%g\n",\
    $ylocal, $Pavg, $P_static, $Vavg_mix, $void, $Y);
! }
```

```
# End of the loop
! }
#######################################################################


# Close the output files
! close(OUT_H);

# Set the variable back to Hybrid values
   SCALAR VARIABLE:$varName
     Boundary Values = Hybrid
   END

# End of the subroutine
! }
#================================================================#
```

D.1.2 Development Length Calculation

```
#  Written in Perl
#
#----------------------------------------------------------------#
# Input parameters are entered through the GUI that appears when
# this file is loaded in the "Macro Calculator" in CFD Post.
#
# Results are output to a text file.
#----------------------------------------------------------------#
#
#----------------------------------------------------------------#
# Set up  a GUI to enter various input parameters
#----------------------------------------------------------------#
# Macro GUI begin
#
# macro name = phase separation point
# macro subroutine = HYDY
# macro output file = HYD_y.out
#
# macro parameter = separator
#  type = Separator
#
# macro parameter = comment
#  type = Comment
#  default = find air film dettachment point
#
#
# macro parameter = OS 0(Win), 1(Lin)
#  type = Int
```

```
#  range = 0,1
#  default = 0
#
# macro parameter = Begin Location [m]
#  type = Float
#  quantity type = length
#  range = -3 [m], 3 [m]
#  default = 0.2 [m]
#
# macro parameter = End Location [m]
#  type = Float
#  quantity type = length
#  range = -10 [m], 10 [m]
#  default = 1.5 [m]
#
#
# macro parameter = Nslices
#  type = Int
#  range = 2, 5000
#  default = 400
#
# macro parameter = x mid location (xmid) [m]
#  type = Float
#  quantity type = length
#  range = -1 [m], 1 [m]
#  default = 0.00 [m]
#
# macro parameter = z mid location (zmid) [m]
#  type = Float
#  quantity type = length
#  range = -1 [m], 1 [m]
#  default = 0.00 [m]
#
# macro parameter = CSV Format Flag
#  type = Int
#  range = 0,1
#  default = 0
#
# Macro GUI end
#-------------------------------------------------------------#
#
#######################################################
#  NOTE: Do NOT use the true Y bound as "End Location".
#        Otherwise, the macro will fail.
#        i.e.: if y is defined from [0-2]
#        set "End Location" as 1.99999 instead of 2
#######################################################
! no warnings 'redefine';
#-------------------------------------------------------------#
```

```
# Set up subroutine to calculate and output values along y
#----------------------------------------------------------------#
!sub HYDY  {
!  ($OSFlag,\
    $yBegin, $yEnd, $Nslices, $x_mid, $z_mid,\
    $csvFlag) = @_;
#
## If necessary Hard-coded values specified here
#

#use this for debug printing if needed
#(uncomment these two lines and comment the open(OUT_H line later)
##! $outFile = "HYD_y_tmp.out";
##!  open(OUT_H,">$outFile");

! $datetime= scalar(localtime);  # get date and time
#----------------------------------------------------------------#
# Create string to be used for the output file name.
#
# Get the full path and name of the results file
! $fullresfname = getValue("DATA READER", "Current Results File");

# Create a vector of substrings that come from splitting the full results
# file name into the strings separated by the path character.
# This character is "\" on Windows and "\" on Linux. Use the OS flag
# to tell the macro which one to use.
#
!  if( $OSFlag == 0 ) {
# Windows
!   @subStrings = split (/\\/, $fullresfname);
!  }
!  else {
# Linux
!  @subStrings = split (’/’, $fullresfname);
!  }
# get the number of elements in the substrings vector
! $size = @subStrings;

# collect the last part of the full file name into a string
# the vector first element is zero, so if, for example,
# the size is 4 elements, the last element has index 3 (size - 1).
#
! $shortresfname = $subStrings[$size -1];

# Copy the res fname into another string,
# then replace the .res extension with a more meaningful string
# and extension for the data produced here.
#
! $H_outputfile = $shortresfname;
```

```
! $H_outputfile =~ s/\.res/\_sep-point\.dat/g;
#-----------------------------------------------------------------#

# Open a text file to store the hydrodynamic results
!  open(OUT_H,">$H_outputfile");

!  printf(OUT_H "%1s %s\n", "#"," ============ General Info ==========");
!    printf(OUT_H "%1s %s %s\n", "#", "date and time:", $datetime);
!    printf(OUT_H "%1s %s %s\n", "#", "fullresfname:", $fullresfname);
##!    printf(OUT_H "%1s %s %d\n", "#", "size:", $size);
##!    printf(OUT_H "%1s %s %s\n", "#", "shortresfname:", $shortresfname);
!    printf(OUT_H "%1s %s %s\n", "#",\
    "Hydrodynamic output file name:", $H_outputfile);
!  printf(OUT_H "%1s %s\n", "#"," ====================================");

# Echo input parameters to HYD file
!  printf(OUT_H "%1s %s\n", "#"," ************ Input values **********");
!  printf(OUT_H "%1s %s %d \n",   "#", "OS Flag (0=Win,1=Lin):", $OSFlag);
!  printf(OUT_H "%1s %s %g %s\n", "#", "Y Begin: ",         $yBegin,"[m]");
!  printf(OUT_H "%1s %s %g %s\n", "#", "Y End: ",           $yEnd,"[m]");
!  printf(OUT_H "%1s %s %d \n",   "#", "Number of Slices: ",$Nslices);
!  printf(OUT_H "%1s %s %g %s\n", "#", "X mid location:",   $x_mid,"[m]");
!  printf(OUT_H "%1s %s %g %s\n", "#", "Z mid location:",   $z_mid,"[m]");
!  printf(OUT_H "%1s %s\n", "#"," **********************************");

#########################################################################
# Define some local variables for the length of the domain
# !  $minY = 0.99999*minVal("Y",$DomainName);
# !  $maxY = 0.999999*maxVal("Y",$DomainName);

# # Fix yEnd if it is too close to yBegin
# !  $minrange = 0.001*($maxY - $minY);
# !  if( abs( $yEnd - $yBegin ) < $minrange ) {
# !    $yEnd = $yBegin + $minrange;
# !    printf(OUT_H "%1s %s\n", "#"," *** Fixed the value of yEnd **");
# !    printf(OUT_H "%1s %s %s \n", "#", "yEnd [m]: ", $yEnd);
# !  }

# Calculate step size along y-axis
!  $Ystep = ($yEnd-$yBegin)/($Nslices - 1);

!  printf(OUT_H "%1s %s %g \n", "#", "Ystep [m]: ", $Ystep);

POINT: centerline
Option = XYZ
Point = 0 [m], 0 [m], 0 [m]
Visibility = off
END
```

```
########################################################################
##       transient averaging loop around axial sweep loop
########################################################################
! $read_TimeSteps = (getValue("DATA READER", "Timestep List"));
! @Timestep_list = split(/, /, $read_TimeSteps );
#! @Timestep_list = (26000, 28000); # manual test auto generate later
# initialize
! $N_Tstep = @Timestep_list;
#! @Ylist   = (0) x $N_Tstep;
! @Ylist = ();
! printf(OUT_H "%s %d \n", "# Number of timesteps" , $N_Tstep);
! foreach $Timestep (@Timestep_list){
>load timestep=$Timestep
########################################################################
# Start a loop from the beginning to the end value along the y-axis
! $Y = $yBegin;
! $done = 0;
! while ( ($Y <= $yEnd)&& ($done ne 1)) {
# update point location
POINT: centerline
Option = XYZ
Point = 0 [m], $Y, 0 [m]
Visibility = off
END
! $void = probe("air.Volume Fraction","centerline");
! if ($void >0.9) {
! push @Ylist, $Y;
#! printf(OUT_H "%d %8.6f \n" , $Timestep, $Y);
! $done = 1;
! }
! $Y += $Ystep;
# End of the axial sweep loop
! }
# ! printf(OUT_H "%s", 'test')
#End of the time averaging loop
! }
##################################################################
! $sum = 0;
! foreach (@Ylist) {
! $sum += $_;
# !  printf(OUT_H "%f \n", $sum);
! }
! $avg = $sum/$N_Tstep;
!  printf(OUT_H "%1s %s\n", "#"," ***********************************");
! printf(OUT_H "%s %8.6f \n", "# average seperation point:" , $avg);
!  printf(OUT_H "%1s %s\n", "#"," ***********************************");
# print header
! printf(OUT_H "%s \n", '#Time step   Yloc');
! for ($k = 0; $k <=$#Ylist; $k +=1){
```

```
! printf(OUT_H "%8d %8.6f \n" , $Timestep_list[$k], $Ylist[$k]);
! }
#
# Close the output files
! close(OUT_H);

# End of the subroutine
! }
#================================================================#
```

D.2 Steady-State Model

```
program main
implicit none
real flowrate  ! initialize function
!initialize variables for curve generation loop
real:: QG_max,QG_min,ratio
real:: in1,in2,in3
integer:: i  ! loop counter
integer, parameter:: Npoints=100     ! number of points in the flowrate curve
real, dimension(Npoints) :: QG,QL  !kg/hr
!initialize variables for file name and writing
character(30)::filetag
character(100)::filename

!################################!
! read in model parameters  !
!################################!

write(*,*) "name of experiment data set"
read(*,*) filetag
write(*,*) "min air flow rate [kg/hr]"
read(*,*) QG_min
write(*,*) "max air flow rate [kg/hr]"
read(*,*) QG_max
write(*,*) "diameter [m]"
read(*,*) in1
write(*,*) "submergence ratio"
read(*,*) in2
write(*,*) "length [m]"
read(*,*) in3

!####################################################!
! calculate step size and generate list of QG values !
!####################################################!

ratio=(Npoints)/(QG_max-QG_min)  ! calculate step size
```

```
do i=1,Npoints ! generate list
QG(i)=QG_min+i/ratio
enddo

!################################!
! calculate QL for a given QG.  !
! store as a list  !
!################################!

do i=1,Npoints
! perform flow rate calcutation
QL(i)=(flowrate(QG(i)/1.3/3600.,in1,in2,in3))*1000*3600
enddo

!########################################!
! file operations write data to file    !
!########################################!

filename = "ahmed-model-" // trim(filetag) // ".dat"  ! create file name
write(*,*) "creating output file:", filename ! print file name to screean
open (unit=10,file=trim(filename)) ! open file
write(10,'(1X,a,6X,f5.3)') "# Diameter [m]", in1 ! write header with model inputs
write(10,'(1X,a,1X,f5.3)')  "# Submergence ratio", in2
write(10,'(1X,a,8X,f5.3)')  "# Length [m]", in3
write(10,'(1X,a,1X,a,1X,a)') '#','air [kg /hr]','water [kg / hr]'! write data column headers
do i=1,Npoints
write(10,'(1pe14.7,1X,e14.7)') QG(i), QL(i) ! write data lists
enddo
close(10) ! close file
!
end program main

!###############################################################!
! function for calculating QL for a given QG. works in m3/s.    !
! uses iterative newton raphson solver
!###############################################################!

real function flowrate(Q_g,D,submergence_ratio,L)   !takes Q_g in m3/s returns Q_L in m3/s
implicit none
real, intent(in) :: Q_g,D,submergence_ratio,L !function inputs
real :: g=9.81, rho =1000., mu = 8.9E-4 !hard coded water properties
real :: f, K, V1,V_tot, s, A, Re,  !physical variables
real :: FF, QS, df1, df2, df3, ds, dFF, dK  !intermediate terms to simplify writing func
real :: func , derivative, Q_l_old,Q_l_new, error, tolerance !variables for root search
integer :: counter !loop counter
error  = 1  !initialize loop
counter = 0  !initialize loop
tolerance = 1E-4 !initialize loop
```

```
!##################################################!
! perform constant calculations out side of loop   !
!##################################################!

A = 3.14/4.*D**2. !calculate cross-sectional area
Q_l_old =0.01*Q_g !initial guess
K = 4. !initial guess
s = 1.94 !initial guess

!##########################!
! begin root search loop   !
!##########################!

do while( (error >tolerance) .and. (counter<500) )
! calculate terms for func
V1=abs(Q_l_old/A)
V_tot= (Q_l_old+Q_g)/A
Re = rho*V1*D/mu
FF = 150.39/(Re**0.98865)-152.66/Re
s= 1.2+0.2*Q_g/Q_l_old + 0.35*sqrt(g*D)/V1
f=0.25*(log10(FF))**(-2)
K=f*L/D
QS = 1.+ Q_g/(s*Q_l_old)
! calculate function
func = ( 1.0 / (1.0 + Q_g/(s*Q_l_old))
 - submergence_ratio
 + (K+1.+(K+2.0d+0)*Q_g/Q_l_old) * Q_l_old**2 /2./ g/L/A**2)
! calculate terms for derivative
ds = -0.2*Q_g/Q_l_old**2 - 0.35*A*sqrt(g*D)/Q_l_old**2
dFF = rho*D/(A*mu) * (150.39*(-0.98865)/Re**1.98865 + 152.66/Re**2)
dK =-2.*L/D*(log10(FF))**(-3)/(FF*log(10.))*dFF
df1 = Q_g/QS**2 * (ds/(Q_l_old*s**2) + 1./(s*Q_l_old**2))
df2 = 2.*Q_l_old*K + Q_l_old**2*dK + 2.*Q_l_old
df3 = Q_g*(K + Q_L_old*dK+2)
! calculate derivative
derivative = df1 + (df2 + df3)/(2.*g*L*A**2)
! perform root search
Q_l_new = Q_l_old - func/derivative !solve for new iteration value
error = abs(func) !calculate error
Q_l_old = Q_l_new !update old iteration value
counter=counter+1 !update loop count
enddo
flowrate = Q_l_new !write value to output from function [m3/s]
!write an error message to the screen if the root search did not converge
if (error >tolerance) then
write (*,*) "not converged for m_g",Q_g
end if
end function flowrate
```

D.3 Results Processing in Matlab

Several short codes were written in Matlab to perform results processing operations on .csv datafiles exported from the simulation results.

D.3.1 Liquid Discharge Rate Calculation

```
%===============================================================%
%    code assumes a constant timestep
%===============================================================%
clear all
path = '..\kassab\monitor-exports\';
%
startTrim = 0.0%[s]
%
File  = 'L275-SR74-8kg-flow.csv';
Tstep=1e-4;
%
%read file
dataFile = readmatrix(strcat(path,File),'NumHeaderLines',(5+round(startTrim/1e-4)));
%create time series array
time = Tstep*dataFile(:,1);
waterIn =  dataFile(:,4);
waterOut = dataFile(:,5);
clear dataFile
%
%remove mean
y1 = waterIn-mean(waterIn);
y2 = waterOut-mean(waterOut);
std1 = std(y1)*3600;      %mean removed
std2 = std(y2)*3600;
$
%calculate autocorrelation
maxLag = 10000; % maximum lag
[c1,lags] = xcorr(y1,maxLag); %water out
c1 = c1([ (maxLag+1) : (maxLag*2+1) ]);        %remove negative lags
lags = lags([ (maxLag+1) : (maxLag*2+1) ]);
lagTime = lags*Tstep;    %convert lags to time shift
c1 = c1/c1(1);  %normalize
%stem(lagTime1(1:100:end) ,c1(1:100:end) )  %plot autocorrelation vs time shift
decorr_TimeIn = lagTime(find(c1<0.0001,1)); % finds indix of when autocorrelation approaches 0
%
[c2,lags] = xcorr(y2,maxLag); %water out
c2 = c2([ (maxLag+1) : (maxLag*2+1) ]);        %remove negative lags
c2 = c2/c2(1);  %normalize
%stem(lagTime(1:100:end) ,c2(1:100:end) )  %plot autocorrelation vs time shift
```

```
decorr_TimeOut = lagTime(find(c2<0.0001,1)); % finds indix of when autocorrelation approaches 0
%
%error calc
errorin  = sqrt( decorr_TimeIn *2.0/(time(end)-time(1))*(std(waterIn ))^2 / (mean(waterIn ))^2 );
errorout = sqrt( decorr_TimeOut*2.0/(time(end)-time(1))*(std(waterOut))^2 / (mean(waterOut))^2 );
%
% accumulating average
avgWaterIn(1)  = waterIn(1);
avgWaterOut(1) = waterOut(1);
avgMomOut(1) = momOut(1);
for I =2:length(time)
    avgWaterIn(I)  = (I-1)*avgWaterIn(I-1) /I +waterIn(I)/I;
    avgWaterOut(I) = (I-1)*avgWaterOut(I-1)/I + waterOut(I)/I;
    avgMomOut(I)   = (I-1)*avgMomOut(I-1)/I   + momOut(I)/I;
end
store =avgWaterOut;
avgflow = (avgWaterIn(end) + avgWaterOut(end))/2;
%normalize by end value
avgWaterIn = avgWaterIn/avgWaterOut(end);
avgWaterOut = avgWaterOut/avgWaterOut(end);
%
% check for period average is converged
DIFF = abs(avgWaterIn - avgWaterOut);
I=length(time);
%sweep backwards in time staating from the end
while ((DIFF(I)<0.05) && (avgWaterOut(I)>0.975) && (avgWaterOut(I)<1.025))
    I = I - 1;
    cnvgdTime = time(end) - time(I);
    timeToCnvg = time(I) - time(1);
end
```

D.3.2 Force Proportion Calculation

```
clear all
File  = 'L275-SR74-8kg-force.csv';
path = '..\kassab\monitor-exports\';
outName = strcat(File(1:end-4),'-force.dat');
startTrim = 0.0;%[s]
L = 2.75;
SR = 0.74;
rhoL = 997;
A = pi*0.0254^2/4;
Pinlet = A*rhoL*9.81*L*SR;
%read file
dataFile = readmatrix(strcat(path,File),'NumHeaderLines',(5+round(startTrim/1e-4)));
time = 1e-4*dataFile(:,1);
N = length(time);
```

```
%
Pstat  = [dataFile(:,2:6)  zeros(N,1)] ;   %N add zero pressure at outlet
Pcfx   = [dataFile(:,7:11) zeros(N,1)] ;  %N add zero pressure at outlet
weight = dataFile(:,12:16); %N
wall   = dataFile(:,17:21); %N
momcfx    = dataFile(:,22:27); %N
% remove pressure from CFX momentum
mom = momcfx - Pcfx; % in,in,in,in,in,out
mom(:,6) = mom(:,6)*-1; %flip sign for momentum out
deltaMom = mean(mom(:,6))-mean(mom(:,1))
totWeight = sum(mean(weight,1));
totWall   = sum(mean(wall,1));
WSS = (totWall-mean(wall(:,1))-mean(wall(:,2)))/((L-0.262659)*pi*0.0254);
proportion = [deltaMom/Pinlet totWeight/Pinlet totWall/Pinlet]*100
forcebal = zeros(N,5);
for i=1:5 % length of subdomains
    forcebal(:,i) = -(mom(:,i+1) - mom(:,i))     ...
                    -(Pstat(:,i+1) - Pstat(:,i)) ...
                    - weight(:,i) - wall(:,i);
end
forcebalRiser = forcebal(:,3) + forcebal(:,4) + forcebal(:,5);
normImbal = mean(forcebal)./mean(weight)*100;
totImbal = sum(mean(forcebal))/Pinlet*100
```